


2011

## Characterization of the Nonlinear Refractive Index of Carbon Disulfide Over an Extended Spectral and Temporal Range

Marcus Seidel  
*University of Central Florida*

 Part of the [Electromagnetics and Photonics Commons](#), and the [Optics Commons](#)  
Find similar works at: <https://stars.library.ucf.edu/etd>  
University of Central Florida Libraries <http://library.ucf.edu>

This Masters Thesis (Open Access) is brought to you for free and open access by STARS. It has been accepted for inclusion in Electronic Theses and Dissertations by an authorized administrator of STARS. For more information, please contact [STARS@ucf.edu](mailto:STARS@ucf.edu).

---

### STARS Citation

Seidel, Marcus, "Characterization of the Nonlinear Refractive Index of Carbon Disulfide Over an Extended Spectral and Temporal Range" (2011). *Electronic Theses and Dissertations*. 6667.  
<https://stars.library.ucf.edu/etd/6667>

CHARACTERIZATION OF THE NONLINEAR REFRACTIVE INDEX OF CARBON  
DISULFIDE OVER AN EXTENDED SPECTRAL AND TEMPORAL RANGE

by

MARCUS SEIDEL

A thesis submitted in partial fulfillment of the requirements  
for the degree of Master of Science  
in CREOL - the College of Optics and Photonics  
at the University of Central Florida  
Orlando, Florida

Summer Term  
2011

© 2011 Marcus Seidel

## ABSTRACT

The intensity dependent refractive index change of a medium is frequently described in terms of the product  $n_2 \cdot I$  where  $n_2$  is the nonlinear refractive index and  $I$  the light intensity. The nonlinear refractive index is often treated as constant which is a reasonable assumption if the light interacts only with bound electrons. In the case of carbon disulfide ( $\text{CS}_2$ ) however, nuclear motions contribute to  $n_2$ . These motions occur on the sub picosecond time scale and thus become especially relevant for ultrashort laser pulses. The neat liquid  $\text{CS}_2$  is studied because it exhibits a large nonlinear refractive index in comparison to other liquids. Therefore, it is employed in optical switching, optical limiting, and beam filamentation applications.

This thesis presents effective  $n_2$  values for Gaussian shaped linearly polarized pulses with central wavelength at  $\lambda = 700\text{nm}$ . A theoretical model describing the time evolution of the material response is applied to distinguish between the instantaneous electronic, the ultrafast nuclear and the slow nuclear origins of the nonlinear refractive index. Moreover, the tensor nature of the material response function is studied by means of circularly polarized light. The relative magnitudes of bound electronic and nuclear contributions to  $n_2$  are experimentally determined. Eventually, the dispersion of the instantaneous electronic response is measured in the spectral range between  $390\text{nm}$  and  $1064\text{nm}$ .



## ACKNOWLEDGMENTS

First, I would like to thank god for gifting me ability and opportunity to earn a master's degree in science at the College of Optics and Photonics in Orlando. Many buttons had to be pushed that were not accessible to me and I am glad that finally everything turned out very well.

That thesis could be written in a fairly short amount of time which was only possible by means of the strong support of the nonlinear optics group of CREOL. I especially would like to thank my advisors Dr. Eric Van Stryland, Dr. David Hagan and Dr. Peter Delfyett as well as the postdocs Dr. Scott Webster and Dr. Dmitry Fishman and the PhD candidate Honghua Hu who spent many, many hours in the lab to align the measurement setup excellently. Moreover, graduating does unfortunately not only require academic guidance but also financial support. I am absolutely pleased that I was allowed to study at UCF as a Fulbright scholar. I would like to thank the staff and supporters of the German-American program for giving me the opportunity to participate in the MS program and for guiding me in my new cultural environment. I would also like to thank the College of Graduate Studies at UCF to waive my tuitions in the final summer term and for granting me admission to the graduate program without having an undergraduate degree. With respect to both issues I also enjoyed the support of the CREOL as well as the Fulbright and the IIE staff, respectively.

Eventually, high academic performance is merely feasible in a pleasant social environment. That is why I would like to thank my friends who have shared with me that marvellous year in the United States. I would like to thank the "German-French connection" at CREOL and

at St. John's Church for protecting me from crashing very hard into the cultural barrier between Europe and the US as well as for sharing my interests of seeing the country and enjoying spare time. Also, I would like to thank my American friends who enabled me to dive into the American culture and to gain unforgettable impressions of the living beyond the great sea. I am thankful that family O'Toole offered and "subsidized" me a car which made me mobile and allowed me not only to get to CREOL more conveniently but also to see many beautiful places in my leisure time. Finally, I have been absolutely happy to stay in contact with my friends and family in Germany. I would like to thank them for keeping me in mind all the time despite the spatial separation. In particular, I would like to thank my next of kin: Birgit, Reinhard and Daniel Seidel.

# TABLE OF CONTENTS

LIST OF FIGURES	ix
LIST OF TABLES	xi
LIST OF MEDIA	xii
LIST OF NOMENCLATURE AND ABBREVIATIONS	xiii
<b>1 INTRODUCTION</b>	<b>1</b>
1.1 Motivation of the Work . . . . .	1
1.2 Properties and Linear Characterization of Carbon Disulfide . . . . .	4
1.3 The Nonlinear Refractive Index and Two-photon Absorption . . . . .	5
1.3.1 The Nonlinear Refractive Index . . . . .	8
1.3.2 Two-photon Absorption . . . . .	9
<b>2 EXPERIMENTAL TECHNIQUE</b>	<b>11</b>
2.1 The Z-scan . . . . .	11
2.1.1 Fundamental Idea . . . . .	11
2.1.2 Z-scan Theory for Thin Samples . . . . .	13
2.2 Experimental Setup . . . . .	17
2.2.1 Ultrafast Laser . . . . .	17
2.2.2 Optical Parametric Amplifier . . . . .	18
2.2.3 Prism Compressor . . . . .	19

2.2.4	Complete Setup . . . . .	20
2.2.5	Alignment Procedure . . . . .	23
2.3	Application of Gaussian Quadrature in the Data Analysis Algorithm . . . . .	23
3	PULSE WIDTH DEPENDENCE OF THE NONLINEAR REFRACTION IN CS <sub>2</sub>	<b>26</b>
3.1	The Measurement Procedure . . . . .	26
3.2	Effective $n_2$ for Gaussian Laser Pulses at $\lambda = 700nm$ . . . . .	31
3.3	Effective $n_2$ for Gaussian Laser Pulses at $\lambda = 1064nm$ . . . . .	32
3.4	Error Analysis . . . . .	34
3.5	Effective $n_2$ Measurements: Conclusions . . . . .	38
4	PARAMETRIZATION OF THE TIME DEPENDENCE OF $n_2$ IN CS <sub>2</sub>	<b>39</b>
4.1	Nuclear Motions in the Neat Liquid Carbon Disulfide . . . . .	39
4.1.1	Molecular Origins of $n_2$ . . . . .	39
4.1.2	Time Dependence of the Nuclear Response . . . . .	42
4.2	Macroscopic Description of the Noninstantaneous Material Response . . . . .	45
4.3	Implementation of the Parametrized Nonlinear Refractive Index in the Z-scan Analysis . . . . .	48
4.4	Fitted Parameters . . . . .	52
4.5	Parametrization Model: Conclusions . . . . .	58
5	POLARIZATION DEPENDENCE OF THE NONLINEAR REFRACTIVE INDEX	<b>60</b>
5.1	Tensor Nature of the Material Response Function . . . . .	60
5.1.1	Bound Electronic Contribution . . . . .	62
5.1.2	Slow Nuclear Contribution . . . . .	65
5.2	Polarization Measurements and Results . . . . .	66
5.3	Calculation of the Tensor Elements . . . . .	67
5.3.1	Electronic Susceptibility Tensor Elements . . . . .	67
5.3.2	Nuclear Polarizability Tensor . . . . .	70

5.3.3	Nuclear Susceptibilities . . . . .	72
5.4	Polarization Dependence of $n_2$ : Conclusions . . . . .	73
6	DISPERSION OF THE INSTANTANEOUS ELECTRONIC RESPONSE	<b>75</b>
6.1	The Role of Dispersion in the Electronic Response . . . . .	75
6.2	Dispersion Measurements . . . . .	76
7	CONCLUSIONS AND PROSPECTS	<b>80</b>
	APPENDIX A: CAUSALITY	<b>82</b>
	APPENDIX B: SLOWLY VARYING WAVE APPROXIMATION	<b>84</b>
	APPENDIX C: POWER TRANSMITTED THROUGH A THIN SAMPLE WITH TWO-PHOTON ABSORPTION	<b>87</b>
	APPENDIX D: ANALYTIC EXPRESSIONS OF THE NUCLEAR RESPONSE FUNCTIONS	<b>89</b>
	LIST OF REFERENCES	<b>93</b>

## LIST OF FIGURES

1.1	Linear transmittance and absorption spectrum, resp. of CS <sub>2</sub> . . . . .	5
2.1	Induced single beam interferometer. . . . .	13
2.2	Setup of a prism compressor. . . . .	20
2.3	Complete Z-scan Setup. . . . .	21
2.4	Convergence of the Gaussian quadrature algorithm up to a precision of 10 <sup>-12</sup> . . . . .	25
3.1	The linearity of the photo detectors. . . . .	27
3.2	Effects of sample inhomogeneities. . . . .	27
3.3	Determination of the beam waist by means of the open and the closed aperture Z-scan analysis. . . . .	30
3.4	Illustration of the $n_2$ least square fit routine for a prenormalized curve. . . . .	31
3.5	Example for the closed aperture data analysis for light of the wavelength $\lambda = 700nm$ . . . . .	32
3.6	Example for the closed aperture data analysis for light of the wavelength $\lambda = 1064nm$ . . . . .	34
3.7	Change of $n_2$ upon the variation of a single parameter. . . . .	36
3.8	Effective nonlinear refractive indexes at $\lambda = 700nm$ and $\lambda = 1064nm$ . . . . .	38
4.1	Rotational motions contribution to the nonlinear refraction. . . . .	44
4.2	Illustration of the fitting algorithm. . . . .	50
4.3	Long pulse boundary. . . . .	51

4.4	Reproduction of the previously determined $n_{2,eff}$ through the three and four contribution parameter model. . . . .	53
4.5	Material response plots that are derived from the rise as well as decay times and the magnitudes of the different contributions. . . . .	54
4.6	Proportionality of the peak-valley difference and the effective nonlinear refractive index . . . . .	55
5.1	Effective values and reference curves of the polarization measurements. . . .	68
6.1	Measured effective $n_2$ and $\beta$ spectrum for ultrashort pulses . . . . .	77
6.2	Experimentally determined dispersion curve of the electronic contribution to the nonlinear refractive index of CS <sub>2</sub> . . . . .	79

## LIST OF TABLES

1.1	Several examples for the nonlinear refractive index of neat liquids. . . . .	2
1.2	A selection of different $n_2$ measurements of CS <sub>2</sub> . . . . .	3
3.1	Effective nonlinear refractive indexes for Gaussian shaped laser pulses with central wavelength $\lambda = 700nm$ . . . . .	33
3.2	Effective nonlinear refractive indexes for Gaussian shaped laser pulses with central wavelength $\lambda = 1064nm$ . . . . .	35
4.1	Fitted parameters for the three and four contribution model. . . . .	52
4.2	Allowed variations of the parameters in the three contribution model. . . . .	56
4.3	Allowed variations of the parameters in the four contribution model. . . . .	57
5.1	Derived $n_2$ ratios between linearly and circularly polarized light. . . . .	67



## LIST OF MEDIA

2.1	The concept of Z-scan. . . . .	12
-----	--------------------------------	----

## LIST OF NOMENCLATURE AND ABBREVIATIONS

$\beta$	two-photon absorption coefficient - note that this $\beta$ has no subscript
$\beta_i$	rise time of a nuclear motion
$\chi^{(1)}$	complex linear susceptibility
$\Delta\omega$	inhomogeneous broadening factor of librational response
$\epsilon_0$	vacuum permittivity
$\kappa$	elastic force constant
$\lambda$	vacuum wavelength
$\mathcal{I}$	moment of inertia
$\mathcal{S}$	entropy
$\mathcal{T}(z')$	measured transmittance of a Z-scan
$\omega_0$	carrier frequency
$\Phi$	optical power, inverse of focal length
$\tau_i$	decay time of a nuclear motion
$\tilde{\alpha}$	polarizability tensor
$\tilde{\chi}^{(3)}$	complex third order susceptibility tensor
$\tilde{\mathcal{R}}(\vec{r}, t)$	complex material response tensor
$\vec{E}(\vec{r}, t)/\vec{\mathcal{E}}(\vec{r}, t)$	real/complex electric field vector

$\vec{M}$	torque
$\vec{p}$	electric dipole
$\vec{P}(\vec{r}, t)/\vec{\mathcal{P}}(\vec{r}, t)$	real/complex material polarization vector
$\vec{r}$	position vector
$\xi$	internal friction coefficient in CS <sub>2</sub>
$A(\vec{r}, t)/\mathcal{A}(\vec{r}, t)$	real/complex time and position dependent function describing a laser pulse and beam profile
$A_{\text{fit}}$	area between measured closed aperture Z-scan transmittance and theoretical transmittance
$c$	vacuum speed of light
$I(\vec{r}, t)$	light irradiance
$I_0$	laser pulse peak irradiance at $z = 0$
$I_p(z)$	laser pulse peak irradiance
$k_B$	Boltzmann constant
$L$	sample length
$L_{eff}$	Linear absorption corrected effective sample length
$n_0$	linear refractive index
$n_2$	(lowest order) nonlinear refractive index
$n_{2,eff}$	effective, i.e. pulse dependent, nonlinear refractive index
$n_i$	magnitude of the nonlinear refractive index induced by a certain contribution to the total response function
$r$	radial distance to the irradiance peak of a Gaussian beam

$r_a$	aperture radius in the Z-scan setup
$r_i(t)$	response function of a certain nuclear motion
$S$	linear aperture transmittance in the Z-scan setup
$T$	temperature
$t$	time
$T(z')$	theoretical transmittance of a Z-scan
$T_{PV}$	peak-valley difference in the closed aperture Z-scan transmission signal
$w_0$	beam waist of a Gaussian beam
$z$	distance to the beam waist location along the propagation axis in the description of a Gaussian pulse
$z_0$	Rayleigh length or Rayleigh range
BBO	$\beta$ -barium borate or $\beta - BaB_2O_4$
c.c.	complex conjugate
CdSe	cadmium selenide
cf	compare
CS <sub>2</sub>	carbon disulfide
e.g.	exempli gratia, which means 'for example'
fs	femtosecond ( $10^{-15}s$ )
FWHM	full width of the function that is reduced to one half of its maximum
HW1/ $e$ M	half width of the function that is reduced to $1/e$ of its maximum
HW1/ $e^2$ M	half width of the function that is reduced to $1/e^2$ of its maximum
i.e.	id est, which means 'that is' or 'that are'

IR	infrared
ps	picosecond ( $10^{-12}s$ )
resp.	respectively
rms	root mean square
SVEA	slowly varying envelope approximation
TEM	transverse electromagnetic
ZnS	zinc sulfide
ZnSe	zinc selenide

# 1 INTRODUCTION

## 1.1 Motivation of the Work

A couple years after J.A. Armstrong *et al.* [1] formulated the theory of an intensity dependent refractive index, the nonlinear optical properties of carbon disulfide were investigated [2]. Still today (e. g. [3]), the nonlinear refractive index characterization of the material is a topic of wide interest because CS<sub>2</sub> has a large nonlinear refractive index in comparison to other liquids as indicated through table 1.1. Consequently, it has been employed in optical switching [5], optical limiting [6] and beam filamentation [7] applications. Furthermore, carbon disulfide is often used as a reference material for optical nonlinearity measurements of other materials (as textbooks like [8, chap. 3] show). Especially in this application, it is indispensable to have available precise values in order to avoid propagating systematic errors.

The reason why the characterization of the nonlinear refractive index of CS<sub>2</sub> is still in progress after 45 years, originates from the fact that  $n_2$  is not constant but clearly dependent on the polarization and wavelength of light as well as the interaction time between light and matter. The motions of molecules, nuclei and electrons which are stimulated by external electric fields result in a temporal evolution of the material response. If short and intense laser pulses interact with a nonlinear material, even the pulse shape may become an important parameter in the determination of  $n_2$ . This multitude of dependencies considerably complicates the precise measurement of the material property and explains to some degree why a variety of  $n_2$  values, which are now and then clearly different, is published as partly shown in table 1.2.

Table 1.1: Several examples for the nonlinear refractive index of neat liquids.

Material	Wavelength ( $nm$ )	Pulse Duration ( $ps$ )	$n_2(10^{-16}cm^2/W)$
Benzene	532	30	129
Carbon disulfide	532	30	310
Chloroform	532	25	3.5
Toluene	532	25	6.7
Water	532	21	5.4

Examples are taken from R. L. Sutherland: *Handbook of Nonlinear Optics* [4], chapter 8, table 6. More examples and detailed references are presented there.

A timescale of particular interest is the femtosecond ( $10^{-15}s$ ) and low picosecond ( $10^{-12}s$ ) range due to the evolution of molecular motions within this range. The intention of this work is to provide experimental Z-scan data to characterize the nonlinear response of carbon disulfide on the mentioned timescale. The Z-scan is an experimental technique that was invented at the College of Optics and Photonics in 1989. It is a single beam measurement method that is explained in detail in chapter 2. In chapter 3 effective  $n_2$  values for Gaussian pulses are determined. These nonlinear refractive indexes were measured over an temporal range from about  $30fs$  to about  $2ps$ . In chapter 4, a theoretical model substitutes the variety of effective  $n_2$  values by parameterizing the nonlinear response so that it can be analytically described as a function of pulse duration for a particular wavelength. The validity of the presented model is tested through Z-scans with circularly polarized light in chapter 5. Theoretical ratios between the results of linearly and circularly polarized light are derived for the quasi instantaneous bound electron response and the slow diffusive molecular orientational response. The expression quasi instantaneous bound electronic response means that the electronic contribution to the nonlinear refraction is fully present independent of the pulse

Table 1.2: A selection of different  $n_2$  measurements of CS<sub>2</sub>

$n_2$ ( $10^{-15} \frac{cm^2}{W}$ )	pulse duration ( $fs$ )	$\lambda$ ( $nm$ )	method	reference
2.3	130	770	Z-scan	[9]
2.5	110	800	SPIDER	[10]
2.9	125	800	Z-scan	[3]
3.0	110	795	Z-scan	[11]
3.1	110	800	Z-scan	[10]
3.5	475	1054	Z-scan	[11]
4.7	100	800	time division interferometry	[12]
18.5	1000	800	Z-scan	[13]
32.0	$3 \cdot 10^5$	1054	Z-scan	[11]



duration. The theoretical ratios are experimentally checked and an additional ratio for the fast nuclear contribution to the nonlinear refractive index of CS<sub>2</sub> is determined. Finally, the impact of wavelength variations on  $n_2$  is measured for ultrashort laser pulses. The derived dispersion of the electronic response is presented in chapter 6.

## 1.2 Properties and Linear Characterization of Carbon Disulfide

Carbon disulfide is a linear, diatomic molecule, having the structural formula



where  $S$  denotes a sulphur and  $C$  the carbon atom. At room temperature and normal pressure the molecules assemble in the liquid phase which is synonymous to the fact that the material is optically isotropic. Due to the centro-symmetry of the molecule, it does not exhibit a permanent dipole moment. It has however two independent polarizability components,  $\alpha_{||}$  which is parallel to the molecular axis and the clearly smaller  $\alpha_{\perp}$  which is perpendicular to the molecular axis. Higher order permanent moments and polarizabilities are not of importance in the topics discussed in this thesis but can be found in the literature [14].

The neat liquid appears colorless and exhibits indeed a wide transparency range over the visible and near IR spectrum. Figure 1.1 shows the linear transmittance of the liquid for a 1mm cell that is used in the later described experiments and a thinner 100 $\mu$ m cell. Moreover, the UV absorption bands are resolved more clearly and are expressed in terms of the absorption cross section  $\sigma$ .

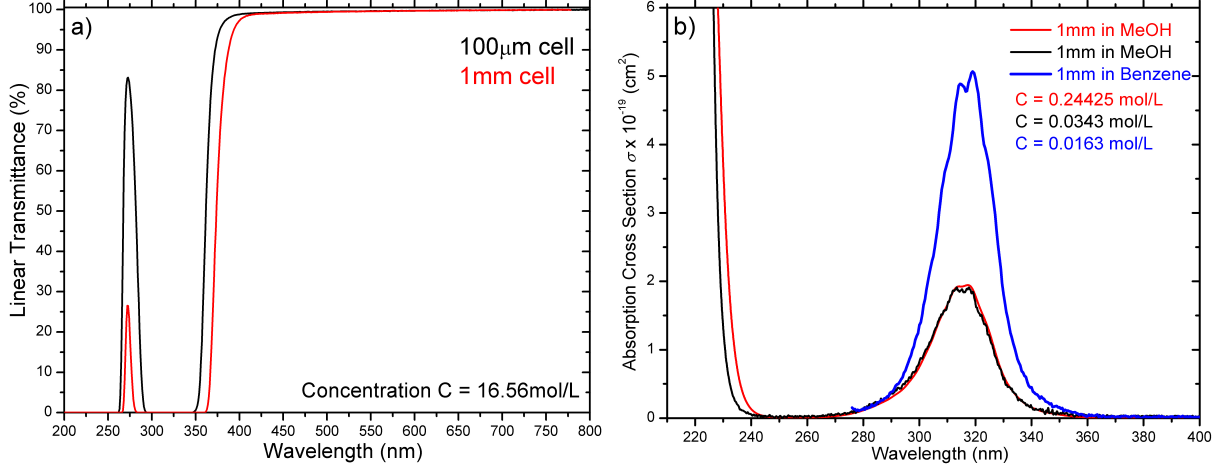


Figure 1.1: Linear transmittance and absorption spectrum, resp. of  $\text{CS}_2$

The transmittance spectrum a) shows that  $\text{CS}_2$  is transparent over the whole visible range. There is also no significant absorption in the near IR, in particular at  $\lambda = 1064\text{nm}$ . The absorption bands are further specified in b). Clearly, the absorption band from  $\approx 190$  to  $230\text{nm}$  is much stronger than the band from  $290$  to  $340\text{nm}$ .

### 1.3 The Nonlinear Refractive Index and Two-photon Absorption

Every material consists of electric charge carrying particles, i.e. negatively charged electrons and positively charged nuclei. Consequently, dipoles can be found or induced in every medium. The polarization  $\vec{P}(\vec{r}, t) = \frac{1}{2} (\vec{\mathcal{P}}(\vec{r}, t) + \vec{\mathcal{P}}^*(\vec{r}, t))$  describes the macroscopic volume density of electric dipoles in a material and represents the interaction between light and matter which is formally expressed as

$$\begin{aligned}
\frac{1}{2} (\mathcal{P}_i(\vec{r}, t) + \mathcal{P}_i^*(\vec{r}, t)) = \epsilon_0 \left[ \int_{-\infty}^{\infty} d\vec{r}' \int_0^{\infty} dt' \mathcal{R}_{ij}^{(1)}(\vec{r}', t') \frac{\mathcal{E}_j^{(*)}(\vec{r} - \vec{r}', t - t')}{2} \right. \\
+ \int_{-\infty}^{\infty} d\vec{r}' \int_{-\infty}^{\infty} d\vec{r}'' \int_0^{\infty} dt' \int_0^{\infty} dt'' \mathcal{R}_{ijk}^{(2)}(\vec{r}', \vec{r}'', t', t'') \frac{\mathcal{E}_j^{(*)}(\vec{r} - \vec{r}', t - t') \mathcal{E}_k^{(*)}(\vec{r} - \vec{r}'', t - t'')}{4} \\
+ \int_{-\infty}^{\infty} d\vec{r}' \int_{-\infty}^{\infty} d\vec{r}'' \int_{-\infty}^{\infty} d\vec{r}''' \int_0^{\infty} dt' \int_0^{\infty} dt'' \int_0^{\infty} dt''' \\
\left. \times \mathcal{R}_{ijkl}^{(3)}(\vec{r}', \vec{r}'', \vec{r}''', t', t'', t''') \frac{\mathcal{E}_j^{(*)}(\vec{r} - \vec{r}', t - t') \mathcal{E}_k^{(*)}(\vec{r} - \vec{r}'', t - t'') \mathcal{E}_l^{(*)}(\vec{r} - \vec{r}''', t - t''')}{8} \right. \\
\left. + \text{higher order terms} \right], \tag{1.2}
\end{aligned}$$

where the vector and tensor indexes, resp.  $i, j, k, l$  refer to any position vector component  $x, y, z$ . It is to note that expression (1.2) is written in Einstein notation. The integrals  $\int_{-\infty}^{\infty} d\vec{r}$  denote volume integrals and  $\int_0^{\infty} dt$  time integrals, the asterisks in brackets indicate that both complex electric field and its complex conjugated fields are part of the real polarization vector. All permutations must be summed up to describe the complete polarization. Based on the principle of causality, which is briefly explained in the [appendix A](#), the  $n^{th}$  order complex response function  $\tilde{\mathcal{R}}^{(n)}(\vec{r}, t)$ , which is a tensor of the order  $(n+1)$ , is zero for negative times. The complex electric field vector of the light interacting with the material is denoted by  $\vec{\mathcal{E}}(\vec{r}, t)$ . The higher order terms of the polarization are not important in the performed experiments due to sufficiently small peak irradiances and thus are not further specified.

The relatively small dispersion in the visible and near IR wavelength range of linear absorption spectrum of CS<sub>2</sub> implies that the linear term of equation (1.2) can be rewritten as

$$\mathcal{P}_i^{(1)}(\vec{r}, t) = \epsilon_0 \chi_{ij}^{(1)} \mathcal{E}_j(\vec{r}, t), \quad (1.3)$$

where  $\chi^{(1)}$  is the complex linear susceptibility. The second term cancels for CS<sub>2</sub> because of the optical isotropy of liquids [15, chap. 1]. Eventually, the third term describes nonlinear refraction and absorption. It can be considerably simplified in the case of carbon disulfide because the macroscopic spatial homogeneity of the liquid eliminates the necessity of spatial integration. Moreover, the sample under test was only illuminated by one input field, hence the nonlinear polarization reads

$$\mathcal{P}_i^{(3)}(\vec{r}, t) + c.c. = \frac{\epsilon_0}{4} \int_0^{\infty} dt' \mathcal{R}_{ijkl}^{(3)}(t') \mathcal{E}_j^{(*)}(\vec{r}, t - t') \mathcal{E}_k^{(*)}(\vec{r}, t - t') \mathcal{E}_l^{(*)}(\vec{r}, t - t'). \quad (1.4)$$

The complex electric fields can be decomposed into a time and position dependent envelope  $\mathcal{A}(\vec{r}, t)$  and a carrier term  $\exp\{i(kz - \omega_0 t + \varphi)\}$ , where

$$k := \frac{2\pi n_0}{\lambda} \quad (1.5)$$

is the wavenumber and  $\omega_0$  the carrier frequency. The complex electric field components read

$$\mathcal{E}(z, t) = \mathcal{A}(\vec{r}, t) e^{i(kz - \omega_0 t)}. \quad (1.6)$$

The light transmitted through the sample does not change its frequency in the case of refraction or absorption. Therefore, the polarization is required to oscillate with the carrier frequency as well.

It will be referred to the integral (1.4) in later sections. However, in order to introduce nonlinear refraction as well as absorption, it is much more instructive to consider the special case of an instantaneous material response and linear polarized light. The third order polarization simplifies to

$$\mathcal{P}_x^{(3)}(\vec{r}, t) = \frac{3}{4} \epsilon_0 \chi_{xxxx}^{(3)} \mathcal{A}_x(\vec{r}, t) \mathcal{A}_x^*(\vec{r}, t) \mathcal{A}_x(\vec{r}, t) e^{i(kz - \omega_0 t)}. \quad (1.7)$$

The factor 3 represents the number of permutations of the electric fields that allow the polarization to oscillate with the carrier frequency of the input. Only the component  $\chi_{xxxx}^{(3)}$  of the third order susceptibility tensor is of importance under the described assumptions.

The propagation of the light can be described by the reduced wave equation which takes the form [15, chap. 2]

$$\frac{\partial^2 \mathcal{E}_i}{\partial z^2} - \frac{n_0^2}{c^2} \frac{\partial^2 \mathcal{E}_i}{\partial t^2} = \frac{1}{\epsilon_0 c^2} \frac{\partial^2 \mathcal{P}_i^{(3)}}{\partial t^2} \quad (1.8)$$

where  $\epsilon_0$  is the vacuum permittivity,  $c$  is the vacuum speed of light and the linear refractive index is defined as

$$n_0 := \Re \left\{ \sqrt{1 + \chi^{(1)}} \right\} \overset{\text{CS}_2}{\approx} \sqrt{1 + \chi^{(1)}}. \quad (1.9)$$

A central wavelength of  $\lambda = 700\text{nm}$  implies the duration of an optical cycle of  $T \approx 2.3\text{fs}$ . Since the pulse duration, i.e. the width of the envelope  $\mathcal{A}(t)$ , of the light that was generated by the used laser system was at least ten times longer, it is appropriate to apply the slowly varying envelope approximation (SVEA) [16, chap. 1] to the electric fields and the polarization so that the upper equation (1.8) simplifies to

$$e^{i\omega_0 t} \frac{\partial}{\partial z} \mathcal{A}(\vec{r}, t) = i \frac{\omega^2}{2\epsilon_0 c^2 k} \mathcal{P}_i^{(3)}. \quad (1.10)$$

It is to note that this equation holds only in a reference frame that travels with the phase velocity of the central wavelength of the laser pulse. The detailed derivation can be reviewed in the [appendix B](#). To solve the differential equation, the function  $\mathcal{A}(\vec{r}, t)$  is decomposed into its amplitude  $A(\vec{r}, t)$  and its phase  $\phi(\vec{r}, t)$ . Plugging expression (1.7) into (1.10) reads

$$e^{i\phi} \frac{\partial A}{\partial z} + i A e^{i\phi} \frac{\partial \phi}{\partial z} = i \frac{\omega^2}{\epsilon_0 c^2 k} \cdot \frac{3}{8} \epsilon_0 \chi_{xxxx}^{(3)} |A|^2 A e^{i\phi}. \quad (1.11)$$

### 1.3.1 The Nonlinear Refractive Index

The nonlinear refractive index describes the irradiance dependent phase change of light that travels through a sample of length  $L$ . From equation (1.11), it is found

$$\Delta\phi = \int_0^L dz \frac{3\omega_0^2 \Re \left\{ \chi_{xxxx}^{(3)} \right\}}{8c^2 k} A^2(\vec{r}, t) \quad (1.12)$$

For a thin sample and a weak absorber the approximation that  $\frac{\partial A^2(\vec{r}, t)}{\partial z} \approx 0$  is justified. Moreover, the irradiance  $I$  is

$$I(\vec{r}, t) = \frac{n\epsilon_0 c}{2} |\mathcal{A}(\vec{r}, t)|^2 = \frac{n\epsilon_0 c}{2} A^2(\vec{r}, t) \quad (1.13)$$

and the substitutions

$$k = \frac{\omega_0 n_0}{c}, \quad k_0 = \frac{\omega_0}{c} \quad (1.14)$$

are made, so that the nonlinear refraction is described by

$$\Delta\phi = (n_2 I) \cdot k_0 L = \Delta n \cdot k_0 L \quad (1.15)$$

where  $n_2$  is the so-called *nonlinear refractive index* that is related to the real part of the nonlinear susceptibility through

$$n_2 := \frac{3\Re\{\chi_{xxxx}^{(3)}\}}{4n_0^2\epsilon_0 c} \quad (1.16)$$

for a linear polarized one beam input and an instantaneous material response.

### 1.3.2 Two-photon Absorption

If the real parts of the left-hand and right-hand side of equation (1.11) are compared, an expression for the two-photon absorbing process is found which is in particular of importance for determining beam properties (cf. section 3.1). Through expanding the differential equation by the factor  $2A(\vec{r}, t)$ , the equation representing two-photon absorption reads

$$\frac{\partial A^2(\vec{r}, t)}{\partial z} = -\frac{3\omega_0 \Im\{\chi_{xxxx}^{(3)}\}}{4n_0 c} A^4(\vec{r}, t) \quad (1.17)$$

Applying expression (1.13) and defining the *two-photon absorption coefficient*

$$\beta := \frac{3}{2} \frac{\omega_0 \Im \{ \chi_{xxxx}^{(3)} \}}{n_0^2 \epsilon_0 c^2} \quad (1.18)$$

transforms equation (1.17) to

$$\frac{\partial I(\vec{r}, t)}{\partial z} = -\beta(\omega_0) I^2(\vec{r}, t). \quad (1.19)$$

Consequently, the irradiance drops within a sample of length  $L$  to

$$I(L, x, y, t) = \frac{I(0, x, y, t)}{1 + \beta L I(0, x, y, t)} \quad (1.20)$$

where  $I(0, x, y, t)$  is the input irradiance. Again, this result is only correct if the assumptions stated in this section are valid and linear absorption is negligible.

## 2 EXPERIMENTAL TECHNIQUE

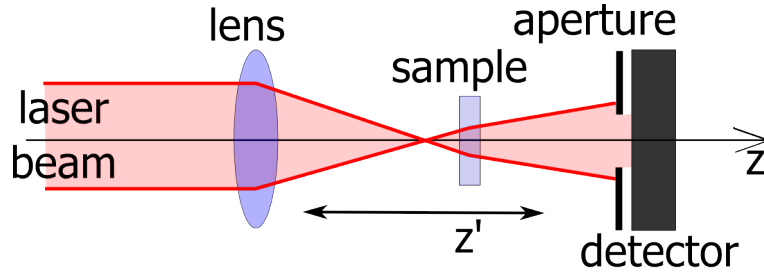
### 2.1 The Z-scan

#### 2.1.1 *Fundamental Idea*

The performed experiments were all done by means of the Z-scan technique which was invented at CREOL, The College of Optics and Photonics in 1989 [17]. By now, the method to measure third and fifth order nonlinearities is widely used and the original publication that introduces its fundamental theory [18] is cited more than 3000 times. The idea of Z-scan is based on the change of the laser beam irradiance along its propagation direction which alters the magnitude of the material's nonlinear response according to equations (1.15) and (1.20). Focused laser light exhibits high peak irradiances at the beam waist as well as a fast beam divergence. Thus, a sample is placed behind a lens and shifted with respect to the focal position, in other words: scanned along the z-axis. The induced change of the magnitude of multi-photon absorption or self focusing is measured at a detector behind the sample. While the absorbance of the sample is determined from the power ratio between the light that is incident on the sample and the light that is transmitted through the sample, the magnitude of self focusing must be derived from the beam size at a particular position  $z''$ . Knowing the radial distribution of the laser beam and setting a radially symmetric aperture at position  $z''$  allows to obtain the amount of nonlinear refraction that is introduced by the sample under test. The essential procedure is animated in media 2.1.

The main advantages of the Z-scan method are simplicity and sensitivity. The technique





A digital version of the thesis shows an animation after clicking the figure.  
A Flash player is required to play the clip.

Media 2.1: The concept of Z-scan.

The detector signal changes dependent on the sample position  $z'$ .

is relatively simple because it is based on the effects of self action, i.e. the central frequency of the incoming and outgoing light field does not change. Therefore, no phase matching is necessary like in third harmonic generation measurements, which makes the technique applicable to a wide range of materials. Moreover, the basic Z-scan is a single beam experiment. While optical Kerr effect and degenerate four wave mixing experiments require the spatial and temporal overlap of at least two beams, Z-scan only requires to align the aperture with respect to the z-axis properly. Furthermore, only one Z-scan may reveal magnitude and sign of the samples nonlinear refractive index and the multi-photon absorption coefficient.

Nonlinear phase distortions can be measured with interferometric sensitivity which can be explained by the fact that the setup is comparable to a single beam interferometer as illustrated in figure 2.1. The sensitivity increases with a decreasing aperture radius [18]. A good compromise between sensitivity and signal to noise ratio was found by allowing one third of the laser power passing through the aperture if no nonlinear refraction occurs.

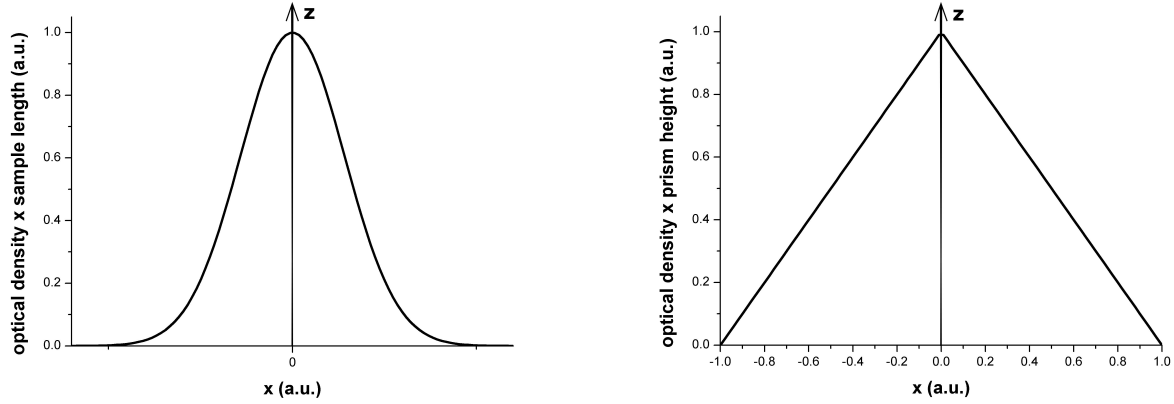


Figure 2.1: Induced single beam interferometer.

*Left:* Induced optical resistance distribution in the Z-scan setup for a Gaussian beam. The wings of the beam travel faster through the sample than the central part.

*Right:* Optical resistance distribution of a classical Fresnel biprism interferometer. The higher  $|x|$  the less optical resistance the light has to overcome as in the previous case.

### 2.1.2 Z-scan Theory for Thin Samples

For Gaussian pulses which are in good approximation generated by the laser system described in section 2.2, the complex electric field takes the form

$$\mathcal{E}(z, r, t) = \frac{A_0}{\sqrt{1 + \frac{z^2}{z_0^2}}} \cdot \exp \left\{ -\frac{r^2}{w_0^2 \left(1 + \frac{z^2}{z_0^2}\right)} - \frac{ikr^2}{2z \left(1 + \frac{z_0^2}{z^2}\right)} - \frac{t^2}{\tau_G^2} + i\phi(z, t) \right\} \quad (2.1)$$

and according to equation (1.13) the irradiance reads

$$I(z, r, t) = \frac{I_0}{1 + \frac{z^2}{z_0^2}} \cdot \exp \left\{ -\frac{2r^2}{w_0^2 \left(1 + \frac{z^2}{z_0^2}\right)} - \frac{2t^2}{\tau_G^2} \right\} \quad (2.2)$$

where  $z$  is the distance to the beam waist location along the propagation axis,  $r$  is the radial distance to the peak of the pulse,  $t$  is the time delay with respect to the peak of the pulse,  $I_0$  is the peak irradiance

$$I_p = \frac{I_0}{1 + \frac{z^2}{z_0^2}} \quad (2.3)$$

at  $z = 0$ ,  $w_0$  is the beam waist, defined as beam radius of  $(I_0 \cdot e^{-\frac{2t^2}{\tau_G^2}})/e^2$  irradiance (HW1/ $e^2$ M),  $z_0$  is the Rayleigh length or Rayleigh range which is defined as the location  $z$  where  $I_p(z_0) = \frac{1}{2}I_0$  and can be expressed as

$$z_0 = \frac{\pi w_0^2}{\lambda}. \quad (2.4)$$

$\tau_G$  is HW1/ $e^2$ M with respect to the Gaussian temporal intensity shape. However, it is usually referred to the shape independent *pulse duration*  $\tau_p$  which is defined as FWHM of the temporal intensity shape of a laser pulse. The pulse duration is connected to  $\tau_G$  through the relation

$$\tau_p = \sqrt{2 \cdot \ln 2} \tau_G. \quad (2.5)$$

Moreover, the  $z$ -dependent *beam width* is defined as

$$w(z) = w_0 \sqrt{1 + \frac{z^2}{z_0^2}}. \quad (2.6)$$

The expression *thin sample* is derived from the fact that the sample length  $L$  must be shorter than the Rayleigh range  $z_0$  in order to assume constant peak irradiance over the sample length. Furthermore, the approximation is only valid if the nonlinear light matter interaction is small such that the shape of a laser pulse is not significantly changed. Through preparing samples with less than  $1mm$  length and not allowing signals to deviate more than 15% from the nonlinear interaction free detector signal, the conditions for the upper approximations were generally fulfilled.

In the case of pure nonlinear refraction, the sample induced phase distortion of the pulse

can be described as

$$\Delta\phi(z, r, t) = \frac{n_2 I_0 k_0 L_{eff}}{1 + \frac{z^2}{z_0^2}} \cdot \exp \left\{ -\frac{2r^2}{w_0^2 \left(1 + \frac{z^2}{z_0^2}\right)} - \frac{2t^2}{\tau_G^2} \right\} \quad (2.7)$$

according to equation (1.15). The more general effective length  $L_{eff}$  is used instead of the physical sample length  $L$  in the upper equation. The effective length takes into account the linear absorption effects and is defined as [18]

$$L_{eff} = L \frac{(1 - T_{lin})}{\ln(1/T_{lin})} \quad (2.8)$$

where  $T_{lin}$  is the linear transmittance that is  $T \approx 99.9\%$  for a 1mm CS<sub>2</sub> sample. Consequently, the physical length is reduced by about  $0.5\mu m$  which is negligible.

The light field  $\mathcal{E}_e(z, r, t)$  emerging from the sample under test must be propagated to the aperture in order to derive its beam size at this particular location. Within the thin sample approximation the electric field at the sample position  $z'$  is

$$\mathcal{E}_e(z', r, t) = \mathcal{E}(z' - L, r, t) \cdot e^{-i\Delta\phi(z', r, t)} \quad (2.9)$$

where the sign of the exponent is in agreement with the radius dependent phase term in equation (2.1). Otherwise, the correct sign of the nonlinearity cannot be extracted from the analysis.

Wearie et al. [19] proposed to propagate the terms of the exponential power series solely in order to reduce the electrical field to a sum of Gaussian beams which can be analytically propagated [20]. The electric field at the aperture plane, which is situated at the distance

$z = d$ , reads

$$\begin{aligned} \mathcal{E}_a(d, r, t) = \mathcal{E}(z' - L, 0, t) \sum_{m=0}^{\infty} \frac{[-i\Delta\phi_0]^m}{m! \cdot \sqrt{1 + \frac{d^2}{d_m^2}}} \\ \cdot \exp \left\{ -\frac{r^2}{w_m^2(d)} - \frac{ikr^2}{2d(1 + d_m^2/d^2)} + i \arctan(d/d_m) \right\} \end{aligned} \quad (2.10)$$

where  $d_m$  is the Rayleigh length and  $w_m(d)$  is the beam size of the  $m^{th}$  Gaussian component.

The phase distortion  $\Delta\phi_0$  is defined as

$$\Delta\phi_0 = \frac{n_2 I_0 k_0 L}{1 + \frac{z'^2}{z_0^2}} \quad (2.11)$$

It turns out that the higher order and fast diverging Gaussians only have a small impact on the detector signal, for the beam size is expressed as

$$w_m(d) = w_0 \cdot \sqrt{\frac{1 + d^2/d_m^2}{2m + 1}}. \quad (2.12)$$

Therefore, only several low order terms have to be taken into account in order to calculate the signal the detector should display. Eventually, the measured Z-scan transmittance is calculated by [18]

$$T_{n_2}(z') = \frac{4 \int_{-\infty}^{\infty} \int_0^{r_a} |\mathcal{E}_a(d, r, t)|^2 r dr dt}{S w_0^2 \int_{-\infty}^{\infty} |\mathcal{E}(t)|^2 dt} \quad (2.13)$$

where

$$S = 1 - e^{-2r_a^2/w_0^2(d)} \quad (2.14)$$

is the linear aperture transmittance and  $r_a$  is the aperture radius.

In the case of two-photon absorption measurements the aperture is opened such that  $S \equiv 1$ .

The propagation of the beam emerging from the sample is unnecessary but the transmittance

dependence on the sample position  $z'$  must be described. The power at the detector is

$$\begin{aligned} P(d, t) &= 2\pi T_{lin} \int_0^\infty dr r \frac{I(z', r, t)}{1 + \beta L_{eff} I(z', r, t)} \\ &= T_{lin} \cdot \frac{\pi w_0^2 (1 + z'^2/z_0^2)}{2\beta L_{eff}} \ln(1 + \beta L_{eff} I(z', t)) \end{aligned} \quad (2.15)$$

according to equation (1.20). Finally, the sample transmittance reads

$$T_{2PA}(z') = \frac{(1 + z'^2/z_0^2)}{\sqrt{\pi}\beta L_{eff} I_0} \cdot \int_{-\infty}^\infty dt' \ln \left( 1 + \frac{\beta L_{eff} I_0 e^{-t'^2}}{1 + z'^2/z_0^2} \right). \quad (2.16)$$

Further calculation details are shown in [appendix C](#). If the signal is altered by effects resulting from a finite aperture size, the measurement is denoted by the term *closed* aperture Z-scan while the nonlinear absorption measurements are called *open* aperture Z-scans.

## 2.2 Experimental Setup

### 2.2.1 Ultrafast Laser

The short pulses are generated by a commercial laser system of the Clark-MXR CPA series (model 2001). The laser operates at  $\lambda = 778.5nm$  and  $1kHz$  repetition rate in the Gaussian shaped TEM<sub>00</sub> mode. The energy of the generated  $\tau_p = 140fs$  pulses is about  $1mJ$  which corresponds to an average power of  $\bar{P} = 1W$  and a pulse peak power of  $P_p = 6.7GW$ .

In principle, the system consists of an oscillator, a pulse expander, a regenerative amplifier and a pulse compressor. The resonator consists of an  $Er^{3+}$ , i.e. erbium-doped fiber which is pumped by a diode laser operating at  $\lambda = 980nm$ . The oscillator is passively mode-locked through the method of stretched-pulse polarization rotation additive mode-locking which was originally proposed by K. Tamura *et al.* [21]. The polarization rotation in the fiber is induced by self as well as cross phase modulation which is based on the effect of nonlinear

refraction. The pulse dispersion of linear polarized output is compensated and the light is frequency doubled in a periodically poled lithium niobate crystal. Doped fiber oscillators have several advantages. They are very compact and provide high gain as well as a large gain bandwidth which allows relatively low pump powers and makes  $fs$ -pulse generation possible. Another important property is the stability of mode-locked fiber lasers in the case of good temperature control.

In order to make the short pulses very intense, the principle of chirped pulse amplification [22] is applied. By means of a transmission grating pair, spectral phase is added to the short pulses in order to expand them and decrease their peak power. Some of the longer pulses are picked by a polarization controlling Pockels cell and sent into another cavity. An  $Al_2O_3$ , i.e. sapphire crystal doped with optical active  $Ti^{3+}$ , i.e. titanium ions serves as the active medium of the regenerative amplifier. The isolated ions have a broad fluorescence spectrum that provides optical gain over a wavelength range of about  $\Delta\lambda = 400nm$  [23, chapt. 9] which is very favorable for broadband short pulse generation. The crystal is pumped with light of  $\lambda = 532nm$  from a Q-switched frequency doubled neodymium:YAG laser. The advantage of the active crystal is the opportunity to reach  $fs$ -pulse energies in the  $mJ$ -range. After several round trips the amplified pulses leave the Q-switched cavity and are compressed again by another transmission grating to reach their output duration of  $140fs$ .

### **2.2.2 Optical Parametric Amplifier**

The operating wavelength is selected by the commercial optical parametric amplifier TOPAS-C that is tunable from  $\lambda_{min} = 1140nm$  to  $\lambda_{max} = 2600nm$ . A small percentage of the incoming laser beam is used to generate parametric superfluorescence in a BBO crystal. This effect occurs if quantum noise is amplified by phase-matched  $\chi^{(2)}$ -based three wave mixing processes [24] or in other words if a pump photon of energy  $\hbar\omega_p$  decays into a signal

photon of energy  $\hbar\omega_s$  and an idler photon of energy  $\hbar\omega_i$  where

$$\omega_p = \omega_s + \omega_i. \quad (2.17)$$

The generated signal photons are used as seed for a preamplification process that is initiated by a first pump beam that is collinearly overlapped with the superfluorescence seed to stimulate the three wave mixing process. A stable and relatively intense (in comparison to the superfluorescence spectral component) seed pulse is created that is strongly amplified by another pump pulse from the CPA laser system.

The signal wavelength is selected by means of the crystal orientation. For  $\chi^{(2)}$ -processes the phase-matching between amplified and pump beam is crucial for noticeable conversion efficiencies. Since BBO is birefringent the phase-matched wavelength is set by the effective refractive index of the extraordinary polarized light.

During the parametric amplification the pump pulse properties are approximately maintained and thus the signal pulse duration is similar to that of the laser system. According to the manufacturer, the output stability of the commercial parametric amplifier is supposed to be lower than 2% rms. This is an important factor for efficiently generating the second harmonic of the TOPAS output which is necessary to access the visible and near-IR spectrum where the presented measurements were taken.

### **2.2.3 Prism Compressor**

The pulse duration is varied by means of a prism pair. The principle of this dispersive element is illustrated in figure 2.2. Broadband laser pulses are incident on prism 1 in the Brewster angle to minimize Fresnel losses. Since the utilized SF10 glass prisms exhibit normal dispersion, the shorter wavelength parts of the spectrum are stronger refracted than the longer wavelengths. The pulse spectrum is spatially resolved behind prism one. The stronger the refraction the longer the distance to the surface of the second prism which is



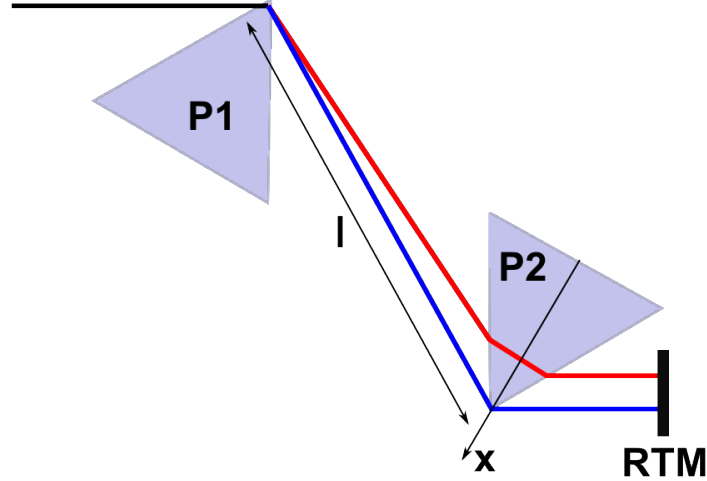


Figure 2.2: Setup of a prism compressor.

P1, P2: prisms, RTM: rooftop mirror,  $l$ : apex distance,  $x$ : translation axis of P2

effective anomalous dispersion. On the other hand, the longer wavelengths travel through more glass of prism two which results in additional normal dispersion. Taking both effects into account, it can be shown that the effective dispersion can be negative [25] depending on the parameters  $l$  and  $x$  (cf. figure 2.2). Increasing the apex distance leads to more anomalous dispersion while increasing  $x$  enhances the normal dispersion. In addition, the finite beam size has to be considered and thus also the distance the light travels through the first prism. Experimentally, the peak open aperture Z-scan signal, which scales with the pulse duration (cf. equation (2.16)), is used to adjust the apex distance roughly. In order to generate long pulses, the distance  $l$  is increased continuously, the fine adjustment is done afterwards by changing  $x$ . The longest obtained pulse duration is  $2.3\text{ps}$ . A further increase of the distance between the prisms was not possible for the pulse energy losses were too high. Subsequently, the signal-to-noise ratio was so low that the transmittance signal of the Z-scan could not be analyzed anymore.

#### 2.2.4 Complete Setup

The complete laboratory setup is sketched in figure 2.3. The beam expander and the first iris

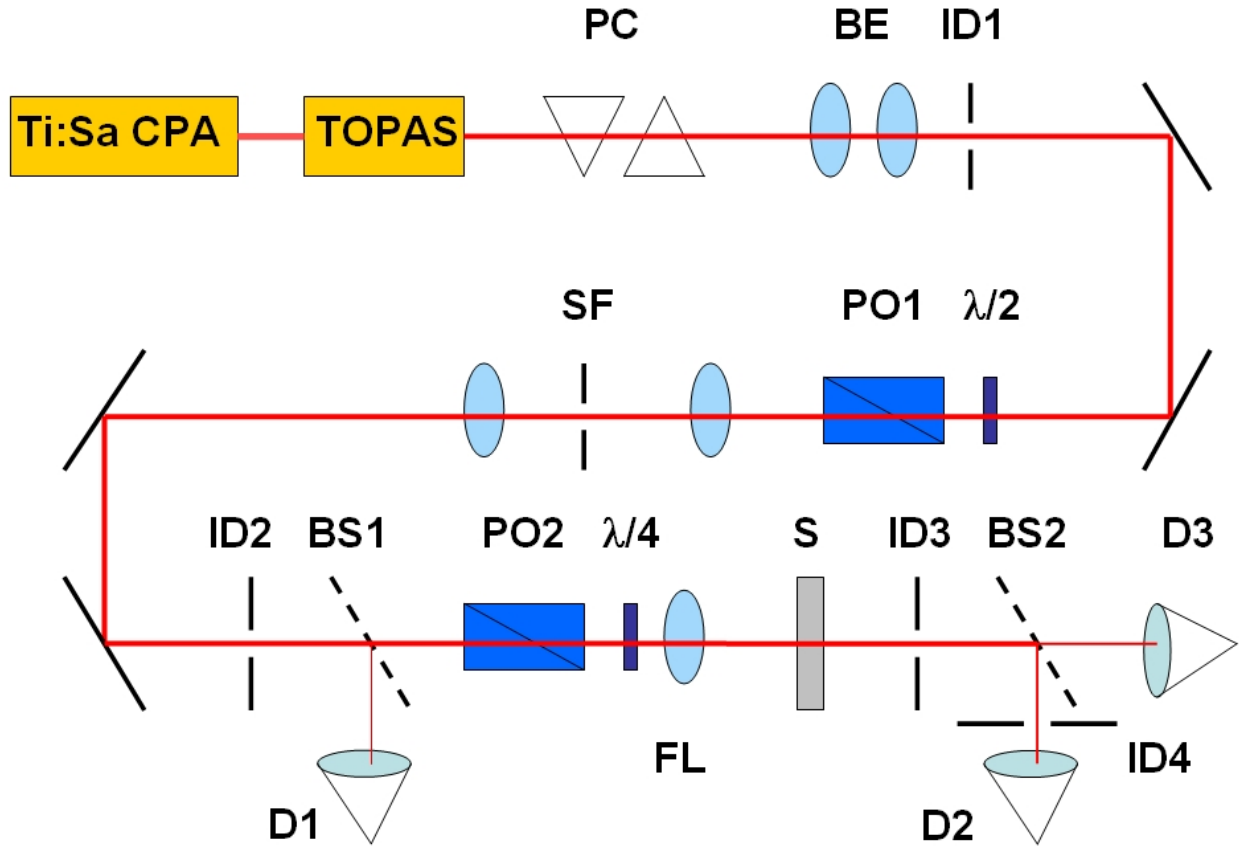


Figure 2.3: Complete Z-scan Setup.

Ti:Sa CPA - Clark MXR CPA laser system, TOPAS - optical parametric amplifier, PC - prism compressor, BE - beam expander, ID1, ID2, ID3, ID4 - iris diaphragms,  $\lambda/2$  - half-wave plate, PO1, PO2 - linear polarizers, SF - spatial filter, BS1, BS2 - beam splitter,  $\lambda/4$  - zeroth order quarter-wave plate, FL - focusing lens, S - sample and D1, D2, D3 - photodiode detectors.

diaphragm are used to select a clean Gaussian beam profile. The incoming beam is disturbed by the multitude of parametric processes which makes cleaning advisable. The beam shape is checked by means of the beam profiler. At long pulse durations ( $\tau_p > 1.1ps$ ), not enough energy is available to include the beam expander and hence those optical elements were removed. The half-wave plate and polarizer one are used to adjust the pulse energy. The retardation plate rotates, depending on the orientation of its fast and slow axis, the electric field vector. This vector is projected onto the polarization axis of PO1 which leads to an effective amplitude change of the linearly polarized light. The spatial filter consists of a focusing and a collimating lens as well as a pinhole which is placed at the beam focus location. Pinholes of  $120\mu m$  and  $180\mu m$  were used. The iris diaphragms 2 and 3 were basically used to align the Z-axis properly which is crucial for the closed aperture scans. Polarizer PO2 and the quarter-wave plate were only inserted into the setup during the measurements that should reveal the tensor nature of the nonlinear response (cf. chapter 5). The second polarizer ensures that linearly polarized light enters the retardation plate. The  $\lambda/4$ -plate is of zeroth order and is recommended for a wavelength range from  $700nm$  to  $1550nm$ . The ellipticity of the light was smaller than 5% in the case of quasi linear polarized light and higher than 90% in the case of quasi circular polarization. Focusing lenses of  $15mm$  and  $25mm$  focal length were used to observe nonlinear refraction and absorption at high signal-to-noise ratios. The sample is shifted along the z-axis by means of a computer controlled motor that rotates a fine adjustment screw of a Klinger Scientific translation stage. The beam splitter one sends a small percentage of the beam energy to a reference detector. Dividing the signal by the reference reduces the error caused by pulse energy fluctuation. The iris diaphragm 4 is adjusted to a radius  $r_a$  that corresponds to a linear aperture transmittance of  $S = 0.33$  which has proved as a good compromise of measurement sensitivity and signal-to-noise ratio. Detector 2 measures the closed and detector 3 the open aperture signal. In the case of the polarization measurements beam splitter 2 was replaced by a mirror in order to eliminate the polarization dependence of the beam splitter.

### **2.2.5 Alignment Procedure**

In order to measure data that is comparable to the theoretical curves, alignment is absolutely crucial. It is necessary to make sure that the beam after the beam expander and the spatial filter is well collimated which was checked by means of two mirrors that projected the beam on a wall of the lab at an optical distance of about 10m. The pinhole position can be aligned by means of a x-y-z translation stage. A maximal throughput and a symmetrical beam spreading upon small misalignment is adjusted in order to optimize the filtering of higher order spatial frequencies. The iris diaphragms indicate the direction of the z-axis. The beam is centered at these apertures before the optical elements along the z-axis are placed into the setup. The beam profile camera, placed behind the second aperture ID3, allows to align the central position very precisely. The optical elements, lens, if necessary quarter-wave plate and polarizer, are afterwards gradually inserted into the setup. The back reflection of the elements is checked first in order to avoid tilt and consequently beam walk-off. Afterwards, the x-y location of the lens is adjusted such that the beam profile behind the aperture ID3 remains concentric. All of these alignment are double-check by means of the beam profiler. Next, the sample is inserted in the far field, i.e. no nonlinearities can be detected at this sample location. The sample is just tilted enough that its back reflections are not detected. Of course, the symmetry of the beam behind the iris diaphragm must be maintained. Finally, the beam splitter BS2 is adjusted such that the beam is centered at the aperture ID4 as well.

## **2.3 Application of Gaussian Quadrature in the Data Analysis Algorithm**

As section 2.1.2 has shown, it is necessary to solve integrals numerically in order to compare theoretical Z-scan curves with numerical data. This is in particular a computational issue in the case of the closed aperture Z-scan where integrations over space and time are performed. In order to reduce the time consumption of an accurate data fit, fast integration algorithms

must be applied. The Z-scan analysis contains integrals of quite similar functions which do not have any singularities because of their physical origins. These properties lead to the opportunity to apply Gaussian quadrature algorithms instead of the conventional trapezoidal rule, Simpson's rule or Romberg's method.

Every integral

$$\int_{-1}^1 f(x)dx \quad (2.18)$$

can be solved exactly by the quadrature

$$\sum_{k=1}^n w_k f(x_k) \quad (2.19)$$

if  $f(x)$  is a polynomial of the order  $2n - 1$  [26]. The idea of the Gaussian quadrature is to find the weights  $w_k$  and abscissas  $x_k$  which establish the equivalence of (2.18) and (2.19). The interval  $[-1, 1]$  can be extended by variable substitutions to an arbitrary interval of integration, such that even improper integrals can be solved. The choice of the weights depends on the endpoints of the integration. In the Z-scan analysis program two weighting formulas are used

- Gauss-Legendre formulas for the intervals  $[0, r_a]$  and
- Gauss-Hermite formulas for the interval  $(-\infty, \infty)$ .

The weights and abscissas are tabled in the "Handbook of Mathematical Functions" by M. Abramowitz and I. A. Stegun [27] for both integral types. However, the book also presents analytic expressions for  $w_k$  so that values were calculated numerically to determine an optimal number of integration points. For the Gauss-Legendre integration, 25 points are calculated and 12 for the Gauss-Hermite integration. These were saved in a text file which is loaded at the launch of the analysis program. The example  $\int_0^1 \exp(-x^2)dx$  in figure 2.4 shows how fast the Gaussian quadrature converges to the correct value.

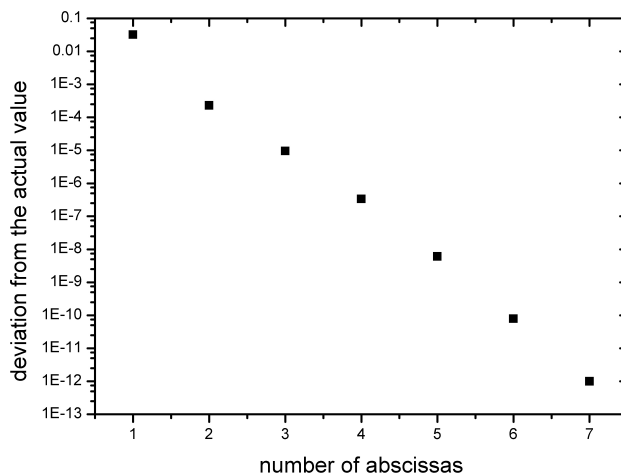


Figure 2.4: Convergence of the Gaussian quadrature algorithm up to a precision of  $10^{-12}$ .

The example  $\int_0^1 \exp(-x^2)dx = 0.746824132812 + \mathcal{O}(10^{-13})$  shows how fast the Gaussian-Legendre quadrature converges. Only eight points are necessary to obtain the arbitrarily chosen precision.

Introducing these algorithms into the data analysis program has made it possible to apply automatic least square fitting routines to the taken raw data. Consequently, measurement uncertainties are reduced and the applicability of the parametrization of the temporal response can be evaluated.

## 3 PULSE WIDTH DEPENDENCE OF THE NONLINEAR REFRACTION IN CS<sub>2</sub>

### 3.1 The Measurement Procedure

After aligning the setup, the pulse energy is adjusted by means of rotation of the half-wave plate. The maximal change in transmittance is usually supposed to be more than 2% and less than 10% in order to gain a signal that reproduces all features of the material's third order nonlinearity but does not violate the thin sample assumptions discussed in section 2.1.2 or exhibit features of higher order nonlinearities. The energy is measured with a power meter behind the focusing lens in the z-axis to calibrate the reference detector. Neutral density filters in front of the detectors are set such that the readings are never below 1V or above 3V. The detectors respond linearly within this range as figure 3.1 shows. An average pulse energy as well as reference detector signal is determined by taking 5000 data points. During the measurements, energy fluctuations are limited by acquiring data only if the reference signal differs less than 2% from the its previously determined average.

The Z-scan is usually performed at two or three spots on the sample (i.e. different x-y positions of the sample) to exclude errors due to inhomogeneities. The impact of inhomogeneities is especially present in the open aperture semiconductor scans. Figure 3.2 shows an example where two different spots reveal significantly distinct beam parameters. Moreover, the pulse energy is varied to assure that no higher order effects are present. Per sample location  $z'$ , 50 data points are taken and averaged. Resembling curves of different spots are averaged,

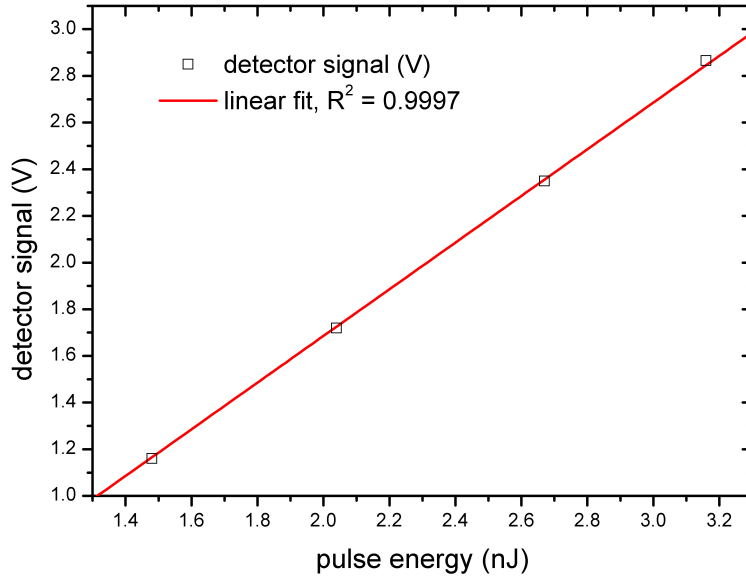


Figure 3.1: The linearity of the photo detectors.

The slope of the fitted line is  $1V/nJ$ .

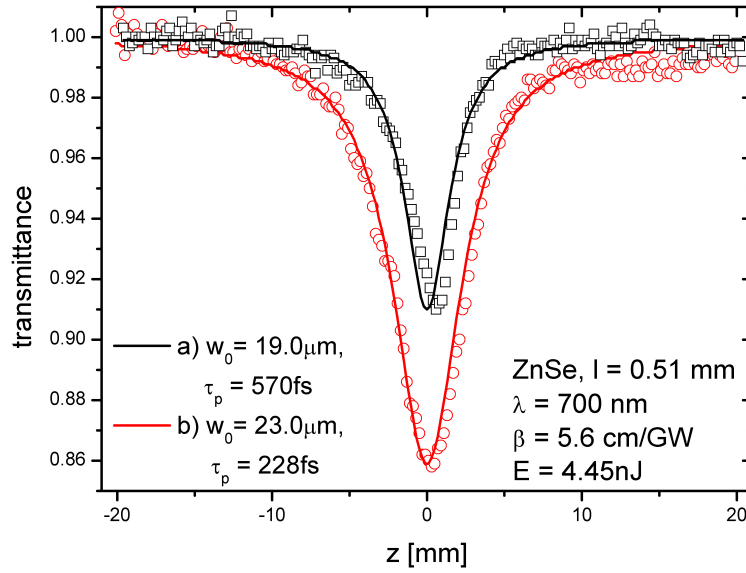


Figure 3.2: Effects of sample inhomogeneities.

The only difference between these measurements is the spot where the light beam hits the ZnSe sample. Case a) is reproducible at other spots and thus case b) is omitted in further evaluation.



too. Data is acquired for 200 sample locations  $z'$  during each Z-scan. The scan range is 4cm which assures that the sample is measured in the far field behind as well as in front of the focus.

Before comparing computed curves and measured data, the detector signal must be normalized. The Z-scan theory of chapter 2.1.2 is based on the fact that the transmittance signal is one if no nonlinearities occur. All linear losses behind the sample do not have to be analyzed, but the signal in the far field position must be normalized to one. Moreover, the point of minimal transmittance is shifted to  $z = 0$  in the case of an open aperture scan since the beam waist is minimal at this location and thus the two-photon absorption is maximal. In the case of nonlinear refraction, the unity transmittance point between peak and valley of the signal is shifted to  $z = 0$  which is plausible if the optical power of a thick lens is considered:

$$\Phi = \Phi_1 + \Phi_2 - d\Phi_1\Phi_2 \quad (3.1)$$

where the optical power  $\Phi$  is the inverse of the focal length. If the sample location is at  $z = 0$  and the light illuminating the focusing lens is collimated, the lens thickness is  $d = 1/\Phi_1$  and thus

$$\Phi = \Phi_1 \quad (3.2)$$

which is equivalent to the systems optical power if the sample is in the far field. After the normalization is done by eye, the theoretical curves computed by equations (2.13) and (2.16), resp. are fitted to the acquired data. Since the beam waist determines the beam divergence, the open and closed aperture Z-scan signal is clearly more sensitive to a change of the beam waist than to a change of pulse duration and refractive index, resp. Consequently, the beam waist is determined by the shape of the open and the closed aperture signal. Although this is done by eye, a measurement uncertainty of less than  $\pm 0.5\mu m$  is justified. An example for the

determination of the beam waist is explained by means of figure 3.3. The pulse duration is derived from the zinc selenide (ZnSe) open aperture Z-scans for  $\lambda = 700nm$ . The two-photon absorption coefficient  $\beta$  is taken from the literature [28] and set as  $\beta_{ZnSe} = 5.6 \frac{cm}{GW}$ . The  $\lambda = 1064nm$  open aperture measurements were performed with cadmium selenide (CdSe) as reference sample with  $\beta_{CdSe} = 23.0 \frac{cm}{GW}$ . Other semiconductors and fused silica are used to check the validity of the utilized two-photon absorption coefficients. The closed aperture data is fitted by means of a least square algorithm which is equivalent to the variational ansatz

$$\delta A_{\text{fit}} = \delta \int_{-\infty}^{\infty} |T_{n_2}(z') - \mathcal{T}_{n_2}(z')| dz' \stackrel{!}{=} 0. \quad (3.3)$$

where  $A_{\text{fit}}$  is the area between theoretical transmittance  $T_{n_2}(z')$  and measured transmittance  $\mathcal{T}_{n_2}(z')$ . The integral is calculated numerically with Simpson's rule. The variation is basically done on a trial and error basis. The algorithm first tries zero nonlinearity and increases afterwards  $n_2$  in steps of  $10^{-15} \frac{cm^2}{W}$  until  $A_{\text{fit}}$  grows. Afterwards the nonlinear refractive index is decreased in steps of  $10^{-16} \frac{cm^2}{W}$  until the area between both curves is getting larger again. Finally,  $A_{\text{fit}}$  is minimized by increasing  $n_2$  in steps of  $10^{-17} \frac{cm^2}{W}$  which is set as the precision of the fit algorithm. In order to emphasize peak and valley of  $\mathcal{T}_{n_2}(z')$ , where less points are taken than at the wings, the data is weighted on a linear scale from one to five. The further a data point is away from unity transmittance the higher its weighting factor. For example, three data points are measured, the first at  $\mathcal{T}_1 = 1.00$ , the second at  $\mathcal{T}_2 = 1.10$  and the third at  $\mathcal{T}_3 = 1.03$ . The weights are subsequently  $w_1 = 1$ ,  $w_2 = 5$  and  $w_3 = 2.2$ . Only 50 points in the vicinity of  $z = 0$  are used to fit the data. The other points at the far wings are mainly considered during the normalization routine. Figure 3.4 illustrates the fitting routine which is applied to all of the averaged normalized Z-scan data that was measured. The results for the same pulse duration but different energies are averaged to one value. The average takes into account the standard deviation obtained from the least square fits by weighting with its

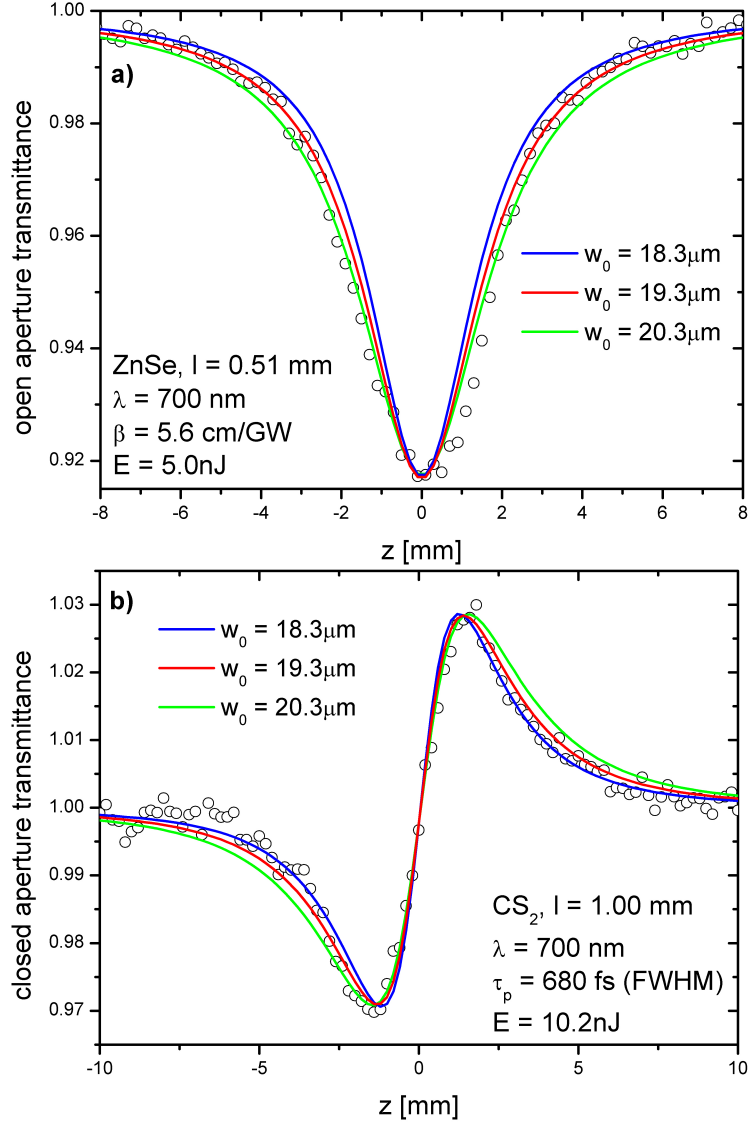


Figure 3.3: Determination of the beam waist by means of the open and the closed aperture Z-scan analysis.

The open aperture signal a) is well fitted at the wings by  $w_0 = 19.3\mu\text{m}$ . The  $w_0 = 20.3\mu\text{m}$  curve fits the peak better than the red curve,  $w_0 = 18.3\mu\text{m}$  is clearly too small. On the other hand, the blue curve fits the wings of the closed aperture signal b) well although the peak-valley distance is too small. The large beam waist does not look appropriate for the closed aperture data and thus  $w_0 = 19.3\mu\text{m}$  is chosen as the beam waist for further analysis. Pulse duration and nonlinear refractive index are adjusted to the signal extrema. Further measurements at different energies are evaluated to determine the beam waist.

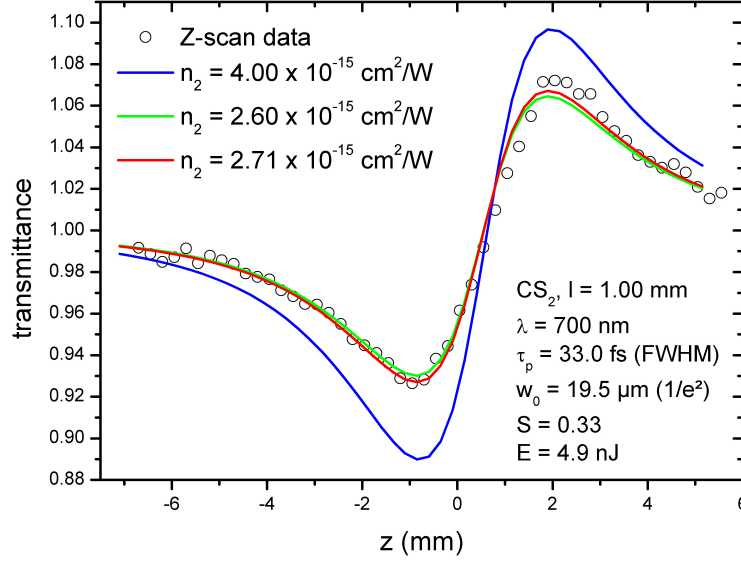


Figure 3.4: Illustration of the  $n_2$  least square fit routine for a prenormalized curve.

The best fit with a precision of  $10^{-17} \frac{\text{cm}^2}{\text{W}}$  is obtained for  $n_2 = 3 \cdot 10^{-15} \frac{\text{cm}^2}{\text{W}}$ . Consequently, the routine starts decreasing  $n_2$  in steps of  $10^{-16} \frac{\text{cm}^2}{\text{W}}$  at  $n_2 = 4 \cdot 10^{-15} \frac{\text{cm}^2}{\text{W}}$  until it overshoots the best fit  $n_2 = 2.7 \cdot 10^{-15} \frac{\text{cm}^2}{\text{W}}$ . Finally, the refractive index is increased in steps of  $10^{-17} \frac{\text{cm}^2}{\text{W}}$  until the best fit is obtained.

inverse.

### 3.2 Effective $n_2$ for Gaussian Laser Pulses at $\lambda = 700\text{nm}$

As indicated in section 1.1, the nonlinear refraction of light in  $\text{CS}_2$  is influenced by nuclear motions and thus changes in time. Owing to the subsequent importance of the shape of the short laser pulses, the term "effective  $n_2$ " is used. The equation (1.15), i.e.  $\Delta n(t) = n_2 I(t)$ , is not applicable for the case of a time dependent nonlinear refractive index. Instead, the change of the refractive index must be expressed as

$$\Delta n(t) = n_{2,eff} \cdot f(t) \quad (3.4)$$

where the function  $f(t)$  contains the time dependency of the material's response function *and* the laser pulse. Nonetheless, an effective  $n_{2,eff}$  can be derived that appears to satisfy

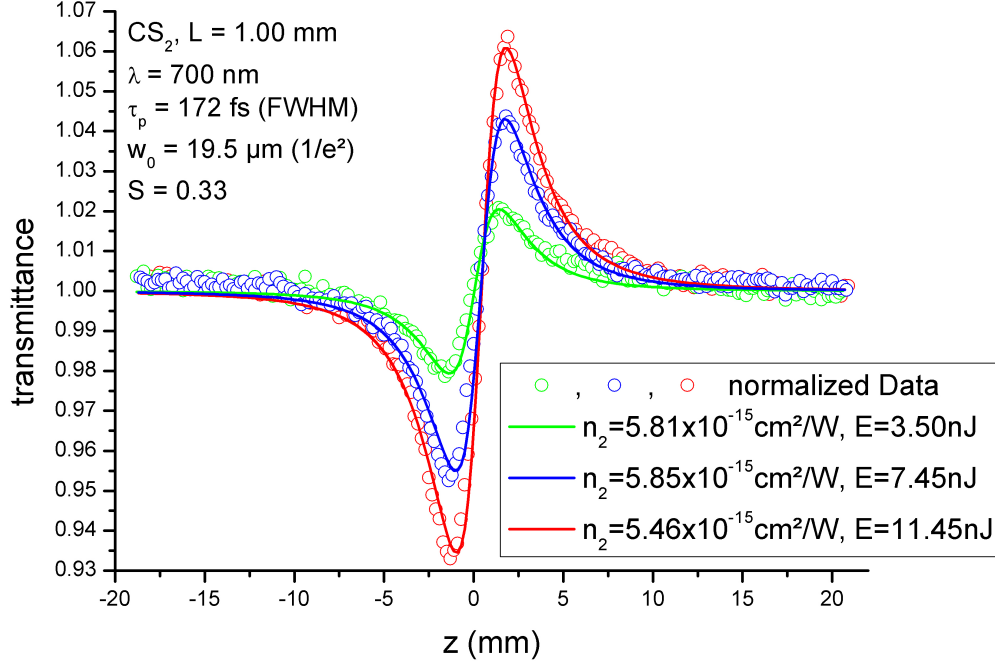


Figure 3.5: Example for the closed aperture data analysis for light of the wavelength  $\lambda = 700nm$ .

The average effective nonlinear refractive index for the pulse duration  $172fs$  is determined to be  $n_{2,eff} = 5.74 \cdot 10^{-15} \frac{cm^2}{W}$ .

the equation  $\Delta n(t) = n_2 I(t)$ . Since the ultrashort pulses of many laser systems are fairly well described by a Gaussian shape, the effective values are of relevance although they are not pure material properties. The pulse duration dependent  $n_{2,eff}$  are obtained by the procedure described in the previous section. Figure 3.5 shows an example of fitted closed aperture curves for a pulse duration of  $172fs$ . All determined effective nonlinear indexes in the temporal range from  $31fs$  to  $2085fs$  are presented in table 3.1.

### 3.3 Effective $n_2$ for Gaussian Laser Pulses at $\lambda = 1064nm$

Similar effective  $n_2$  measurements were performed at a central pulse wavelength  $\lambda = 1064nm$ . However, only the temporal range from  $70fs$  to  $340fs$  is scanned. Shorter pulses could not be generated because the spectral bandwidth the parametric amplifier provides is smaller than for  $\lambda = 700nm$ . Again, a closed aperture Z-scan example is shown in figure 3.6 and the

Table 3.1: Effective nonlinear refractive indexes for Gaussian shaped laser pulses with central wavelength  $\lambda = 700nm$ .

$\tau_p$ (fs)	$n_{2,eff}$ ( $10^{-15} \frac{cm^2}{W}$ )	$\tau_p$ (fs)	$n_{2,eff}$ ( $10^{-15} \frac{cm^2}{W}$ )
31	2.33	217	6.55
32	2.02	235	6.61
33	2.79	265	6.71
37	2.37	313	8.13
43	2.36	368	8.41
48	2.99	495	9.88
57	2.67	585	9.48
65	2.79	620	10.99
67	2.86	680	10.87
83	3.01	865	12.23
92	3.65	1015	12.69
105	3.89	1163	12.08
119	4.06	1412	13.74
125	4.87	1640	14.72
147	4.74	2085	15.75
172	5.74		

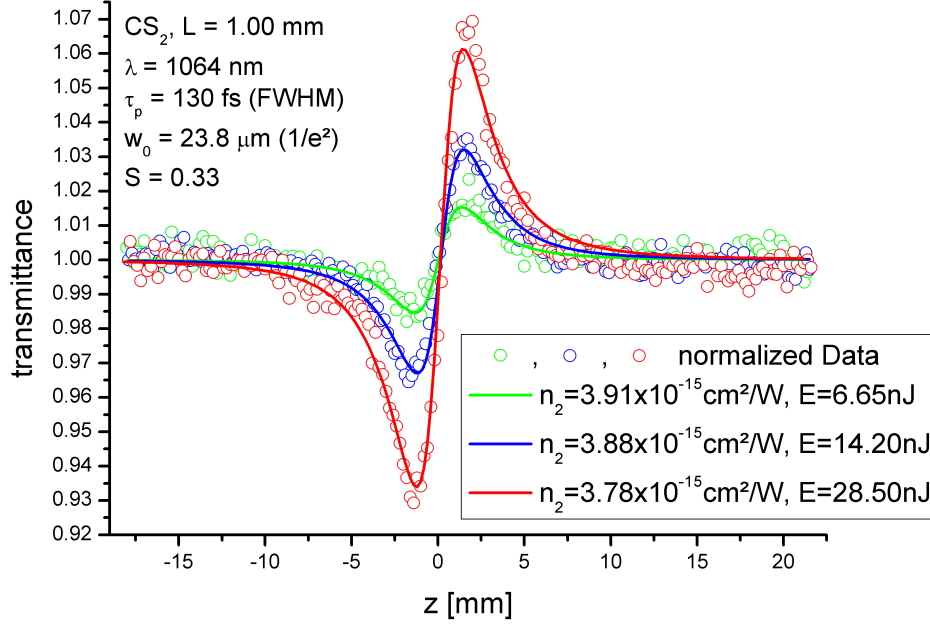


Figure 3.6: Example for the closed aperture data analysis for light of the wavelength  $\lambda = 1064nm$ .

The average effective nonlinear refractive index for the pulse duration  $130fs$  is determined to be  $n_{2,eff} = 3.87 \cdot 10^{-15} \frac{cm^2}{W}$ .

derived values for  $n_{2,eff}$  are shown in table 3.2.

### 3.4 Error Analysis

The measurement uncertainties of the effective values of tables 3.1 and 3.2 shall be analyzed in this section. A straightforward error analysis is not possible in the scope of the Z-scan theory because of the non-analytic character of the expressions (2.13) and (2.16). A phenomenological model is provided that estimates the total error if the measurements. It is investigated by means of the least square fit routine how the determined effective nonlinear refractive index changes upon a small variation of a single parameter, for the uncertainty of  $n_2$  is calculated by

$$u_{n_2}(\lambda, E, \tau_p, w_0) = \left| \frac{\partial n_2}{\partial \lambda} \right| u_\lambda + \left| \frac{\partial n_2}{\partial E} \right| u_E + \left| \frac{\partial n_2}{\partial \tau_p} \right| u_{\tau_p} + \left| \frac{\partial n_2}{\partial w_0} \right| u_{w_0} \quad (3.5)$$

Table 3.2: Effective nonlinear refractive indexes for Gaussian shaped laser pulses with central wavelength  $\lambda = 1064nm$ .

$\tau_p$ (fs)	$n_{2,eff}$ ( $10^{-15} \frac{cm^2}{W}$ )
70	2.44
82	3.24
97	4.19
110	3.87
113	3.64
130	3.87
149	4.66
166	4.86
200	5.34
255	7.10
310	8.05
340	7.93



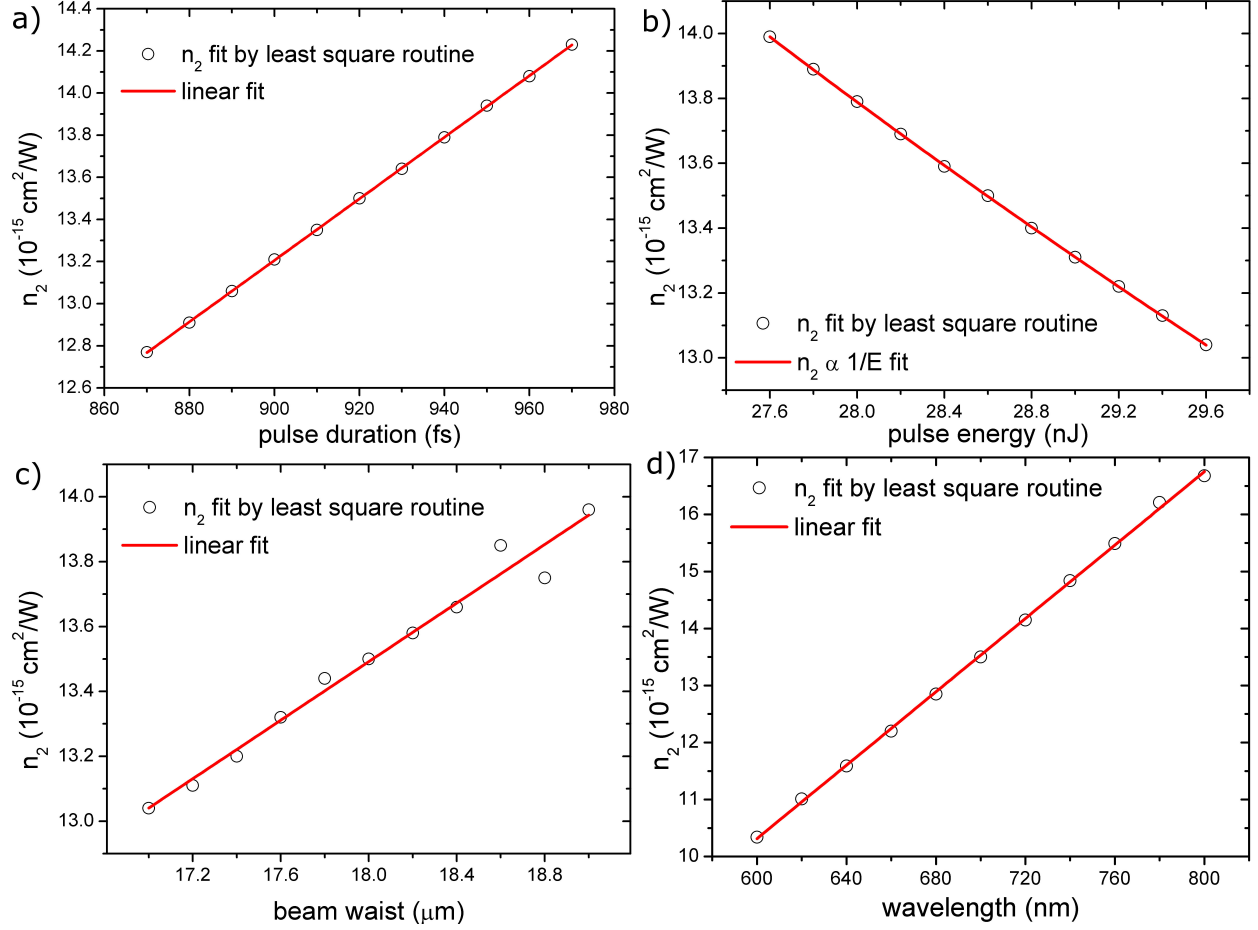


Figure 3.7: Change of  $n_2$  upon the variation of a single parameter.

where prevailing systematic errors are assumed. For this purpose, a theoretical closed aperture curve was created with the parameters  $\tau_p = 920 \text{ fs}$ ,  $E = 28.6 \text{ nJ}$ ,  $w_0 = 18 \mu\text{m}$ ,  $\lambda = 700 \text{ nm}$  and  $n_2 = 13.5 \cdot 10^{-15} \frac{\text{cm}^2}{\text{W}}$ . Figure 3.7 shows that  $n_2$  generally changes fairly linearly upon the variation of  $\lambda$ ,  $\tau_p$ ,  $w_0$  and the inverse of the pulse energy, resp. It is to clarify that the plot of  $n_2$  over  $\tau_p$  does not show the refractive index change in  $\text{CS}_2$  in dependence of the pulse duration, but it exhibits which effective nonlinear refractive index is measured if for instance a pulse duration of  $900 \text{ fs}$  is assumed instead of the real pulse duration  $920 \text{ fs}$ . The oscillations around the lines in the plots c) and to a small amount also d) can be attributed to the change in the transmittance signal shape, which is not present upon the variation of the pulse duration and pulse energy for only beam waist and wavelength change the beam divergence. This is the reason why the determination of  $w_0$  can be separated from the deter-

mination of the other parameters. The central wavelength is measured with a spectrometer and does scarcely change during the experiments. The fairly linear change of  $n_2$  upon small wavelength variations explains partly why only the central wavelength is considered in the Z-scan theory although a wave packet composes the short pulse. The pulse energy is controlled by the reference detector and does therefore certainly contribute by 2% to the measurement uncertainty. Errors caused by the photodetector and the data acquisition have to be added as random errors to the relative energy uncertainty which is about 7%. Wavelength and beam waist can be separately determined and do not change much during the measurements so that they mainly underly a relatively small systematic error of less than 5nm and 4%, resp. The most uncertain parameter is the parameter is the pulse duration. An error of the two-photon absorption coefficient does directly propagate to the uncertainty in the pulse duration since the beam waist is double-checked by the closed aperture scans. Furthermore, the uncertainties of the beam waist and the pulse energy affect the pulse duration determination through an open aperture scan. Consequently, a 10% relative measurement uncertainty of  $\tau_p$  is estimated. Therefore, an external pulse duration measurement, e.g. with an autocorrelator, would help to reduce the total measurement error. Moreover, information about the pulse shape could be revealed. Neither errors resulting from a non-Gaussian pulse shape nor errors resulting from imperfect alignment are taken into account in equation (3.5). To consider these effects as well, a phenomenological additional error of 3% is added to a total relative error which is estimated to be 25% for a single closed aperture Z-scan measurement. The relatively high measurement uncertainty shows up for example in the comparison between the effective  $n_2$  at 32fs and 33fs in table 3.1 as well as at 97fs and 113fs in table 3.2.

At longer pulse durations the spatial resolution of the pulse bandwidth between the prisms was larger than the width of the second prism. That led effectively to manipulations of the pulse spectra and thus also to a change in the temporal shape. If these shape changes affect the determined effective  $n_2$  values severely, is not clear yet and should be subject of future work.

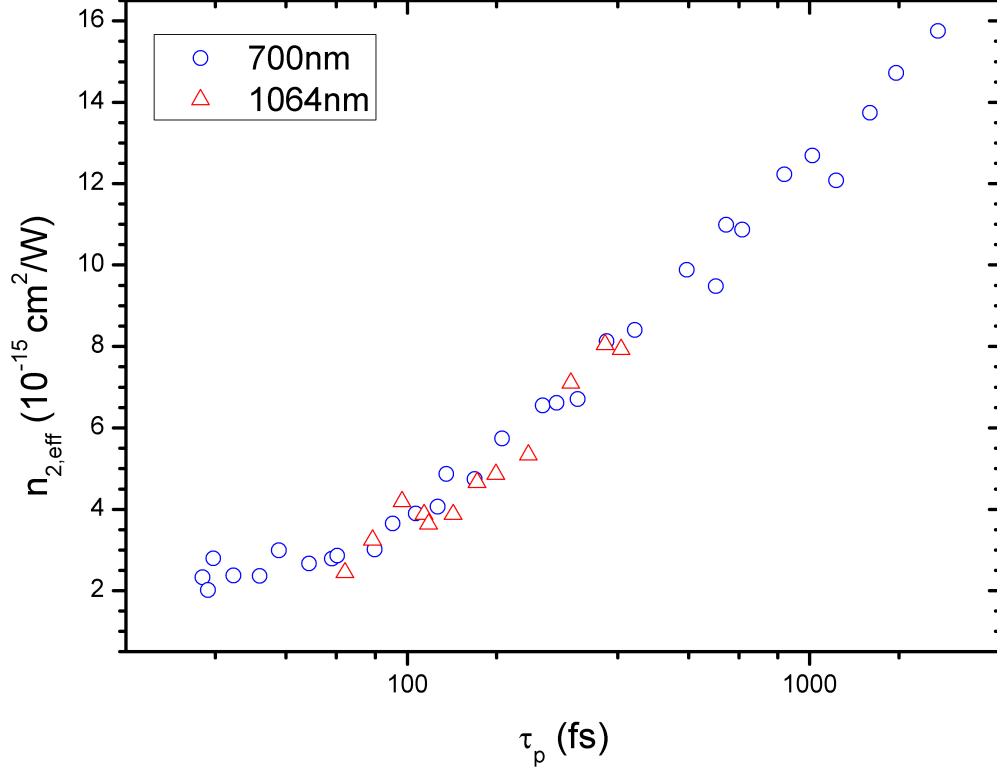


Figure 3.8: Effective nonlinear refractive indexes at  $\lambda = 700nm$  and  $\lambda = 1064nm$ .

### 3.5 Effective $n_2$ Measurements: Conclusions

The measured effective  $n_2$  are plotted in figure 3.8. The values for  $\lambda = 700nm$  and  $\lambda = 1064nm$  do not differ much which indicates that no significant dispersion of  $n_{2,eff}$  is present in this spectral range. The nonlinear refractive index generally grows with increasing pulse duration. The slope of the effective  $n_2$  is relatively small below 100fs in comparison to longer pulse durations. This is the signature of nuclear motions that cannot instantaneously follow the light field but become increasingly significant for  $\tau_p > 100fs$ . The measurement uncertainties are especially significant at very short pulse durations. The measured relative fluctuations of  $n_{2,eff}$  become clearly smaller at longer pulse durations. This curve offers a good reference for short laser pulse applications where the nonlinear refraction in  $CS_2$  is involved.

## 4 PARAMETRIZATION OF THE TIME DEPENDENCE OF $n_2$ IN $\text{CS}_2$

### 4.1 Nuclear Motions in the Neat Liquid Carbon Disulfide

#### 4.1.1 *Molecular Origins of $n_2$*

The previous chapter has shown that not only the bound electronic response of  $\text{CS}_2$  determines the nonlinear refractive index of the material but nuclear motions significantly change its optical properties at pulse durations longer than  $100\text{fs}$ . This section investigates the origins of these nuclear motions in order to describe them mathematically and involve them in the Z-scan analysis.

The Born-Oppenheimer approximation [29] is fundamental for a separated treatment of electronic and nuclear contributions. It states that the inert nuclei cannot follow the rapid motions of the light electrons. Moreover, the electrons react quasi instantaneously to the light field while the nuclei do not notice the fast carrier oscillations but only the electric field envelope.

The nuclear contributions to  $n_2$  can be basically divided into single particle effects and interaction induced effects. The single particle or quasi interaction free effects are due to a collective orientation of the non-symmetric molecules [15, chap. 4] which is energetically favorable. The torque  $\vec{M}$  induced on a dipole  $\vec{p}$  by a homogeneous electric field  $\vec{E}$  is

$$\vec{M} = \vec{p} \times \vec{E}. \quad (4.1)$$

according to classical electromagnetic theory. Consequently, the molecules try to rotate until  $\vec{p}$  and  $\vec{E}$  are parallel which means that no electric field induced force is exerted on the nuclei. If the interaction with other molecules is neglected, the molecules' dipole reads

$$\vec{p} = \tilde{\alpha} \vec{E} \quad (4.2)$$

where

$$\tilde{\alpha} = \begin{pmatrix} \alpha_{\perp} & 0 & 0 \\ 0 & \alpha_{\perp} & 0 \\ 0 & 0 & \alpha_{\parallel} \end{pmatrix} \quad (4.3)$$

is polarizability tensor in the principle axis frame of the molecule. The  $\perp$  sign denotes the polarizability perpendicular to the molecular axis and the  $\parallel$  sign denotes the polarizability along the molecular axis. The cigar shape of the  $\text{CS}_2$  molecules implies that  $\alpha_{\parallel} \gg \alpha_{\perp}$ . Consequently, the randomly oriented particles collectively try to align the molecular axis along the electric field direction. On the other hand, the thermodynamic ensemble is still aiming for a high entropy since the energetically most favorable state is not the state of the lowest electric potential  $U$  but of the lowest free energy  $F$  which is

$$F = U - T \cdot \mathcal{S} \quad (4.4)$$

where  $T$  is the temperature and  $\mathcal{S}$  is the entropy. Therefore, the orientational motion is counteracted by a thermal driven reorientational motion. It can be inferred from equations (4.1), (4.2) and (4.4) that the amount of molecular alignment and thus the refractive index change is dependent on the ensemble temperature and the light intensity.

The electric field in the reference frame of the molecules' principle axes reads

$$\vec{E}(\varphi, \vartheta) = A \begin{pmatrix} -\cos \varphi \sin \vartheta \\ \sin \varphi \sin \vartheta \\ \cos \vartheta \end{pmatrix} \quad (4.5)$$

Again, according to classical electromagnetic theory, the change of the molecules electric potential takes the differential form

$$dU = -\vec{p}d\vec{E} \quad (4.6)$$

which is equivalent to

$$U = -\frac{1}{2} \left( \alpha_{\parallel} A^2 \cos^2 \vartheta + \alpha_{\perp} A^2 \sin^2 \vartheta \right) \quad (4.7)$$

$$= -\frac{A^2}{2} \left( \alpha_{\perp} + (\alpha_{\parallel} - \alpha_{\perp}) \cos^2 \vartheta \right). \quad (4.8)$$

Due to the molecular symmetry, the expression is independent of the angle  $\varphi$ . Comparing this expression with the polarization induced energy density of the electromagnetic field gives

$$\langle U \rangle = -\frac{\bar{E}^2}{2} \langle \alpha \rangle \quad (4.9)$$

where  $\langle \dots \rangle$  denote the ensemble averages and  $\bar{E}$  the time average of the carrier of the electric field. The time average is due to the inert nuclei which cannot follow the fast light oscillations according to the Born-Oppenheimer equation. The polarizability induced refractive index is derived from the Lorentz-Lorenz equation [15, chap. 4]

$$\frac{n^2 - 1}{n^2 + 1} = \frac{N \langle \alpha \rangle}{3\epsilon_0} \quad (4.10)$$

where  $N$  denotes the number density of molecules. The ensemble average takes into account the entropy term of equation (4.4). Assuming a classical Maxwell-Boltzmann distribution, the ensemble averaged polarizability reads

$$\langle \alpha \rangle = \alpha_{\perp} + (\alpha_{\parallel} - \alpha_{\perp}) \langle \cos^2 \vartheta \rangle \quad (4.11)$$

$$= \alpha_{\perp} + (\alpha_{\parallel} - \alpha_{\perp}) \frac{\int_0^{\pi} d\vartheta \sin \vartheta \cos^2 \vartheta e^{-U(\vartheta)/(k_B T)}}{\int_0^{\pi} d\vartheta \sin \vartheta e^{-U(\vartheta)/(k_B T)}} \quad (4.12)$$

$$= \alpha_{\perp} + (\alpha_{\parallel} - \alpha_{\perp}) \frac{\int_{-1}^1 d\xi \xi^2 e^{J\xi^2}}{\int_{-1}^1 d\xi e^{J\xi^2}} \quad (4.13)$$

where

$$J := \frac{\alpha_{\parallel} - \alpha_{\perp}}{2} \cdot \frac{A^2}{k_B T} \quad (4.14)$$

and  $k_B$  denotes the Boltzmann constant. For  $J < 5$ , the number of oriented molecules grows quasi linearly with the intensity of the light field [15, chap. 4]. This value corresponds to an intensity of  $\approx 10^{13} \frac{W}{cm^2}$  at room temperature which is about three orders of magnitude higher than the peak intensities of the performed measurements. Consequently, the ensemble averaged polarizability can be approximated as

$$\langle \alpha \rangle \approx \alpha_{\perp} + (\alpha_{\parallel} - \alpha_{\perp}) \left( \frac{1}{3} + \frac{4J}{45} \right) \quad (4.15)$$

and the nonlinear refractive index reads

$$n_2 = \frac{N}{45n_0^2\epsilon_0^2c} \left( \frac{n_0^2 + 2}{3} \right)^4 \frac{(\alpha_{\parallel} - \alpha_{\perp})^2}{k_B T}. \quad (4.16)$$

#### 4.1.2 Time Dependence of the Nuclear Response

The previous section explains why nuclear motions contribute to the nonlinear refractive index  $n_2$ . The presented theory however does neither involve a time dependence of the

polarizability tensor nor a time dependent electric field. While this theoretical treatment is sufficient for static fields and quasi continuous electromagnetic waves, it has to be extended in the case of ultrashort laser pulses.

A sharp Lorentzian peak in dynamic light scattering spectra of CS<sub>2</sub> [30] indicates that the reorientational motion of the molecules is described by an exponential function. Therefore, the rotational motion can be modeled by a driven damped harmonic oscillator [31]:

$$\mathcal{I} \frac{d^2 \Delta \vartheta}{dt^2} + \xi \frac{d \Delta \vartheta}{dt} + \kappa \cdot \Delta \vartheta = \frac{\alpha_{||} - \alpha_{\perp}}{3} \left( \frac{n_0^2 + 2}{3} \right)^2 \cdot \mathcal{A}(\vec{r}, t) \sin \vartheta \cos \vartheta \quad (4.17)$$

where  $\Delta \vartheta$  is the angular deviation from the molecules equilibrium position  $\vartheta$ ,  $\mathcal{I}$  is the molecule's moment of inertia,  $\xi$  represents the internal friction and  $\kappa$  denotes the elastic force constant of the assumed harmonic potential. The temperature effects are consequently included in the internal friction coefficient. The upper equation rewritten in terms of  $n_2$  reads [31]

$$\frac{\mathcal{I}}{\kappa} \frac{d^2 \Delta n}{dt^2} + \frac{\xi}{\kappa} \frac{d \Delta n}{dt} + \Delta n = n_2^* I(\vec{r}, t) \quad (4.18)$$

where

$$n_2^* = \frac{2N}{15n_0^2 \epsilon_0 c} \left( \frac{n_0^2 + 2}{3} \right)^4 \frac{(\alpha_{||} - \alpha_{\perp})^2}{\kappa} \quad (4.19)$$

While R. Cubeddu *et al.* [31] interpret the underdamped solution of equation (4.18) as a librational motion of the molecules, i.e. a hindered orientation which results in an oscillatory “molecular rocking”, McMorro *et al.* [32] point out that also an overdamped solution of the differential equation can for example be physically interpreted through the quasi free orientational motion which is discussed in the previous chapter. Multiple solutions of the initial differential equation are possible because  $\xi$  and  $\kappa$  are averaged quantities of an initially highly random medium which may be considerably different if the environment of a single



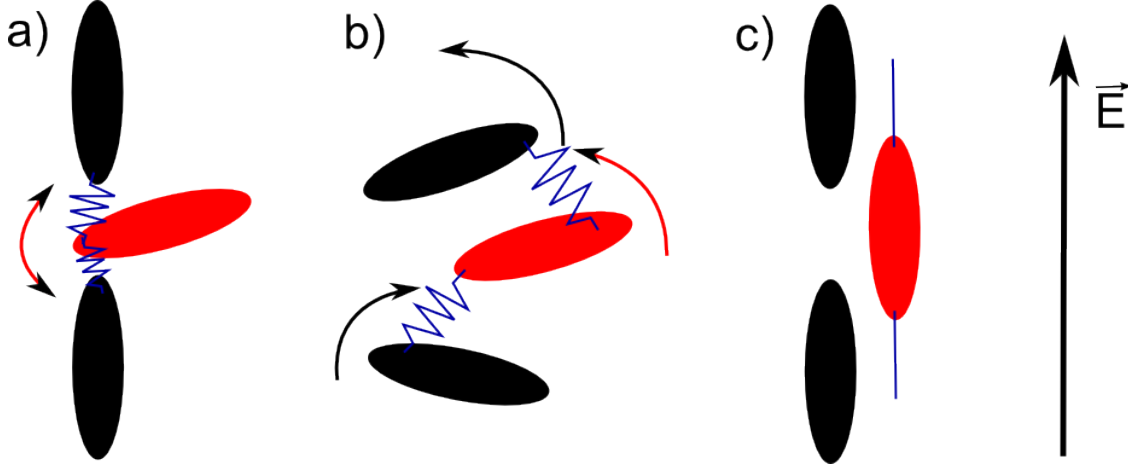


Figure 4.1: Rotational motions contribution to the nonlinear refraction.

In a), the red colored molecule is confined in the potential of two other aligned molecules which do not feel the torque induced by the external electric field. The red colored molecule starts oscillating in the potential of the neighboring molecules,  $\kappa$  is large. In b), the three molecules are mutually fairly aligned and collectively start an orientational motion,  $\kappa$  is smaller than in a). In c), the molecules are perfectly aligned, no molecular motion occurs,  $\kappa$  is zero.

molecule is considered. The force constant  $\kappa$  may be therefore interpreted as indicator of the mutual alignment of molecules along the electric field direction. Consequently,  $\kappa$  decides if a particular molecule changes its orientation (small  $\kappa$ ) or starts to librate (large  $\kappa$ ). Figure 4.1 illustrates three cases of the molecular reaction upon an external light field in the zero-temperature limit. It indicates that  $\kappa$  generally decreases with an increased degree of alignment along the electric field axis. It can be inferred that the quickly occurring librational motion is suppressed by the slower orientational motion of the molecules. McMorow *et al.* [32] estimate the time constant of the librations to be shorter than  $170\text{fs}$  and the time constant of the diffusive reorientational motion to be longer than  $1\text{ps}$  in simple liquids. The fact that the time ranges of both effects are quite distinct suggests to treat them independently [33]. However, a more precise treatment, as employed in molecular dynamics simulations [34], includes a dynamic correlation function  $F(t)$  in the total contribution to the intensity

induced phase change due to rotational motions

$$\Delta\phi(t) \propto (1 + F(t))\Delta\phi^{SP}(t). \quad (4.20)$$

The function  $F(t)$  takes into account the degree of alignment in the medium and  $\Delta\phi_2^{SP}$  is the nonlinear refractive index due to single particle effects.

The fact that nuclear contributions to  $n_2$  were also observed in atomic liquids [35] indicates that not only rotational motions determine the time dependence of  $n_2$ . Since atoms only have translational degrees of freedom, the refractive index change is attributed to a so-called translational anisotropy. The environment of an atom or molecule is altered through light induced dipoles. The molecule is hence not at its energetically favorable location and moves along the induced field gradient. The also called collision induced motion is orthogonal to the rotational motions and can thus be separated from other nuclear contributions to  $n_2$  [34]. Although dynamic light scattering spectra show that the collision induced effects do not exhibit an exact Lorentzian shape, optical Kerr effect studies imply that the temporal description of the motion is well matched by an exponential rise and decay function [12, 33, 36].

## 4.2 Macroscopic Description of the Noninstantaneous Material Response

In chapter 1.3, the polarization is generally introduced as a convolution of the time dependent material response function and the electric fields. In order to obtain the most common description of the nonlinear refractive index, the assumption of an instantaneous response is necessary. The determination of the effective  $n_2$ , presented in chapter 3, is based on this description. Now, equation (1.4) shall be considered again and treated with regard to the

noninstantaneous nuclear response. The expression can be simplified to

$$\mathcal{P}_i^{(3)}(\vec{r}, t) = \frac{3\epsilon_0}{4} \int_0^\infty dt' \mathcal{R}_{ijkl}^{(3)}(t') \mathcal{E}_j(\vec{r}, t) \mathcal{E}_k(\vec{r}, t - t') \mathcal{E}_l^*(\vec{r}, t - t'). \quad (4.21)$$

if the Born-Oppenheimer approximation is valid [37]. The convolution of the field  $\mathcal{E}_j(\vec{r}, t)$  and the material response has not to be taken into account in equation (4.21). The SVEA can be applied again and thus the reduced wave equation has still the form of equation (1.10). Under the assumption of linearly polarized light and after inserting (4.21), the wave equation reads

$$e^{i\omega_0 t} \left( e^{i\phi} \frac{\partial A}{\partial z} + iA e^{i\phi} \frac{\partial \phi}{\partial z} \right) = iA e^{i(\phi + \omega_0 t)} \frac{3k_0}{8n_0} \int_0^\infty dt' \mathcal{R}_{xxxx}^{(3)}(t') A^2(\vec{r}, t - t'). \quad (4.22)$$

By rewriting the complex response function, the intensity induced phase change takes the form

$$\frac{\Delta\phi}{k_0 L} = \sum_{i=1}^m \frac{n_{2,i} \int_0^\infty dt' r_i(t') I(\vec{r}, t - t')}{\int_0^\infty dt' r_i(t')} \quad (4.23)$$

where  $r_i(t')$  denotes the real response function of the  $i^{th}$  contribution to the total nonlinear refraction and  $m$  is the number of independent material responses. The response function acts as a distribution function and is normalized by the denominators of the upper equation. If the pulse duration is much longer than the decay time of the material response, the function  $r(t)$  becomes  $\delta$ -like and the single magnitudes of the contributions  $n_{2,i}$  can be added up to a total quasi time-independent nonlinear refractive index. According to the previous section, there are  $m = 4$  contributions that determine the total material response. However, since the librational motion and the diffusive orientational motion show correlations, a model where  $m = 3$  is also investigated.

The bound electronic response is quasi instantaneous and is thus expressed as

$$\frac{\Delta\phi_e}{k_0L} = \frac{n_{2,e} \int_0^\infty dt' \delta(t') I(\vec{r}, t - t')}{\int_0^\infty dt' \delta(t')} = n_{2,e} I(\vec{r}, t). \quad (4.24)$$

This is consistent with the result (1.15) of chapter 1.3.

According to the overdamped solution of (4.18), the response function can be formulated as

$$r_{RO}(t) = \left(1 - e^{-t/\beta_{RO}}\right) \cdot e^{-t/\tau_{RO}} \quad (4.25)$$

where  $\beta_{RO}$  characterizes the orientational motion which is delayed through the inertia of the molecules and  $\tau_{RO}$  represents the reorientational motion which is temperature driven.

The interaction induced contributions to the nonlinear refractive index, i.e. librations and collision induced translational motions, take place on a similar time scale which makes it difficult to measure them separately. Furthermore, the involved many-body effects complicate the precise mathematical description of these mechanisms. While Kalpouzos *et al.* include both contributions in the analysis of their optical Kerr effect measurements of CS<sub>2</sub> [36], Sato *et al.* and Hattori *et al.* attribute the fast component of their measurements to a single collision-induced process which is supposed to be mainly governed by translational motions [12, 33]. In any case, the response function of one fast component is described like the response function of the diffusive orientation (4.25). However, different time constants  $\beta_{CI}$  and  $\tau_{CI}$  are involved. The response function of the librations is derived from the underdamped solution of the differential equation (4.18) which reads

$$r_{LIB}(t) = e^{-t/\tau_{LIB}} \sin(\omega t) \quad (4.26)$$

where the oscillation frequency would be

$$\omega = \sqrt{\frac{\kappa}{\mathcal{I}} - \frac{\xi^2}{4\mathcal{I}^2}}. \quad (4.27)$$

As discussed in the previous section, the force constant  $\kappa$  may vary drastically due to different environments of the single molecules. Subsequently, multiple oscillation frequencies are present. In order to take this bandwidth into account, Kalpouzos *et al.* propose to include an inhomogeneous spectral broadening term, so that the librational response function reads

$$r_{LIB}(t) = e^{-t/\tau_{LIB}} e^{-\frac{t^2 \Delta\omega^2}{2}} \sin(\omega_0 t) \quad (4.28)$$

where  $\Delta\omega$  represents the spectral bandwidth and  $\omega_0$  is the central libration frequency.

### 4.3 Implementation of the Parametrized Nonlinear Refractive Index in the Z-scan Analysis

It is basically straight forward to implement the previously introduced theory in the Z-scan analysis since the beam can still be propagated as a sum of Gaussian beams. Only equation (2.7) has to be adjusted through replacing it by equation (4.23). Keeping the complexity of the algorithm low is absolutely favorable for a numerical data fitting routine. Subsequently, it is useful to express the response functions analytically.

The normalization term of equation (4.25) takes the form

$$\int_0^\infty dt' r_{RO,CI}(t') = \tau_{RO,CI} \left( 1 - \frac{1}{1 + \tau_{RO,CI}/\beta_{RO,CI}} \right) \quad (4.29)$$

and the convolution of the response function and the irradiance reads

$$\begin{aligned} \int_0^\infty dt' r_{RO,CI}(t') I(\vec{r}, t - t') &= I(\vec{r}) \cdot e^{\frac{-2t^2}{\tau_G^2}} \sqrt{\frac{\pi}{2}} \tau_G \\ &\cdot \left[ e^{\frac{\tau_G^2}{4} \left( \frac{1}{\tau_{RO,CI}} - \frac{4t}{\tau_G^2} \right)^2} \operatorname{erfc} \left\{ \frac{\tau_G}{\sqrt{2} \cdot 4} \left( \frac{1}{\tau_{RO,CI}} - \frac{4t}{\tau_G^2} \right) \right\} \right. \\ &\quad \left. - e^{\frac{\tau_G^2}{4} \left( \frac{1}{\tau_{RO,CI}} + \frac{1}{\beta_{RO,CI}} - \frac{4t}{\tau_G^2} \right)^2} \operatorname{erfc} \left\{ \frac{\tau_G}{\sqrt{2} \cdot 4} \left( \frac{1}{\tau_{RO,CI}} + \frac{1}{\beta_{RO,CI}} - \frac{4t}{\tau_G^2} \right) \right\} \right] \quad (4.30) \end{aligned}$$

where the complementary error function is defined as

$$\operatorname{erfc}(\zeta) := 1 - \frac{2}{\sqrt{\pi}} \sum_{m=0}^{\infty} \frac{(-1)^m \cdot \zeta^{2m+1}}{m!(2m+1)}. \quad (4.31)$$

The argument  $\zeta$  can take any complex value. The librational response function (4.28) can be rewritten as

$$r_{LIB}(t) = \Im \left\{ e^{-t/\tau_{LIB} + i\omega_0 t} e^{-\frac{t^2 \Delta\omega^2}{2}} \right\} \quad (4.32)$$

and consequently, an analytical expression for the normalization factor is

$$\int_0^{\infty} dt' r_{LIB}(t') = \Im \left\{ \sqrt{\frac{\pi}{2\Delta\omega^2}} \exp \left[ \frac{1/\tau_{LIB}^2 - \omega_0^2 - i\frac{2}{\tau_{LIB}\omega_0}}{2\Delta\omega^2} \right] \operatorname{erfc} \left[ \frac{1/\tau - i\omega_0}{\sqrt{2}\Delta\omega} \right] \right\} \quad (4.33)$$

and the expression for the convolution of material response and light intensity reads

$$\begin{aligned} \int_0^{\infty} dt' r_{LIB}(t') I(\vec{r}, t - t') &= I_0(\vec{r}) \\ &\cdot \Im \left\{ \frac{1}{2} \sqrt{\frac{\pi}{\Delta\omega^2/2 + 2/\tau_G^2}} \exp \left[ -2t^2/\tau_G^2 + \frac{(1/\tau_{LIB} - i\omega_0 + 4/\tau_G^2)^2}{4(\Delta\omega^2/2 + 2/\tau_G^2)} \right] \right. \\ &\quad \left. \cdot \operatorname{erfc} \left[ \frac{1/\tau - i\omega_0 - 4t/\tau_G^2}{2\sqrt{\Delta\omega^2/2 + 2/\tau_G^2}} \right] \right\}. \end{aligned} \quad (4.34)$$

Although these expressions look cumbersome, they are of low computational complexity for they can be fully expressed in terms of power series. Further calculation details with regards to the upper expressions are given in [appendix D](#). It was therefore possible to implement fitting routines in order to find the parameters that match the Z-scan measurements best. The algorithm is reducing the area between theoretical and experimental transmittance curve as expressed through equation (3.3). However, the areas of the single Z-scans are added up and their total sum  $A_{fit,tot}$  is minimized. Instead of changing  $n_{2,eff}$ , like in the previous presented routine, the parameters of the response functions are varied to obtain the best

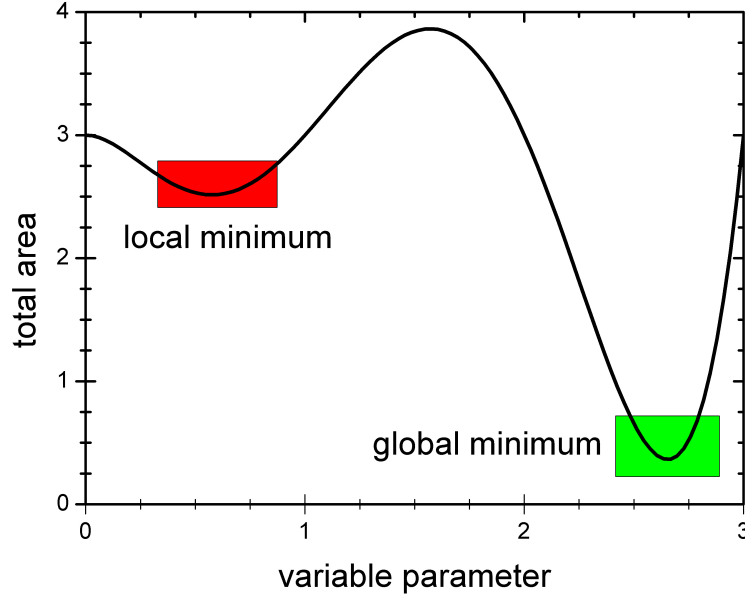


Figure 4.2: Illustration of the fitting algorithm.

If the initial guess of the parameter is one step smaller than  $1.5\overline{7}$ , the routine will stop in the red marked area - the exact spot depends on the chosen step width. Otherwise, the parameter will be stepwise changed until it ends up in the green marked area where the global minimum is. For example: The initial guess for the parameter is 2 and the rather coarse step width is 0.25. The algorithm checks subsequently the values 2, 2.25, 2.5, 2.75, 3 and finally 2.5 again to ensure that 2.75 is the best value.

fit. The algorithm determines  $A_{fit,tot}$  first, changes one parameter in a predetermined step width and checks afterwards if  $A_{fit,tot}$  is smaller after the change. If the total area is reduced the routine changes the next parameter, otherwise the first parameter is increased if it was decreased before or decreased if it was increased before. If neither the first nor the second variation lead to a smaller area, the parameter remains unchanged. If none of the parameters changes anymore, the routine stops and the magnitudes of  $n_2$  as well as the rise and decay times are determined. The algorithm converges in any case within the preset precision but it is not able to find the global minimum of the area  $A_{fit,tot}$  but only the next local minimum. Consequently, the initial guess of the parameters is very important. Figure 4.2 illustrates the fitting routine for a single parameter. The total area can be interpreted as a m-dimensional surface where m is the number of parameters. The higher the dimension of the surface the more likely is a convergence to a local minimum. Consequently, boundary conditions

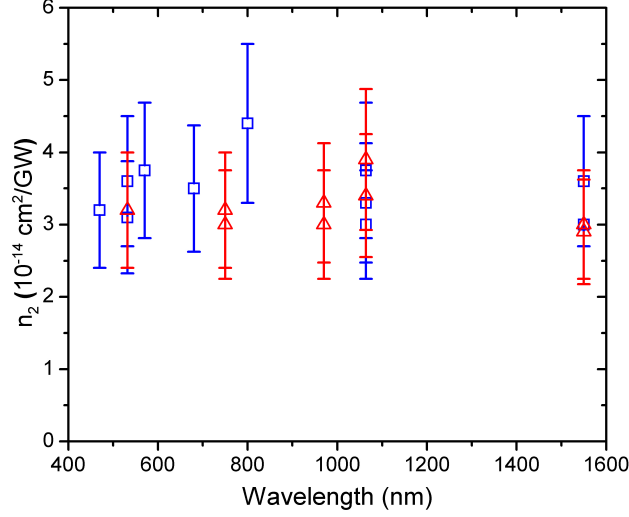


Figure 4.3: Long pulse boundary.

The blue data points show results of Z-scans with CS<sub>2</sub> samples for pulses of  $13ps \leq \tau_p \leq 20ps$  and the red points show results for  $2.5ns \leq \tau_p \leq 16.5ns$ .

were applied to reduce the dimensionality of the surface. The first boundary condition is derived from previous Z-scan measurements that were done in the Nonlinear Optics Group of CREOL. As figure 4.3 implies, the sum of the single contributions  $n_{2,i}$  must be about  $3 \cdot 10^{-14} cm^2/W$ . These results are independently confirmed in a publication of Ganeev *et al.* [11]. As a second boundary, the relaxation time of the reorientational motion is fixed because its value is supposed to be between  $1.3ps$  and  $2.2ps$  according to the literature [12, 38]. A relaxation time of  $\tau_{ro} = 1.7ps$  at the center of this temporal range is assumed. This value is proposed by Hattori *et al.* [33] and close to the value determined by Kalpouzos *et al.* [36] ( $1.61ps$ ) whose theoretical models are similar to the ones which are presented in this thesis. Consequently, the remaining parameters for the three contribution model are  $n_{2,e}$ ,  $n_{2,CI}$ ,  $\beta_{CI}$ ,  $\beta_{RO}$  and  $\tau_{CI}$  as well as  $n_{2,e}$ ,  $n_{2,LIB}$ ,  $n_{2,CI}$ ,  $\beta_{CI}$ ,  $\omega_0$ ,  $\Delta\omega$ ,  $\beta_{RO}$ ,  $\tau_{LIB}$  and  $\tau_{CI}$  for the model including librations separately.



Table 4.1: Fitted parameters for the three and four contribution model.

	three contribution model	four contribution model
$n_{2,e}$	$1.35 \cdot 10^{-15} \frac{cm^2}{W}$	$1.50 \cdot 10^{-15} \frac{cm^2}{W}$
$n_{2,CI}$	$10.0 \cdot 10^{-15} \frac{cm^2}{W}$	$13.0 \cdot 10^{-15} \frac{cm^2}{W}$
$n_{2,RO}^*$	$18.65 \cdot 10^{-15} \frac{cm^2}{W}$	$12.5 \cdot 10^{-15} \frac{cm^2}{W}$
$\beta_{CI}$	$105 fs$	$345 fs$
$\beta_{RO}$	$40 fs$	$350 fs$
$\tau_{CI}$	$160 fs$	$480 fs$
$\tau_{RO}^*$	$1700 fs$	$1700 fs$
$n_{2,LIB}$		$3.0 \cdot 10^{-15} \frac{cm^2}{W}$
$\omega_0$		$1.05 \cdot 10^{13} s^{-1}$
$\Delta\omega$		$3.0 \cdot 10^{12} s^{-1}$
$\tau_{LIB}$		$390 fs$

\* - These parameters were fixed by boundary conditions. The central libration frequency  $\omega_0$  corresponds to a wavelength of  $\lambda_{LIB} = 179 \mu m$  and a spectral line at  $\tilde{\nu} = 56 cm^{-1}$ .

#### 4.4 Fitted Parameters

The step width for  $n_{2,e}$  was chosen to be  $0.2 \cdot 10^{-15} \frac{cm^2}{W}$ , the step widths for  $n_{2,CI}$  and  $n_{2,LIB}$  were  $0.5 \cdot 10^{-15} \frac{cm^2}{W}$  and  $n_{2,RO}$  was determined by the long pulse boundary condition, i.e.  $n_{2,RO} = n_{2,e} + n_{2,CI}$  and  $n_{2,RO} = n_{2,e} + n_{2,CI} + n_{2,LIB}$ , resp. The times and  $1/\Delta\omega_0$  were varied in  $5 fs$  steps. Eventually,  $\Delta\omega$  was varied in steps of  $10^{11} s^{-1}$ . The 81 Z-scans taken at  $\lambda = 700 nm$  were fitted. The results of the three and four contribution model are shown in table 4.1.

The theoretical Z-scan curves of the parameter model are fitted with the algorithm ex-

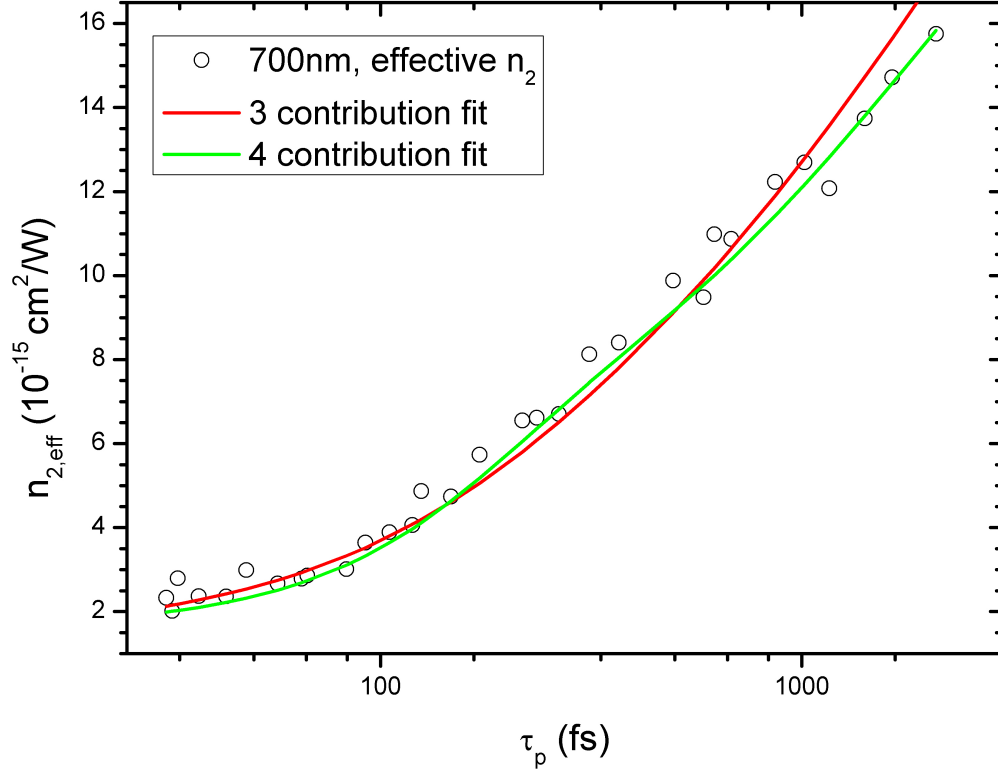


Figure 4.4: Reproduction of the previously determined  $n_{2,eff}$  through the three and four contribution parameter model.

plained in section 3.1 in order to derive a reference curve for the effective  $n_2$ . The reference curves together with the previously determined effective nonlinear indexes are shown in figure 4.4. The magnitudes of the bound electronic response is relatively small in comparison to the short pulse results shown in table 1.2 and the effective values determined in table 3.1. This can be attributed to the slowly arising nuclear contributions which clearly determine the nonlinear response if long pulses are measured. The convolutions of the response functions and the irradiance are shown for three pulse durations in figure 4.5. The functions were designed by the parameters of table 4.1 and have arbitrary units. The plots have in common that the magnitude of the material response grows with the pulse duration. The longer the pulse, the smaller the contribution of  $n_{2,e}$  and the larger the contribution of the diffusive orientation.

It was investigated how sensitive the reference curves in figure 4.4 are with respect to vari-

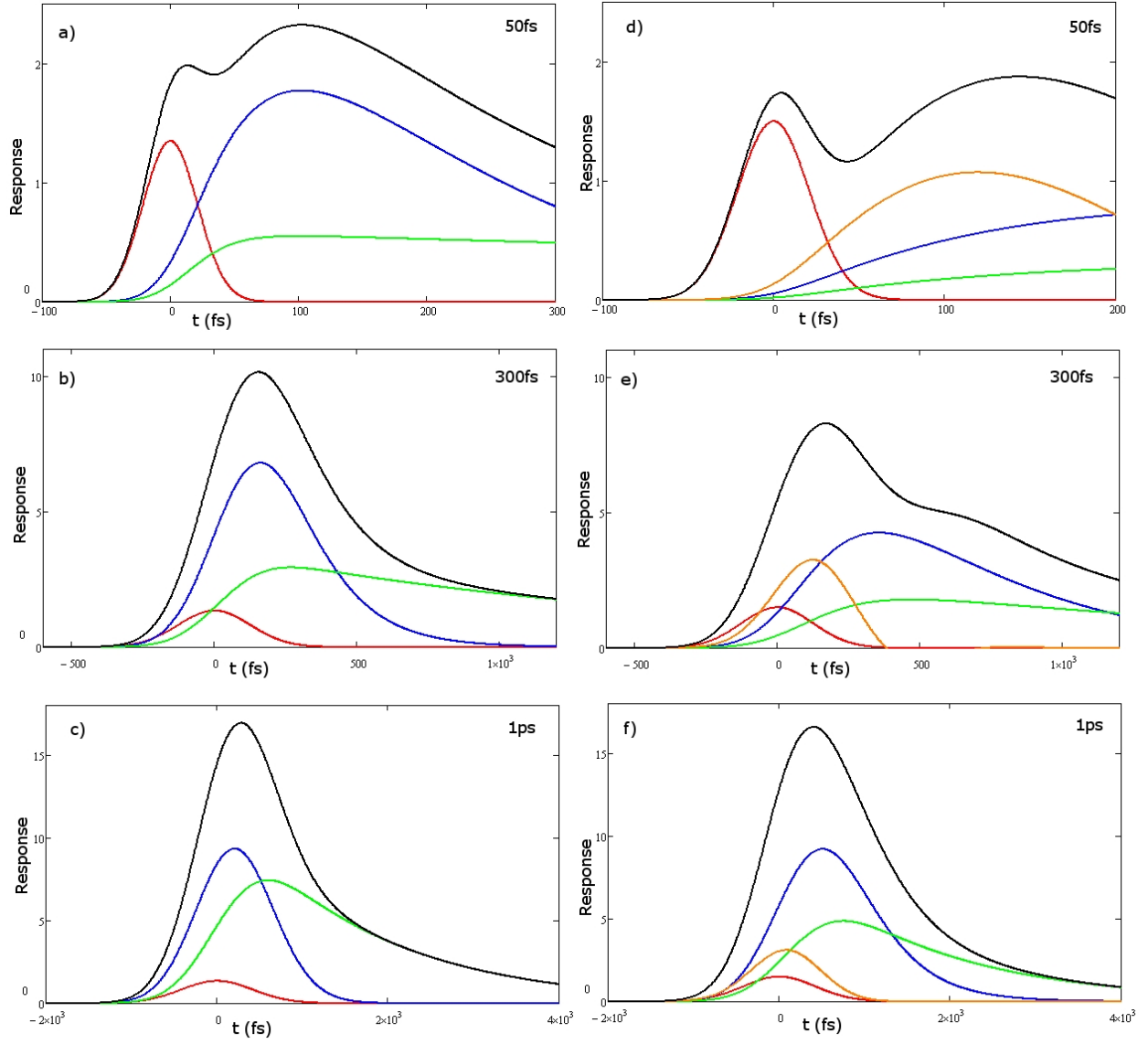


Figure 4.5: Material response plots that are derived from the rise as well as decay times and the magnitudes of the different contributions.

The plots a) to c) show the modeled response for only one ultrafast contribution while plots d) to f) distinguish between librational and collision induced motions. The red curves denote the instantaneous electronic response, the blue curves the ultrafast or collision induced response, the green curves represent diffusive orientation and the orange curves the librational motion. The black line shows the sum of all responses which determines basically  $n_{2,eff}$ . The pulse duration that causes the material response is stated in the upper right corner of the plots.

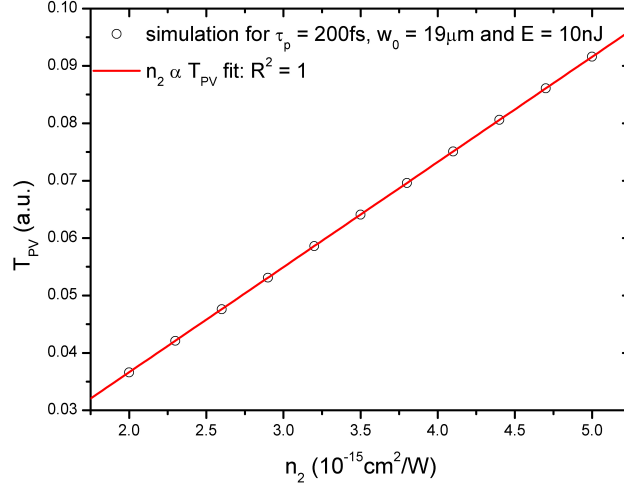


Figure 4.6: Proportionality of the peak-valley difference and the effective nonlinear refractive index

ations of a single parameter. An effective nonlinear refractive index is not involved in the parametrization model but a good measure for  $n_{2,eff}$  is the peak-valley difference in the Z-scan transmission signal  $T_{PV}$ . It turns out that

$$T_{PV} \propto n_{2,eff} \quad (4.35)$$

as indicated in figure 4.6. Therefore, if the single measurement  $n_{2,eff}$  uncertainty is 25%, the  $T_{PV}$  error is also restricted to 25%. Consequently, the peak-valley differences of the effective  $n_2$  fits were determined and utilized by the parameter fitting algorithm. The least square fit parameters were individually varied until one of the resulting theoretical Z-scan curves violated the confidence limits of  $T_{PV}$ . It is problematic however that one of the 81 Z-scans does not exhibit a peak-valley difference interval which corresponds to the  $T_{PV}$  determined by the three contribution parameter fit. In the case of the four contribution model, there are even three curves that do not meet the initial requirement. These Z-scan curves were not considered while varying the single parameters. The occurrence of a small number of measurements which do not lie within the determined confidence interval can be justified since the interval is defined such that it contains a certain percentage of all results

Table 4.2: Allowed variations of the parameters in the three contribution model.

	result	minimal value	maximal value
$n_{2,e}$	$1.35 \cdot 10^{-15} \frac{cm^2}{W}$	$1.20 \cdot 10^{-15} \frac{cm^2}{W}$	$1.70 \cdot 10^{-15} \frac{cm^2}{W}$
$n_{2,CI}$	$10.0 \cdot 10^{-15} \frac{cm^2}{W}$	$7.8 \cdot 10^{-15} \frac{cm^2}{W}$	$12.6 \cdot 10^{-15} \frac{cm^2}{W}$
$n_{2,RO}^*$	$18.65 \cdot 10^{-15} \frac{cm^2}{W}$	$16.05 \cdot 10^{-15} \frac{cm^2}{W}$	$20.85 \cdot 10^{-15} \frac{cm^2}{W}$
$\beta_{CI}$	$105 fs$	$85 fs$	$135 fs$
$\beta_{RO}$	$40 fs$	$20 fs$	$440 fs$
$\tau_{CI}$	$160 fs$	$120 fs$	$200 fs$
$\tau_{RO}^*$	$1700 fs$	-	-

\* - These parameters were fixed by boundary conditions.

(often 95%). The allowed variations of the parameters are listed in table 4.2 for the three contribution model and in table 4.3 for the four contribution model.

The parameters deviate not more than 25% from the best fit value if only one fast nuclear component is considered. The curve is only relatively insensitive to the rise time of the slow nuclear component which could be even one order of magnitude higher than the best fit value. Owing to the higher number of parameters in the four contribution model, the variation of a single parameter has less impact on the reference curve. The uncertainties are consequently higher than in the three contribution model. Especially, changes of  $\tau_{LIB}$  and  $\Delta\omega$  hardly affect the reference curve. The lower limit of the inhomogeneous broadening factor could not be determined due to numerical issues for small  $\Delta\omega$ , the maximal value for  $\tau_{LIB}$  is so far away from the expected range that the algorithm was stopped at times longer than  $6ps$ .

Table 4.3: Allowed variations of the parameters in the four contribution model.

	result	minimal value	maximal value
$n_{2,e}$	$1.50 \cdot 10^{-15} \frac{cm^2}{W}$	$1.30 \cdot 10^{-15} \frac{cm^2}{W}$	$2.10 \cdot 10^{-15} \frac{cm^2}{W}$
$n_{2,CI}$	$13.0 \cdot 10^{-15} \frac{cm^2}{W}$	$9.5 \cdot 10^{-15} \frac{cm^2}{W}$	$20.5 \cdot 10^{-15} \frac{cm^2}{W}$
$n_{2,RO}^*$	$12.5 \cdot 10^{-15} \frac{cm^2}{W}$	$5.0 \cdot 10^{-15} \frac{cm^2}{W}$	$16 \cdot 10^{-15} \frac{cm^2}{W}$
$\beta_{CI}$	$345 fs$	$215 fs$	$470 fs$
$\beta_{RO}$	$350 fs$	$20 fs$	$2600 fs$
$\tau_{CI}$	$480 fs$	$355 fs$	$575 fs$
$\tau_{RO}^*$	$1700 fs$	-	-
$n_{2,LIB}$	$3.0 \cdot 10^{-15} \frac{cm^2}{W}$	$2.0 \cdot 10^{-15} \frac{cm^2}{W}$	$4.5 \cdot 10^{-15} \frac{cm^2}{W}$
$\omega_0$	$1.05 \cdot 10^{13} s^{-1}$	$0.80 \cdot 10^{13} s^{-1}$	$1.54 \cdot 10^{13} s^{-1}$
$\Delta\omega$	$3.0 \cdot 10^{12} s^{-1} < 2.0 \cdot 10^{12} s^{-1}$		$13.9 \cdot 10^{12} s^{-1}$
$\tau_{LIB}$	$390 fs$	$55 fs$	$> 6 ps$

\* - These parameters were fixed by boundary conditions.

## 4.5 Parametrization Model: Conclusions

The three contribution model fits the effective  $n_2$  not as good as the four contribution model but the line in figure 4.4 is still within the measurement uncertainties of the individual data points. The weak spot of the model is clearly the time range where actually two different contributions are present. The red curve in figure 4.4 is systematically below the effective values in the time range between  $200\text{fs}$  and  $800\text{fs}$ . The difference in the response at the time range of the fast nuclear response comes clear in the plots b) and e) of figure 4.5. The four contribution model includes the additional differentiation between two ultrafast responses and fits the effective values therefore very well. However, the rise time parameters  $\beta_{RO}$  and  $\beta_{CI}$  are about  $350\text{fs}$  and therefore considerably longer than expected. Literature values are about  $100\text{fs}$  or less [33, 36]. The libration frequency and the decay time of the collision induced contribution are in the expected range. It is unlikely however, that the collision induced magnitude of  $n_2$  is larger than the orientational diffusion magnitude [32, 12, 33] since the anisotropy of the polarizability tensor is expected to be the main origin of the relatively high nonlinear refractive index of  $\text{CS}_2$ . Furthermore, the parameters errors are clearly higher than for the three contribution model and some of the used parameters do not even influence the theoretical curves severely. It can be concluded that the four contribution model fits the data well, but does only partly quantitatively represent the physical origins of the nonlinearities. The major issue of the model can be attributed the ignorance of equation (4.20). The four contributions may be separable in the case of pump-probe measurements, where a short, intense pump pulse triggers the molecular motions but for a single beam measurement it seems necessary to include the correlation between librations and diffusive orientation. The time-resolved pump-probe measurement basically sees only the the responses of the plots a) or d) of figure 4.5 (depending on the pump pulse duration). The probe scans the material response at a later time. In a single beam measurement, all of the presented material functions of the plots of figure 4.5 are accessible, however the pump is always also

the pump. Apparently, the degree of alignment in the sample changes in a sufficient amount to quench the librations when a long pulse excites the material. This does not change the analysis in the case of plot d) in figure 4.5 since the slow nuclear contribution is still very small. The applied analysis however drives the librations continuously also in the cases e) and f) of figure 4.5. Only the orthogonal, translational fast component can be continuously driven while the trailing edge of the librational component must be steepened in the plots e) and f). In the case of quenched librational motions, the other nuclear components would have to take over the early  $n_2$  components which might result in faster rise times. To interpret the results of the model with two fast contributions more accurately, the numbers of variable parameters would have to be reduced through additional boundary conditions since the errors of the single parameters are quite large. It was however not possible to find well founded conditions for that purpose.

The three contribution model is physically rather reasonable. The times where the librations are expected to launch are covered by an early and wide-spread reorientational contribution and a steep edge ultrafast response. The fast nuclear contribution has a very short time span. It is mainly very strong when librations and translational contributions ought to be present. At later times the diffusive reorientation is mainly contributing to the total material response. Although the three contribution model distributes the librational contribution to the remaining ultrafast and the slow nuclear motions, it is physically reasonable and reproduces the previously determined effective  $n_2$  values well. Only the rise time of the slow nuclear contribution is quite uncertain while the errors of the other parameters do not question their physical interpretation. Therefore the three contribution model is applied in later chapters of this thesis.



## 5 POLARIZATION DEPENDENCE OF THE NONLINEAR REFRACTIVE INDEX

### 5.1 Tensor Nature of the Material Response Function

So far, the presented theory is based on the assumption that the light field that illuminates the sample is linearly polarized. The third order material response function is however a fourth-rank tensor and thus the magnitude of nonlinear refraction exhibits a strong dependence on the light polarization. It is to point out that the rise and the decay times presented in the previous chapter are derived independently of the external light field. Therefore, they should be also independent of the light polarization.

Due to the optical isotropy of CS<sub>2</sub> the tensor  $\mathcal{R}_{ijkl}^{(3)}$  can be reduced to four elements [15, chap. 4] which are  $\mathcal{R}_{1111}^{(3)}$ ,  $\mathcal{R}_{1122}^{(3)}$ ,  $\mathcal{R}_{1212}^{(3)}$  and  $\mathcal{R}_{1221}^{(3)}$  where  $1, 2 = x, y, z$ . The use of  $1, 2, 3$  instead of  $i, j, k$  denotes that the indexes must be different. The material does not exhibit any preferred direction and thus  $\mathcal{R}_{iijj}^{(3)} \stackrel{!}{=} \mathcal{R}_{kkll}^{(3)}$  for all  $i, j, k, l = x, y, z$ . The terms with odd numbers of indexes must vanish. Bound electrons, for example, follow the electric field vector quasi instantaneously. The electrons choose the way where they have to work least. Since the instantaneous work is  $dW = \vec{F} d\vec{s}$  and the force  $\vec{F}$  depends only on the distance to the nuclei but not on any angle, the electrons minimize their way and follow the electric field exactly along its direction of oscillation. Similar arguments hold for input fields of the form  $\mathcal{E}_1^{(*)} \mathcal{E}_2^{(*)} \mathcal{E}_2^{(*)}$  and their permutations as well as for  $\mathcal{E}_1^{(*)} \mathcal{E}_2^{(*)} \mathcal{E}_3^{(*)}$ . Moreover, in the case of  $\mathcal{E}_2^{(*)} \mathcal{E}_2^{(*)} \mathcal{E}_1^{(*)}$ ,  $\mathcal{E}_2^{(*)} \mathcal{E}_1^{(*)} \mathcal{E}_2^{(*)}$  and  $\mathcal{E}_1^{(*)} \mathcal{E}_2^{(*)} \mathcal{E}_2^{(*)}$ , the electrons are formally allowed to respond only

in the direction of the field in direction 1 while they are allowed to respond in the direction of each of the three electric fields in the case of  $\mathcal{E}_1^{(*)}\mathcal{E}_1^{(*)}\mathcal{E}_1^{(*)}$ . Again, since there is no preferred direction, it can be concluded that

$$\mathcal{R}_{1111}^{(3)} = \mathcal{R}_{1122}^{(3)} + \mathcal{R}_{1212}^{(3)} + \mathcal{R}_{1221}^{(3)}. \quad (5.1)$$

Eventually, only three independent tensor components are remaining for any isotropic material. Another component can be eliminated if only the case of nonlinear refraction is considered, i.e. if the polarization frequency is equal to the oscillation frequency of the external electric field. The principle of the so-called intrinsic permutation symmetry states that the response time of a material does not depend on the polarization of the external light field and thus

$$\mathcal{R}_{1212}^{(3)}\mathcal{E}_2\mathcal{E}_1\mathcal{E}_2^* = \mathcal{R}_{1122}^{(3)}\mathcal{E}_1\mathcal{E}_2\mathcal{E}_2^*. \quad (5.2)$$

Consequently,  $\mathcal{R}_{1212}^{(3)}$  and  $\mathcal{R}_{1122}^{(3)}$  are equal. It is to note that the complex conjugated field remains the last factor and cannot be permuted with the other fields. If the c.c. field was set to be the first or second factor, the two real fields could be permuted each time but two tensor components would remain independent in each of the three cases. Subsequently, equation (1.4) can be specified to

$$\begin{aligned} \mathcal{P}_1^{(3)}(\vec{r}, t) = \frac{3\epsilon_0}{4} \left\{ 2 \int_0^\infty dt' \mathcal{R}_{1122}^{(3)}(t') \mathcal{E}_1(\vec{r}, t - t') \mathcal{E}_2(\vec{r}, t - t') \mathcal{E}_2^*(\vec{r}, t - t') \right. \\ \left. + \int_0^\infty dt' \mathcal{R}_{1221}^{(3)}(t') \mathcal{E}_2(\vec{r}, t - t') \mathcal{E}_2(\vec{r}, t - t') \mathcal{E}_1^*(\vec{r}, t - t') \right\} \quad (5.3) \end{aligned}$$

The ratio of the two remaining parameters depends on the origin of the nonlinear effect.

### 5.1.1 Bound Electronic Contribution

The bound electronic response is classically described as an oscillation of electrons in an atomic or molecular potential. The Newtonian equation of motion for an isotropic material reads

$$\vec{F}(\vec{r}, t) = m_e \ddot{\vec{r}}(t) = -e\vec{E}(\vec{r}, t) - 2\Gamma\dot{\vec{r}} - \sum_{i=0}^{\infty} a_i \vec{r}^{2i+1} \quad (5.4)$$

where  $m_e$  is the electron mass,  $-e$  the electron charge,  $\Gamma$  the damping constant and  $a_i$  are force constants. The dots above  $\vec{r}$  denote the first and second time derivative, resp. The centro-symmetry of the potential allows only odd powers of  $\vec{r}$ . If the driving field  $\vec{E}(\vec{r}, t)$  is small, only the harmonic force constant  $a_0$  is relevant. The third order response however, is determined by the  $\vec{r}^3$  term. Owing to the relatively small  $a_1$ , the cubic term can be treated as a perturbation of the harmonic oscillation. For this purpose, a phenomenological parameter  $\mu$  is introduced which turns on ( $\mu = 1$ ) and off ( $\mu = 0$ ) the external electric field. Consequently, the position vector  $\vec{r}$  can be formally expanded in terms of  $\mu$  which leads to a system of differential equations that must be fulfilled for an arbitrary  $\mu$ . It reads

$$m_e \ddot{\vec{r}}_0(t) + 2\Gamma\dot{\vec{r}}_0 + a_0\vec{r}_0 = -e\vec{E}(\vec{r}, t) \quad (5.5)$$

$$m_e \ddot{\vec{r}}_1(t) + 2\Gamma\dot{\vec{r}}_1 + a_0\vec{r}_1^3 = -a_1\vec{r}_0^3 \quad (5.6)$$

if only  $a_0$  and  $a_1$  are considered. The harmonic differential equation (5.5) is analytically solvable in the steady state limit. The solution of  $\vec{r}_0(t)$  can be plugged in equation (5.6) and subsequently  $\vec{r}_1(t)$  is found. The materials polarization is the density of dipoles  $\vec{p} = -e\vec{r}$ , i.e.

$$\vec{P}(t) = -Ne(\vec{r}_0(t) + \vec{r}_1(t)) \quad (5.7)$$

While the complete math is found in [15, chap. 1], only the relation which is decisive with respect to the measurements shall be pointed out here:

$$\chi_{ijkl}^{(3)} \propto \delta_{ij}\delta_{kl} + \delta_{ik}\delta_{jl} + \delta_{il}\delta_{jk} \quad (5.8)$$

where the Kronecker  $\delta$  is defined as

$$\delta_{ij} := \begin{cases} 1 & \text{if } i = j \\ 0 & \text{otherwise} \end{cases}. \quad (5.9)$$

It can be concluded from relation (5.8) that

$$\chi_{1111}^{(3)} = 3\chi_{1122}^{(3)}. \quad (5.10)$$

If  $\chi_{1111}^{(3)}$  is denoted by  $\chi_{11}^{(3)}$  and  $\chi_{1122}^{(3)}$  as well as  $\chi_{1221}^{(3)}$  by  $\chi_{12}^{(3)}$ , equation (5.3) takes the form

$$\vec{\mathcal{P}}^{(3)}(\vec{r}, t) = \frac{3\epsilon_0}{4} \left\{ 2\chi_{12}^{(3)} |\mathcal{E}(\vec{r}, t)|^2 \vec{\mathcal{E}}(\vec{r}, t) + \chi_{12}^{(3)} \vec{\mathcal{E}}^2(\vec{r}, t) \vec{\mathcal{E}}^*(\vec{r}, t) \right\} \quad (5.11)$$

$$= \frac{3\epsilon_0}{4} e^{i\omega_0 t} \left\{ 2\chi_{12}^{(3)} |A(\vec{r}, t)|^2 \vec{\mathcal{A}}(\vec{r}, t) + \chi_{12}^{(3)} \vec{\mathcal{A}}^2(\vec{r}, t) \vec{\mathcal{A}}^*(\vec{r}, t) \right\} \quad (5.12)$$

where the transformation to the carrier reference frame is applied. The vectors can be decomposed into a left-handed and a right-handed circularly polarized component. The orthonormal unit vectors are denoted by  $\hat{\sigma}_l$  and  $\hat{\sigma}_r$ . These vectors are defined as

$$\hat{\sigma}_l := \frac{\hat{x} + i\hat{y}}{\sqrt{2}} = \hat{\sigma}_r^* \quad (5.13)$$

$$\hat{\sigma}_r := \frac{\hat{x} - i\hat{y}}{\sqrt{2}} = \hat{\sigma}_l^* \quad (5.14)$$

for a wave propagating in  $z$ -direction. The orthonormality can be proven in a straight forward manner:

$$|\hat{\sigma}_r|^2 = |\hat{\sigma}_l|^2 = \hat{\sigma}_r \cdot \hat{\sigma}_l = \frac{1}{2} (\hat{x}^2 + \hat{y}^2) = 1 \quad (5.15)$$

$$\hat{\sigma}_r \cdot \hat{\sigma}_l^* = \hat{\sigma}_l \cdot \hat{\sigma}_r^* = \frac{1}{2} (\hat{x}^2 - \hat{y}^2) = 0. \quad (5.16)$$

Through making use of the introduced unit vectors, equation (5.12) reads

$$\begin{aligned} \mathcal{P}_l^{(3)}(\vec{r}, t) \hat{\sigma}_l + \mathcal{P}_r^{(3)}(\vec{r}, t) \hat{\sigma}_r &= \frac{3}{8} \epsilon_0 \left\{ 2\chi_{12}^{(3)} \left( |A_l(\vec{r}, t)|^2 + |A_r(\vec{r}, t)|^2 \right) (\mathcal{A}_l(\vec{r}, t) \hat{\sigma}_l + \mathcal{A}_r(\vec{r}, t) \hat{\sigma}_r) \right. \\ &\quad \left. + 2\chi_{12}^{(3)} (A_l(\vec{r}, t) A_r(\vec{r}, t)) (\mathcal{A}_l^*(\vec{r}, t) \hat{\sigma}_r + \mathcal{A}_r^*(\vec{r}, t) \hat{\sigma}_l) \right\} \end{aligned} \quad (5.17)$$

where the envelope of the electric field is written as

$$\vec{\mathcal{A}}(\vec{r}, t) = \mathcal{A}_l(\vec{r}, t) \hat{\sigma}_l + \mathcal{A}_r(\vec{r}, t) \hat{\sigma}_r. \quad (5.18)$$

The polarization for a circularly polarized electric field of strength  $|A(\vec{r}, t)|$  reads

$$\mathcal{P}_{l/r}^{(3)}(\vec{r}, t) = \frac{3}{4} \epsilon_0 \cdot 2\chi_{12}^{(3)} |A(\vec{r}, t)|^2 \cdot \mathcal{A}_{l/r}(\vec{r}, t) \quad (5.19)$$

$$= \frac{3}{4} \epsilon_0 \cdot \frac{2}{3} \chi_{11}^{(3)} |A(\vec{r}, t)|^2 \cdot \mathcal{A}_{l/r}(\vec{r}, t). \quad (5.20)$$

The equations from (1.8) to (1.16) are independent of the light's polarization and thus the solutions of the reduced wave equation (1.8) for linearly and circularly polarized light predict that

$$\frac{n_{2,e}^{\text{lin}}}{n_{2,e}^{\text{cir}}} = \frac{3}{2}. \quad (5.21)$$

### 5.1.2 Slow Nuclear Contribution

In the case of orientational motions, the polarization is not induced by permanent dipoles but by the polarizability of the molecules as explained in section 4.1.1. Similar to the presented derivation of  $n_2$  for an electrostatic field, the nonlinear refractive index can be derived for electromagnetic fields of an arbitrary polarization. Close *et al.* [39] generalize equation (4.9) to

$$\langle U \rangle = - \sum_{i,j} \frac{\overline{E_i E_j}}{2} \langle \alpha_{i,j} \rangle \quad (5.22)$$

and divide  $\langle \alpha_{i,j} \rangle$  into a sum of the linear  $\alpha$  and nonlinear  $\gamma_{ij}$  polarizability, i.e.

$$\langle \alpha_{i,j} \rangle = \alpha \delta_{i,j} + \gamma_{ij}. \quad (5.23)$$

The nonlinear polarizability reads for CS<sub>2</sub>

$$\gamma_{ij} = \frac{(\alpha_{||} - \alpha_{\perp})^2}{45k_B T} \cdot \sum_{k,l} (3\delta_{ik}\delta_{jl} - \delta_{ij}\delta_{kl}) \overline{E_l E_k}. \quad (5.24)$$

This corresponds to result (4.15) for a linearly polarized static light field where the only element is  $\gamma_{11}^{stat} = \frac{(\alpha_{||} - \alpha_{\perp})^2}{45k_B T} \cdot 2A^2$ . In the case of an electromagnetic linearly polarized field, the time average is however

$$\bar{E}_{lin} = \sqrt{\frac{\omega}{2\pi} \int_0^{2\pi/\omega} dt A^2 \cos^2(\omega t)} = A/\sqrt{2}, \quad (5.25)$$

so that

$$\gamma_{11}^{lin} = \frac{(\alpha_{||} - \alpha_{\perp})^2}{45k_B T} \cdot A^2 \quad (5.26)$$

A circularly polarized field with the same irradiance reads in Cartesian coordinates

$$\bar{E}_{circ} = \frac{A}{\sqrt{2}} (\cos(\omega t)\hat{x} \pm \sin(\omega t)\hat{y}). \quad (5.27)$$

The tensor elements are consequently

$$\gamma_{11}^{circ} = \frac{(\alpha_{\parallel} - \alpha_{\perp})^2}{45k_B T} \cdot \sum_{i,j=1}^2 (3\delta_{1i}\delta_{1j} - \delta_{11}\delta_{ij}) \overline{E_i E_j} = \frac{(\alpha_{\parallel} - \alpha_{\perp})^2}{45k_B T} \cdot \frac{A^2}{4} \quad (5.28)$$

$$\gamma_{12}^{circ} = \frac{(\alpha_{\parallel} - \alpha_{\perp})^2}{45k_B T} \cdot \sum_{i,j=1}^2 (3\delta_{1i}\delta_{2j} - \delta_{12}\delta_{ij}) \overline{E_i E_j} = 0. \quad (5.29)$$

where the indexes 1, 2 are either  $x$  or  $y$ . By comparison to the linearly polarized result (5.26), it can be concluded that

$$\frac{n_{2,RO}^{lin}}{n_{2,RO}^{cir}} = 4. \quad (5.30)$$

## 5.2 Polarization Measurements and Results

The theoretical ratios derived in the previous section are checked experimentally. The three contribution model which seems to fit the material response well within the measurement uncertainties is applied to closed aperture Z-scan data taken with linearly and circularly polarized light. No theoretical evaluation of the fast nuclear response  $n_2$  ratio between linearly and circularly polarized light is provided in this thesis. The value shall only be measured instead. A polarizer and a quarter-wave plate is added to the Z-scan setup as explained in section subsec:complsetup. The measurement were taken in direct succession. After adjusting energy and pulse duration, three closed aperture Z-scan for linearly polarized were done, the  $\lambda/4$ -plate was rotated about  $45^\circ$  and the measurements with circularly polarized light were performed.

Since only the ratio between the nonlinear refractive indexes is of interest in this case, the linear polarization measurements are fitted again, also already included in the data evalu-

Table 5.1: Derived  $n_2$  ratios between linearly and circularly polarized light.

	all magnitudes variable	relative deviation from theory	only $n_{2,CI}$ variable
$n_{2,e}^{lin}/n_{2,e}^{cir}$	1.30	15%	1.5
$n_{2,CI}^{lin}/n_{2,CI}^{cir}$	3		2.69
$n_{2,RO}^{lin}/n_{2,RO}^{cir}$	4.15	4%	4

ation of chapter 3 and 4, allowing the three  $n_2$  magnitudes to adjust as good as possible. This includes that the long pulse boundary condition is lifted. The circular polarization measurements are fitted with the same algorithm. The results shall reveal how well the parameters derived in chapter 4 match the theoretical prediction of the previous section. A second fit routine allows only  $n_{2,CI}$  to vary. The derived parametrized curve is compared to the effective values in order to evaluate a range for  $n_{2,CI}^{lin}/n_{2,CI}^{cir}$ . The ratios for both algorithms are shown in table 5.1. Like in the previous chapter, the theoretical Z-scan curves were fitted with the effective value determining routine and plotted with the  $n_{2,eff}$  values obtained from the experimental data. Figure 5.1 shows the comparison between parameter model and effective values.

### 5.3 Calculation of the Tensor Elements

#### 5.3.1 Electronic Susceptibility Tensor Elements

According to equations (1.16) and (5.20), the independent third-order susceptibility tensor components of the electronic response of  $CS_2$  are calculated through

$$\chi_{11}^{(3)} = \frac{4}{3}n_{2,e}^{lin}n_0^2\epsilon_0c \quad (5.31)$$

$$\chi_{12}^{(3)} = \frac{2}{3}n_{2,e}^{cir}n_0^2\epsilon_0c. \quad (5.32)$$



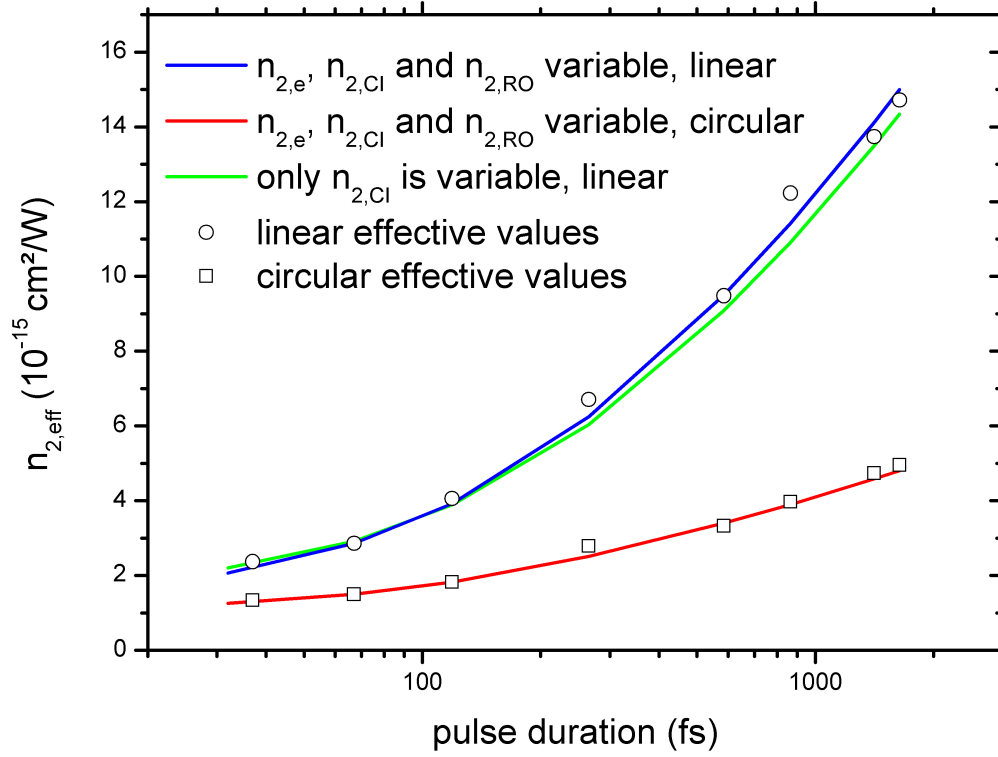


Figure 5.1: Effective values and reference curves of the polarization measurements. The measured times are  $32fs$ ,  $67fs$ ,  $119fs$ ,  $265fs$ ,  $585fs$ ,  $865fs$ ,  $1412fs$  and  $1640fs$ .

By applying equation (5.10), the tensor elements could be also directly determined from the linear measurements. Inserting

$$n_0 = 1.61 \quad [40] \quad (5.33)$$

$$\epsilon_0 = 8.854187817 \cdot 10^{-12} \frac{C}{Vm} \quad [41] \quad (5.34)$$

$$c = 299792458 \frac{m}{s} \quad [41] \quad (5.35)$$

leads to the results

$$\chi_{11}^{(3)} = 1.24 \cdot 10^{-21} \frac{m^2}{V^2} \quad (5.36)$$

$$\chi_{12}^{(3)} = 0.41 \cdot 10^{-21} \frac{m^2}{V^2}. \quad (5.37)$$

Reference values are usually given in electrostatic Gaussian units. The transformation into this unit system is done through [15, appendix C]

$$\chi_{\text{ESU}}^{(3)} = \frac{(3 \cdot 10^4)^2}{4\pi} \chi_{\text{SI}}^{(3)}. \quad (5.38)$$

Therefore, the  $\chi$ s can be rewritten as

$$\chi_{11}^{(3)} = 8.9 \cdot 10^{-14} \text{esu} \quad (5.39)$$

$$\chi_{12}^{(3)} = 3.0 \cdot 10^{-14} \text{esu}. \quad (5.40)$$

It is to note that the theoretical ratio (5.10) was used to obtain these results. The ratio determined by the polarization measurement deviates by 15% from the theory. This deviation can be seen as relative measurement error. Uncertainties due to systematic errors that were present during all measurements should additionally be taken into account. Subsequently,

the nonlinear susceptibilities are expected to be in the range of

$$\chi_{11}^{(3)} = (8.9 \pm 1.8) \cdot 10^{-14} esu \quad (5.41)$$

$$\chi_{12}^{(3)} = (3.0 \pm 0.6) \cdot 10^{-14} esu. \quad (5.42)$$

The values  $\chi_{11}^{(3)} = (6.4 \pm 0.4) \cdot 10^{-14} esu$  and  $\chi_{12}^{(3)} = (2.1 \pm 0.2) \cdot 10^{-14} esu$  published by Yan *et al.* [3] are slightly below (5.41) and (5.42). The publication assumes that all of the nuclear contributions exhibit the nonlinear refractive index ratio (5.30). However, this thesis shows that the ultrafast component exhibits a different relation between  $n_{2,CI}^{\text{lin}}$  and  $n_{2,CI}^{\text{cir}}$ . The derivation of the ratio in 5.1.2 implies the rotational origin of the molecular motion. It is by no means justified that the translational motion exhibits the same ratio which questions the accuracy of the published electronic and nuclear susceptibilities.

### 5.3.2 Nuclear Polarizability Tensor

The origin of the orientational contribution to  $n_2$  is due to the polarizability tensor of the molecules as explained in section 4.1.1. Expressions (5.26) and (5.29) suggest that  $\alpha_{||}$  and  $\alpha_{\perp}$  cannot be determined individually through the  $n_2$  ratio. However, it is possible to calculate the difference of both tensor elements. Combining equations (4.16) and (5.26) leads to the expression

$$\Delta\alpha = \alpha_{||} - \alpha_{\perp} = \sqrt{\frac{90n_0^2\epsilon_0^2c}{N} \left(\frac{3}{n_0^2 + 2}\right)^4 \cdot k_B T \cdot n_{2,RO}}. \quad (5.43)$$

The following values are plugged into the equation

$$n_0 = 1.61 \quad [40] \quad (5.44)$$

$$\epsilon_0 = 8.854187817 \cdot 10^{-12} \frac{C}{Vm} \quad [41] \quad (5.45)$$

$$c = 299792458 \frac{m}{s} \quad [41] \quad (5.46)$$

$$N = \frac{\rho}{M} \cdot N_A = \frac{1.2632}{76.141} \cdot 6.0221417930 \cdot 10^{23} cm^{-3} = 9.973 \cdot \frac{10^{21}}{cm^3} \quad [41] \quad (5.47)$$

$$k_B = 1.380650424 \cdot 10^{-23} J/K \quad [41] \quad (5.48)$$

$$T = 293K \quad (5.49)$$

$$n_{2,RO} = 18.65 \cdot 10^{-15} \frac{cm^2}{W}. \quad (5.50)$$

Consequently, it is found

$$\Delta\alpha = 8.7 \cdot 10^{-40} \cdot \frac{Cm^2}{V} \quad (5.51)$$

$$= 53 \frac{e_0^2 a_0^2}{E_h} \quad (5.52)$$

where

$$e_0 = 1.60217648740 \cdot 10^{-19} C \quad [41] \quad (5.53)$$

$$a_0 = 5.291772085936 \cdot 10^{-11} m \quad [41] \quad (5.54)$$

$$E_h = 4.3597439422 \cdot 10^{-18} J \quad [41]. \quad (5.55)$$

Theoretical and experimental literature values range from  $\Delta\alpha = 56.4 \frac{e_0^2 a_0^2}{E_h}$  to  $\Delta\alpha = 64.8 \frac{e_0^2 a_0^2}{E_h}$  [14] and thus deviate less than 23% percent from the calculated value. This result therefore confirms the magnitude of  $n_{2,RO}$  derived from the three contribution model.

### 5.3.3 Nuclear Susceptibilities

The concept of the third-order susceptibility tensor shall be applied to the  $n_2$  magnitudes of the nuclear contributions since experimental techniques like optical Kerr gating or degenerate four wave mixing may make use the three independent tensor elements of equation (5.1). In order to obtain the ratio (5.30), equation (5.19) have to be reconsidered. In the case of diffusive orientation, this equation must read

$$\mathcal{P}_{l/r}^{(3)}(\vec{r}, t) = \frac{3}{4}\epsilon_0 \cdot \frac{1}{4}\chi_{11}^{(3)}|A(\vec{r}, t)|^2 \cdot \mathcal{A}_{l/r}(\vec{r}, t). \quad (5.56)$$

It can be concluded that

$$\chi_{11}^{(3)} = 8\chi_{1212}^{(3)}. \quad (5.57)$$

Solving equation (5.1) with respect to  $\chi_{1221}^{(3)}$  eventually gives

$$\chi_{11}^{(3)} = \frac{4}{3}\chi_{1221}^{(3)} \quad (5.58)$$

$$\chi_{1221}^{(3)} = 6\chi_{1212}^{(3)}. \quad (5.59)$$

Similarly to section 5.3.1, the magnitudes of the susceptibilities are calculated which are

$$\chi_{1111}^{(3)} = (17.1 \pm 1.6) \cdot 10^{-21} \frac{m^2}{V^2} = (123 \pm 12) \cdot 10^{-14} esu \quad (5.60)$$

$$\chi_{1221}^{(3)} = (2.14 \pm 0.20) \cdot 10^{-21} \frac{m^2}{V^2} = (15.3 \pm 1.4) \cdot 10^{-14} esu \quad (5.61)$$

$$\chi_{1221}^{(3)} = (12.8 \pm 1.2) \cdot 10^{-21} \frac{m^2}{V^2} = (92 \pm 9) \cdot 10^{-14} esu. \quad (5.62)$$

Finally, the tensor elements of the fast nuclear contribution ought to be determined. Starting

from  $n_{2,CI}^{\text{lin}} = 3$ , the relations of the  $\chi$ s read

$$\chi_{11}^{(3)} = 6\chi_{1212}^{(3)} \quad (5.63)$$

$$\chi_{11}^{(3)} = \frac{3}{2}\chi_{1221}^{(3)} \quad (5.64)$$

$$\chi_{1221}^{(3)} = 4\chi_{1212}^{(3)}. \quad (5.65)$$

The magnitudes have a relatively high uncertainty in comparison to the slow nuclear contribution. They are

$$\chi_{1111}^{(3)} = (9.2 \pm 1.5) \cdot 10^{-21} \frac{m^2}{V^2} = (66 \pm 11) \cdot 10^{-14} \text{esu} \quad (5.66)$$

$$\chi_{1221}^{(3)} = (1.53 \pm 0.24) \cdot 10^{-21} \frac{m^2}{V^2} = (11.0 \pm 1.7) \cdot 10^{-14} \text{esu} \quad (5.67)$$

$$\chi_{1221}^{(3)} = (6.1 \pm 1.0) \cdot 10^{-21} \frac{m^2}{V^2} = (44 \pm 7) \cdot 10^{-14} \text{esu}. \quad (5.68)$$

#### 5.4 Polarization Dependence of $n_2$ : Conclusions

The deviation of the  $n_2$  ratios are clearly below the single measurement uncertainties. Especially the ratio for the diffusive reorientation contribution is with only 4% deviation from the theoretical value an excellent result. The linear polarization plots of figure 5.1 show, similarly to the three contribution model results in chapter 4.4, the largest deviation from the effective nonlinear indexes in the time range of the ultrafast contributions. The insufficient differentiation between librations and translational motions has been already mentioned as origin of this effect. Especially the green curve, where  $n_{2,e}$  and  $n_{2,RO}$  were enforced deviates strongly from the data points. However, this curve matches for instance the  $32fs$  data point better than the blue curve, which would correct the 15% deviation of the  $n_{2,e}$  ratio from its theoretical value. At long times, where the slow nuclear contribution is dominant, the blue and the green curve fit the data points almost equally well. The ratio range from 2.7 to 3.0 of the translational motion might be interpreted as a signature of the partly included

libration which should exhibit a  $n_2$  ratio of four since they have the same origin like the reorientational diffusion. On the other hand is the translational motion probably less polarization sensitive than the orientational motion which leads to an effective ratio which is between 1.5 and 4.

In conclusion, the in section 5.1 presented theory was reproduced by the polarization Z-scan measurements. The well fitted effective values which are accompanied by the determined ratios are a strong argument for the applicability of the parametrization model although the willful insufficiently described fast nuclear response region cannot be perfectly matched. Moreover, it is worth to note that Yan *et. al* [3] have recently published a  $n_2$  ratio between 1.7 and 2.2 for  $\tau_p = 125fs$  and  $\lambda = 800nm$ . The ratio determined by means of the fitted curves in figure 5.1 is 2.2 for this particular pulse duration and thus in accordance with the published ellipse rotation measurement result. On the other hand, the magnitudes of the electronic third-order susceptibilities that were proposed in the cited paper could not be confirmed. The observance of a fast nuclear contribution which does not exhibit the  $n_2$  ratio of the slow nuclear contribution must be taken into account in order to determine the tensor elements. Furthermore, the difference between the CS<sub>2</sub> polarizability tensor elements was determined and a result which is quite close to literature values is presented.

## 6 DISPERSION OF THE INSTANTANEOUS ELECTRONIC RESPONSE

### 6.1 The Role of Dispersion in the Electronic Response

The so far presented experiments are mainly focused on the temporal response of CS<sub>2</sub>. Through the method of Fourier transformation from the time domain to the frequency domain, it becomes obvious that a time varying response must have a finite bandwidth. This chapter is mainly concerned about the dispersion of the bound electronic response. As it is shown in figure 3.8, the effective nonlinear index at pulse durations below 100fs changes only slightly while the change of  $n_{2,eff}$  with the pulse duration is much quicker above 100fs. It is basically reasonable to assume that the measured nonlinearity is mainly caused by electrons at these very short times and that the inert molecular motions are rather a perturbation of the measured index. Therefore, the optical parametric amplifier is tuned to a multitude of central wavelengths in order to scan the frequency dependence of  $n_{2,e}$ . The pulses were compressed as much as possible by means of the prism pair. Due to the varying bandwidth, it is however not possible to generate 30fs – 40fs pulses at every central wavelength. Nevertheless, pulse durations below 70fs were achieved in the spectral range from  $\lambda = 411nm$  to 1064nm.

In the previous measurements, a quasi-instantaneous reaction of the bound electrons on the external light field was assumed. This assumption is valid if a flat spectral response of  $n_{2,e}(\omega)$  is present. Mathematically, instantaneous means delta-like and hence the Fourier transfor-



mation would result in a constant. On the other hand, the linear absorption spectrum, figure 1.1, shows absorption bands at about  $200nm$  and  $330nm$ . These linear transitions offer also a higher probability for nonlinear transitions, i.e. two-photon absorption at the doubled wavelengths. In terms of the oscillating electron model of section 5.1.1, a transition is connected to a strong elongation of the electron in its potential. Therefore, higher order force constants become more relevant and enhanced nonlinear refraction is expected.

## 6.2 Dispersion Measurements

Although the Z-scan setup remains as described in chapter 2.2, the data analysis has to change because of the non-negligible two-photon absorption in  $CS_2$  at shorter wavelength. The thin sample approximation, applied in section 2.1.2 to derive the theoretical transmittance, states that the intensity of the light pulse illuminating the sample remains almost unchanged, such that equation (1.12) can be transformed to equation (1.15). In the case of strong multi-photon absorption, this transformation is not possible anymore. Thus the thick sample must be sliced into many thin samples. The pulse which will change its initial shape is also sliced into parts of  $\Delta t$  and  $\Delta r$ . These pulse parts are afterwards propagated through the samples of length  $\Delta z$  in order to calculate the impact of the nonlinear refraction. The Gaussian field decomposition cannot be applied anymore in order to propagate the beam from the sample to the aperture. Instead, the Huygens-Fresnel integral is numerically solved to calculate the closed aperture transmittance. This evaluation of the theoretical signal is clearly of higher complexity than in the thin sample case. Consequently, the fitting routine presented in section 3.1 cannot be applied anymore. The  $n_2$  values were instead fitted by eye. While at longer wavelengths the small absorption effects can be corrected by dividing the closed aperture curve by the open aperture curve, at longer wavelengths this correction is not sufficient anymore. To ensure that no artificial kinks are found in the nonlinear refraction spectrum, all of the measurements were fitted by eye. The detailed mathematical

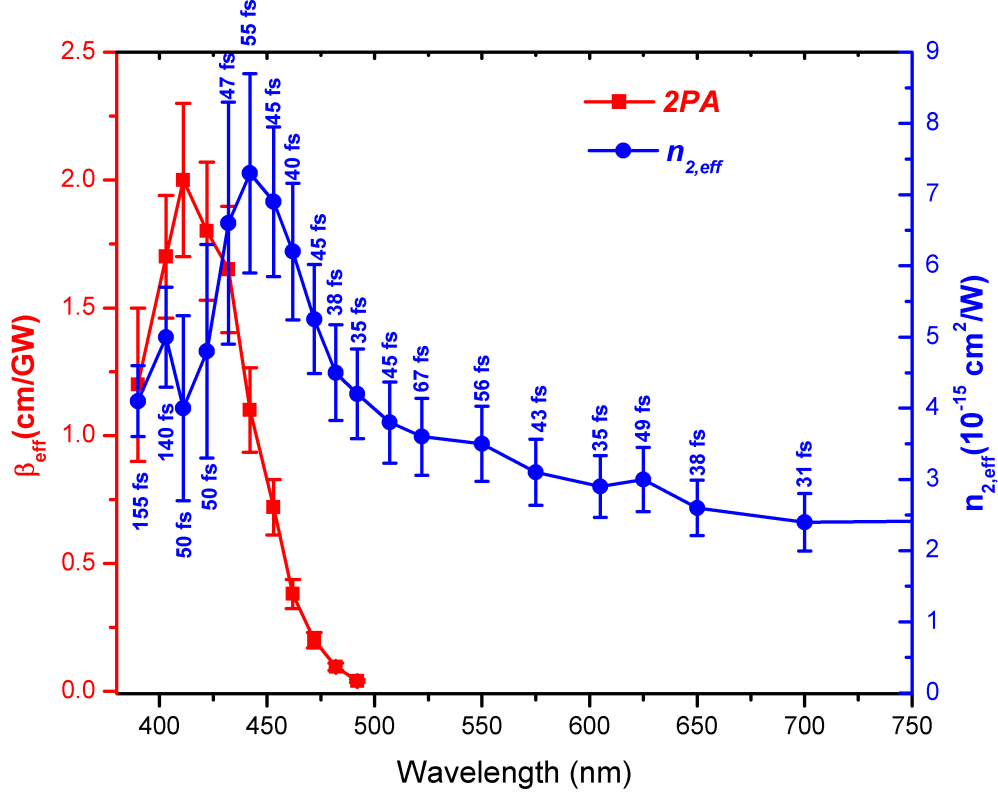


Figure 6.1: Measured effective  $n_2$  and  $\beta$  spectrum for ultrashort pulses

description of the analysis algorithm was published by Said *et al.* [42] and shall not be discussed here. The beam waist and pulse duration were mainly determined by means of open aperture Z-scans with a zinc sulfide (ZnS) sample. The results of the measurements are shown in figure 6.1. Significant two-photon absorption is present at wavelengths smaller than  $450\text{nm}$  which corresponds to the very strong transition around  $200\text{nm}$  that is seen in the linear absorption spectrum in figure 1.1 b). No two-photon absorption is visible in the environment of  $630\text{nm}$  which would correspond to the second absorption band in the linear spectrum. The refractive index increases as predicted towards the two-photon absorption peak. As the transition occurs the anharmonic oscillations are suppressed and the nonlinear refractive index drops to smaller values. At higher wavelengths the spectral response seems to flatten as previously assumed for a quasi-instantaneous reaction of the bound electrons. As indicated by the results of the parameter model, the measured effective refractive indexes at short pulse durations are not fully of electronic origin. Since the nuclear contributions are

however quite small, a linear first order correction should lead to a good estimation of the pure electronic refractive index if the dispersion of the fast nuclear response is small. The effective values from table 3.1 that were measured at pulse durations smaller than  $100fs$  were linearly fitted with the fixed intercept  $n_e = 1.35 \cdot 10^{-15} \frac{cm^2}{W}$ . A pulse duration correction factor of

$$\Delta = 0.0244 \frac{10^{-15} \frac{cm^2}{W}}{fs} \quad (6.1)$$

is determined. The product of the correction factor and the pulse duration subtracted from the measured effective  $n_2$  should reveal a good estimation of  $n_{2,e}(\lambda)$  within the error bars shown in figure 6.1. The dispersion curve in figure 6.2 is quite smooth and has only one small kink at  $525nm$  which is clearly within the previously shown error bars of the measurements. Besides being smoother, the pulse duration corrected curve shows features similar to the uncorrected spectrum. The electronic nonlinear refractive index has its maximum close to the two-photon absorption peak. The index becomes relatively flat at wavelengths which are far away from the 2PA resonance. At the 2PA peak a fast drop of the electronic response is observed.

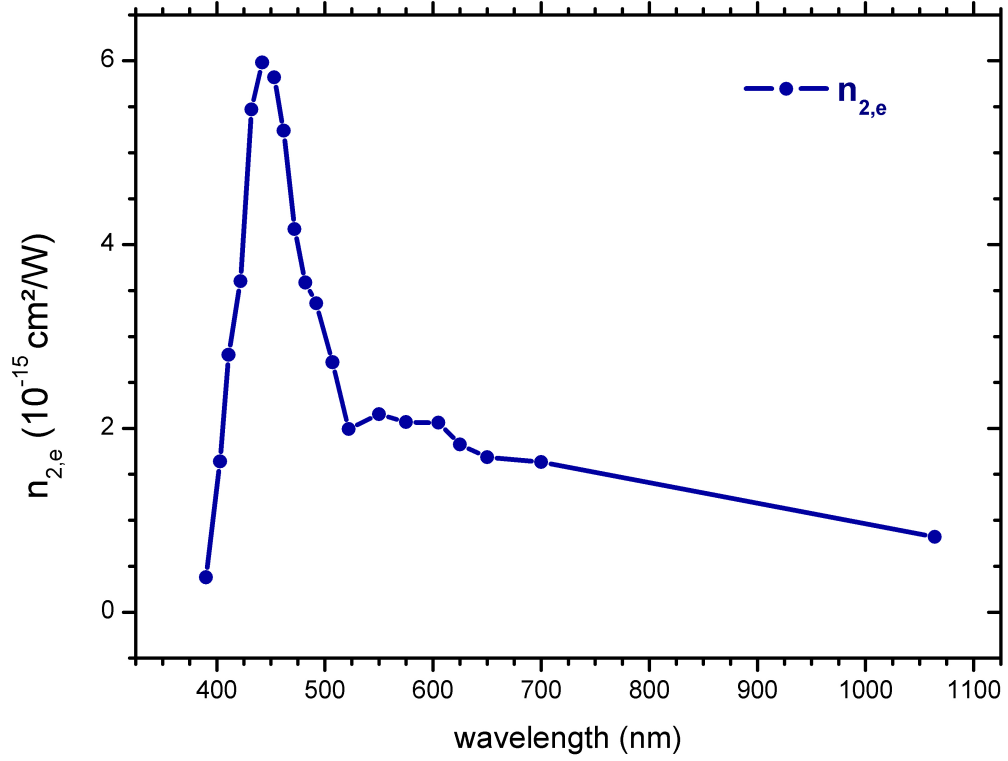


Figure 6.2: Experimentally determined dispersion curve of the electronic contribution to the nonlinear refractive index of  $\text{CS}_2$ .

The points at  $390\text{nm}$  and  $403\text{nm}$  where actually outside the correction range ( $\tau_p < 100$ ) but nonetheless seem to match the electronic dispersion.

## 7 CONCLUSIONS AND PROSPECTS

This thesis reveals the impact of nuclear motions on the nonlinear refractive index of carbon disulfide. A multitude of effective  $n_2$  is determined (cf. table 3.1) for  $\lambda = 700nm$ , that may serve as a reference for nonlinear refraction of  $f$ s-pulses in  $CS_2$ . The effective values do not exhibit a significant amount of dispersion between  $\lambda = 700nm$  and  $\lambda = 1064nm$  as figure 3.8 indicates. Hence, they can probably be utilized over a broader spectral range far from the two-photon absorption peak that is observed at  $\lambda = 410nm$  (cf. figure 6.1). However, more detailed studies are necessary to prove this assumption. Although the dispersion of the bound electronic  $n_2$  was studied (cf. figure 6.2), the dispersion of the nuclear components has not been investigated so far. The dependence of the nuclear  $n_2$  on the central wavelength of the light field is proposed as future work that would rely on the results provided in this thesis.

The effective nonlinear refractive indexes unfortunately underly a quite high measurement uncertainty which is estimated to be about one fourth of the values. It is recommended to decouple the pulse duration measurements and the  $n_2$  measurements by using distinct measurement techniques since these parameter show a similar impact on the closed aperture transmittance. This would clearly reduce systematic errors which are involved in the all-Z-scan measurements. Within the single measurement errors, the effective  $n_2$  curve could be reproduced by a parametrized response function which modeled the temporal behavior of the  $CS_2$  molecules (cf. figure 4.4). A model separating the total material response into a bound electronic, a fast and a slow nuclear contribution is rather preferred than the four

contribution model which divides the fast nuclear response into a librational and collision induced contribution. Firstly, the three contribution model depends on clearly fewer parameters and is thus easier to apply. Furthermore, it represents the physical origins of the nuclear response better than the four contribution model although it adds the contribution of the second real fast nuclear response to the two remaining modeled nuclear responses. The four contribution model must include correlations between the librations and the diffusive reorientation in the case of single beam measurements and must thus be extended to a more involved theory which might limit the practical applicability. The parameters presented in table 4.1 and the equations given in section 4.2 should offer a pulse shape and duration independent description of the nonlinear response of  $\text{CS}_2$  for  $\lambda = 700\text{nm}$  if the pulses are short enough (holds for  $fs$  and  $ps$  range) and the laser repetition rate is small enough ( $kHz$  range) to avoid thermal effects and electrostriction.

The three contribution model has confirmed the theoretical calculations of the ratios of the  $n_2$  magnitudes between linearly and circularly polarized light (cf. table 5.1 and figure 5.1). The ratio for the modeled fast nuclear component is estimated to be between 2.6 and 3.

In order to get more insights of the real magnitude of the electronic and nuclear  $n_2$  components, further experiments that isolate an independent contribution to the total response may be performed. Carbon disulfide in a low pressure vapor phase should for example exhibit the electronic  $n_2$  but not the interaction effects which should allow to determine  $n_{2,e}$  scaled by the molecule volume density more precisely. Diluted  $\text{CS}_2$  solutions have been already experimentally studied ([33], [36]) to observe the magnitude change of the single nuclear contributions to  $n_2$ . Similar experiments could be performed to check the presented theory. Moreover, other measurement techniques could be used to reproduce the determined reference curve in order to eliminate the systematic errors of the presented measurements.

## **APPENDIX A: CAUSALITY**

Many textbooks (e.g. [16]) interpret causality in arguing that no effects which happen at times  $t' > t$  can be observed at time  $t$  and thus express the convolution of the material response function  $\mathcal{R}(t)$  and the light field function  $f(t)$  as

$$\{R * f\}(t) = \int_{-\infty}^t \mathcal{R}(t - t') f(t') dt'$$

The substitution  $\tau = t - t'$  leads to the integrals that are used in the formalism of section 1.3:

$$\begin{aligned} \{R * f\}(t) &= \int_{+\infty}^0 \mathcal{R}(\tau) f(t - \tau) (-d\tau) \\ &= \int_0^{\infty} \mathcal{R}(\tau) f(t - \tau) d\tau. \end{aligned}$$

Hence, the statement that the material cannot respond before it interacts is equivalent to the statement that no response that occurs past the observation time can influence the convolution.



## **APPENDIX B: SLOWLY VARYING WAVE APPROXIMATION**

This section shows how equation (1.8) is transformed into (1.10).

The following abbreviations are used:

$$\begin{aligned}\frac{\partial \mathcal{A}}{\partial z} &\equiv \mathcal{A}' \\ \frac{\partial \mathcal{A}}{\partial t} &\equiv \dot{\mathcal{A}}\end{aligned}$$

Expression (1.6) is inserted into (1.8) and the SVEA is applied:

$$\begin{aligned}& \left[ \left\{ -\underbrace{k^2}_{\frac{n_0^2 \omega_0^2}{c^2}} \mathcal{A}(\vec{r}, t) + 2ik \mathcal{A}'(\vec{r}, t) + \underbrace{\mathcal{A}''(\vec{r}, t)}_{\text{SVEA}} \right\} - \frac{n_0^2}{c^2} \left\{ -\omega_0^2 \mathcal{A}(\vec{r}, t) - 2i\omega_0 \dot{\mathcal{A}}(\vec{r}, t) + \underbrace{\ddot{\mathcal{A}}(\vec{r}, t)}_{\text{SVEA}} \right\} \right] e^{i(kz - \omega_0 t)} \\&= ik \left[ \mathcal{A}'(\vec{r}, t) + \frac{n}{c} \dot{\mathcal{A}}(\vec{r}, t) \right] e^{i(kz - \omega_0 t)} \\&= \frac{1}{\epsilon_0 c^2} \left[ \underbrace{-\omega_0^2 \mathcal{P}_i^{(3)} - i\omega_0 \frac{\partial}{\partial t} (\mathcal{P}_i^{(3)} e^{-i(kz - \omega_0 t)}) + \frac{\partial^2}{\partial t^2} (\mathcal{P}_i^{(3)} e^{-i(kz - \omega_0 t)})}_{\text{SVEA}} \right]\end{aligned}$$

The reference frame is supposed to move with the pulse and thus the following substitutions are made:

$$\begin{aligned}\tau &:= t - \frac{n_0 z}{c} \\ \zeta &:= z \\ \frac{\partial}{\partial t(\tau, \zeta)} &= \frac{\partial \tau}{\partial t} \frac{\partial}{\partial \tau} + \frac{\partial \tau}{\partial \zeta} \frac{\partial}{\partial \zeta} = \frac{\partial}{\partial \tau} \\ \frac{\partial}{\partial z(\tau, \zeta)} &= \frac{\partial \tau}{\partial z} \frac{\partial}{\partial \tau} + \frac{\partial \zeta}{\partial z} \frac{\partial}{\partial \zeta} = -\frac{n}{c} \frac{\partial}{\partial \tau} + \frac{\partial}{\partial \zeta}\end{aligned}$$

Consequently, it is found

$$e^{i\omega_0 \tau} \frac{\partial}{\partial \zeta} \mathcal{A}(\zeta, \tau) = i \frac{\omega^2}{2\epsilon_0 c^2 k} \mathcal{P}_i^{(3)}$$

The variables  $(\zeta, \tau)$  can be relabeled to  $(z, t)$ . The measured quantities are not affected by the transformation.

## **APPENDIX C: POWER TRANSMITTED THROUGH A THIN SAMPLE WITH TWO-PHOTON ABSORPTION**

The laser power behind the absorbing sample is

$$\begin{aligned}
P(d, t) &= 2\pi T_{lin} \int_0^\infty dr r \frac{I(z', r, t)}{1 + \beta L_{eff} I(z', r, t)} \\
&= 2\pi T_{lin} \int_0^\infty dr r \frac{I(z', t) e^{-2\frac{r^2}{w^2(z')}}}{1 + \beta L_{eff} I(z', t) e^{-2\frac{r^2}{w^2(z')}}} \\
&= T_{lin} \cdot \frac{\pi w^2(z')}{2} \int_0^\infty du \frac{I(z', t) e^{-u}}{1 + \beta L_{eff} I(z', t) e^{-u}} \\
&= T_{lin} \cdot \frac{\pi w^2(z')}{2} \int_0^1 du' \frac{I(z', t)}{1 + \beta L_{eff} I(z', t) u'} \\
&= T_{lin} \cdot \frac{\pi w^2(z')}{2\beta L_{eff}} \ln(1 + \beta L_{eff} I(z', t)) \\
&= T_{lin} \cdot \frac{\pi w_0^2 (1 + z'^2/z_0^2)}{2\beta L_{eff}} \ln(1 + \beta L_{eff} I(z', t))
\end{aligned}$$

and the power without 2PA:

$$\begin{aligned}
P_0(d, t) &= 2\pi T_{lin} \int_0^\infty dr r I(r, t) \\
&= T_{lin} \cdot \frac{\pi w_0^2}{2} \cdot I(t).
\end{aligned}$$

The measured energy of a Gaussian shaped pulse is thus

$$\begin{aligned}
E_0(d) &= T_{lin} \cdot \frac{\pi w_0^2}{2} \int_{-\infty}^\infty dt I_0 e^{-2\frac{t^2}{\tau_G}} \\
&= T_{lin} \cdot \frac{\pi^{3/2} \tau_G w_0^2}{2^{3/2}} \cdot I_0.
\end{aligned}$$

## **APPENDIX D: ANALYTIC EXPRESSIONS OF THE NUCLEAR RESPONSE FUNCTIONS**

The integrals of expression (4.23) shall be expressed analytically. For a response function of type (4.25), the normalization term reads

$$\begin{aligned}
\int_0^\infty dt r_{RO,CI}(t) &= \int_0^\infty dt \left(1 - e^{-t/\beta_{RO,CI}}\right) \cdot e^{-t/\tau_{RO,CI}} \\
&= \left[ -\tau_{RO,CI} \cdot e^{-t/\tau_{RO,CI}} + \frac{1}{1/\beta_{RO,CI} + 1/\tau_{RO,CI}} e^{-t \cdot (1/\beta_{RO,CI} + 1/\tau_{RO,CI})} \right]_0^\infty \\
&= \tau_{RO,CI} - \frac{1}{1/\beta_{RO,CI} + 1/\tau_{RO,CI}} \\
&= \tau_{RO,CI} \left( 1 - \frac{1}{1 + \tau_{RO,CI}/\beta_{RO,CI}} \right).
\end{aligned}$$

The convolution of the response function with a Gaussian shaped pulse results in the expression

$$\begin{aligned}
\int_0^\infty dt' r_{RO,CI}(t') I(\vec{r}, t - t') &= \int_0^\infty dt' \left(1 - e^{-t'/\beta_{RO,CI}}\right) \cdot e^{-t'/\tau_{RO,CI}} \cdot I(\vec{r}) \cdot e^{\frac{-2(t-t')^2}{\tau_G^2}} \\
&= I(\vec{r}) \cdot \int_0^\infty dt' \left( e^{-t'/\tau_{RO,CI} + \frac{-2t^2 - 2t'^2 + 4tt'}{\tau_G^2}} - e^{-t'/\beta_{RO,CI} - t'/\tau_{RO,CI} + \frac{-2t^2 - 2t'^2 + 4tt'}{\tau_G^2}} \right).
\end{aligned}$$

It is useful to complete the squares in the exponent, e.g.

$$\begin{aligned}
&-t'/\beta_{RO,CI} - t'/\tau_{RO,CI} + \frac{-2t^2 - 2t'^2 + 4tt'}{\tau_G^2} \\
&= - \left( \frac{\sqrt{2}t'}{\tau_G} - \frac{(1/\beta_{RO,CI} + 1/\tau_{RO,CI})\tau_G}{2 \cdot \sqrt{2}} + \frac{\sqrt{2}t}{\tau_G} \right)^2 \\
&\quad - \frac{2t^2}{\tau_G^2} + \left( \frac{(1/\beta_{RO,CI} + 1/\tau_{RO,CI})\tau_G}{2 \cdot \sqrt{2}} - \frac{\sqrt{2}t}{\tau_G} \right)^2.
\end{aligned}$$

The substitutions

$$\begin{aligned}\xi &= \frac{2}{\tau_G^2} \\ \eta_1 &= (1/\beta_{RO,CI} + 1/\tau_{RO,CI}) - \frac{4t}{\tau_G^2} \\ \eta_2 &= 1/\tau_{RO,CI} - \frac{4t}{\tau_G^2} \\ \zeta &= \frac{2t^2}{\tau_G^2}\end{aligned}$$

simplify the integrals considerably:

$$\begin{aligned}\int_0^\infty dt' r_{RO,CI}(t') I(\vec{r}, t - t') &= I(\vec{r}) e^{-\zeta} \\ &\cdot \left( e^{\frac{\eta_2^2}{4\xi}} \int_0^\infty dt' e^{-\left(\sqrt{\xi}t' - \frac{\eta_2}{2\sqrt{\xi}}\right)^2} - e^{\frac{\eta_1^2}{4\xi}} \int_0^\infty dt' e^{-\left(\sqrt{\xi}t' - \frac{\eta_1}{2\sqrt{\xi}}\right)^2} \right).\end{aligned}$$

By substituting

$$t'' = \sqrt{\xi}t' - \frac{\eta_i}{2\sqrt{\xi}}$$

the expression becomes

$$\begin{aligned}\int_0^\infty dt' r_{RO,CI}(t') I(\vec{r}, t - t') &= I(\vec{r}) e^{-\zeta} \\ &\cdot \left( \frac{e^{\frac{\eta_2^2}{4\xi}}}{\sqrt{\xi}} \int_{\frac{\eta_2}{2\sqrt{\xi}}}^\infty dt'' e^{-t''^2} - \frac{e^{\frac{\eta_1^2}{4\xi}}}{\sqrt{\xi}} \int_{\frac{\eta_1}{2\sqrt{\xi}}}^\infty dt'' e^{-t''^2} \right).\end{aligned}$$

This however can be identified with the complementary error function and thus reads

$$\begin{aligned}\int_0^\infty dt' r_{RO,CI}(t') I(\vec{r}, t - t') &= I(\vec{r}) e^{-\zeta} \sqrt{\frac{\pi}{4\xi}} \\ &\cdot \left( e^{\frac{\eta_2^2}{4\xi}} \operatorname{erfc} \left\{ \frac{\eta_2}{2\sqrt{\xi}} \right\} - e^{\frac{\eta_1^2}{4\xi}} \operatorname{erfc} \left\{ \frac{\eta_1}{2\sqrt{\xi}} \right\} \right).\end{aligned}$$



By reversing the substitutions of  $\xi$ ,  $\eta_1$ ,  $\eta_2$  and  $\zeta$ , the result (4.30) is obtained.

The integrals of the librational response are solved similarly. The expression

$$\int_0^\infty dt r_{LIB}(t) = \Im \left\{ \int_0^\infty dt e^{-t/\tau_{LIB} + i\omega_0 t} e^{-\frac{t^2 \Delta\omega^2}{2}} \right\}$$

can be rewritten to

$$\int_0^\infty dt r_{LIB}(t) = \Im \left\{ \int_0^\infty dt e^{-\left(\frac{t\Delta\omega}{\sqrt{2}} - \frac{i\omega_0 - 1/\tau_{LIB}}{\sqrt{2}\Delta\omega}\right)^2 + \frac{(i\omega_0 - 1/\tau_{LIB})^2}{2\Delta\omega^2}} \right\}.$$

Substituting

$$\begin{aligned} \xi_d &= \frac{2}{\Delta\omega^2} \\ \eta_d &= i\omega_0 - 1/\tau_{LIB}, \end{aligned}$$

gives an integral of the previously solved type and thus the analytic result (4.33). The numerator resembles the denominator but in this case the substitutions

$$\begin{aligned} \xi_n &= \frac{2}{\Delta\omega^2} + \frac{2}{\tau_G^2} \\ \eta_n &= i\omega_0 - 1/\tau_{LIB} + \frac{4t}{\tau_G^2} \\ \zeta &= \frac{2t^2}{\tau_G^2} \end{aligned}$$

have to be made. Subsequently, the result (4.34) follows for the numerator.

## LIST OF REFERENCES

- [1] J. A. Armstrong, N. Bloembergen, J. Ducuing, and P. S. Pershan. Interactions between light waves in a nonlinear dielectric. *Phys. Rev.*, 127(6):1918–1939, Sep 1962.
- [2] P. D. Maker, R. W. Terhune, and C. M. Savage. Intensity-dependent changes in the refractive index of liquids. *Phys. Rev. Lett.*, 12(18):507–509, May 1964.
- [3] X.-Q. Yan, X.-L. Zhang, S. Shi, Z.-B. Liu, and J.-G. Tian. Third-order nonlinear susceptibility tensor elements of CS<sub>2</sub> at femtosecond time scale. *Opt. Express*, 19(6):5559–5564, Mar 2011.
- [4] R. L. Sutherland. *Handbook of Nonlinear Optics*. Marcel Dekker Inc, New York, 2<sup>nd</sup> edition, 2003.
- [5] W. E. Williams, M. J. Soileau, and E. W. Van Stryland. Optical switching and  $n_2$  measurements in CS<sub>2</sub>. *Optics Communications*, 50(4):256 – 260, 1984.
- [6] W. Shensky III, I. Cohanoschi, F. E. Hernandez, E. W. Van Stryland, and D. J. Hagan. Broadband optical limiter using carbon-black suspensions in CS<sub>2</sub>. In *Lasers and Electro-Optics, 2002. CLEO '02. Technical Digest. Summaries of Papers Presented at the*, page 572 vol.1, 2002.
- [7] M. Centurion, Ye Pu, and D. Psaltis. Experimental observation of a phase transition in the filament generation process in kerr media. In *Lasers and Electro-Optics Society, 2004. LEOS 2004. The 17th Annual Meeting of the IEEE*, volume 2, pages 625 – 626 Vol.2, Nov 2004.

- [8] E. Marom, N.A. Vainos, A.A. Friesem, and J.W. Goodman. *Unconventional Optical Elements for Information Storage, Processing and Communications Unconventional Optical Elements for Information Storage, Processing and Communications*. NATO Science Partnership Sub-Series: 3:, Vol. 75. Kluwer Academic Publishers, Dordrecht, 2000.
- [9] M. Falconieri and G. Salvetti. Simultaneous measurement of pure-optical and thermo-optical nonlinearities induced by high-repetition-rate, femtosecond laser pulses: application to  $\text{cs}_2$ . *Applied Physics B: Lasers and Optics*, 69:133–136, 1999. 10.1007/s003400050785.
- [10] S. Couris, M. Renard, O. Faucher, B. Lavorel, R. Chaux, E. Koudoumas, and X. Michaut. An experimental investigation of the nonlinear refractive index ( $n_2$ ) of carbon disulfide and toluene by spectral shearing interferometry and z-scan techniques. *Chemical Physics Letters*, 369(3-4):318 – 324, 2003.
- [11] R.A. Ganeev, A.I. Ryasnyansky, M. Baba, M. Suzuki, N. Ishizawa, M. Turu, S. Sakakibara, and H. Kuroda. Nonlinear refraction in  $\text{CS}_2$ . *Applied Physics B: Lasers and Optics*, 78:433–438, 2004.
- [12] Y. Sato, Morita R., and M. Yamashita. Study on ultrafast dynamic behaviors of different nonlinear refractive index components in  $\text{CS}_2$  using a femtosecond interferometer. *Japanese Journal of Applied Physics*, 36(Part 1, No. 4A):2109–2115, 1997.
- [13] I.P. Nikolakakos, A. Major, J.S. Aitchison, and P.W.E. Smith. Broadband characterization of the nonlinear optical properties of common reference materials. *Selected Topics in Quantum Electronics, IEEE Journal of*, 10(5):1164 – 1170, sept.-oct. 2004.
- [14] George Maroulis. Electric moments, polarizabilities and hyperpolarizabilities for carbon disulfide ( $\text{s=c=s}$ ) from accurate scf calculations. *Chemical Physics Letters*, 199(3-4):250 – 256, 1992.

- [15] R. W. Boyd. *Nonlinear Optics*. Academic Press, Burlington, 3<sup>rd</sup> edition, 2008.
- [16] J.-C. Diels and W. Rudolph. *Ultrashort Laser Pulse Phenomena*. Academic Press, Burlington, 2<sup>nd</sup> edition, 2006.
- [17] M. Sheik-Bahae, Said A. A., and E. W. Van Stryland. High-sensitivity, single-beam  $n_2$  measurements. *Opt. Lett.*, 14(17):955–957, Sep 1989.
- [18] M. Sheik-Bahae, A. A. Said, T.-H. Wei, D. J. Hagan, and E. W. Van Stryland. Sensitive measurement of optical nonlinearities using a single beam. *Quantum Electronics, IEEE Journal of*, 26(4):760–769, Apr 1990.
- [19] D. Weaire, B. S. Wherrett, D. A. B. Miller, and S. D. Smith. Effect of low-power nonlinear refraction on laser-beam propagation in InSb. *Opt. Lett.*, 4(10):331–333, Oct 1979.
- [20] H. Kogelnik and T. Li. Laser beams and resonators. *Appl. Opt.*, 5(10):1550–1567, Oct 1966.
- [21] K. Tamura, C. R. Doerr, L. E. Nelson, H. A. Haus, and E. P. Ippen. Technique for obtaining high-energy ultrashort pulses from an additive-pulse mode-locked erbium-doped fiber ring laser. *Opt. Lett.*, 19(1):46–48, Jan 1994.
- [22] P. Maine, D. Strickland, P. Bado, M. Pessot, and G. Mourou. Generation of ultrahigh peak power pulses by chirped pulse amplification. *Quantum Electronics, IEEE Journal of*, 24(2):398–403, Feb 1988.
- [23] O. Svelto. *Principles of Lasers*. Springer, New York, 5<sup>th</sup> edition, 2010.
- [24] D. A. Kleinman. Theory of optical parametric noise. *Phys. Rev.*, 174(3):1027–1041, Oct 1968.
- [25] R. L. Fork, O. E. Martinez, and J. P. Gordon. Negative dispersion using pairs of prisms. *Opt. Lett.*, 9(5):150–152, May 1984.

- [26] H. R. Schwarz and N. Köchler. *Numerische Mathematik*. Vieweg + Teubner, Wiesbaden, 7<sup>th</sup> edition, 2009.
- [27] M. Abramowitz and I. A. Stegun. *Handbook of Mathematical Functions with Formulas, Graphs, and Mathematical Tables*. Dover Publications, Washington, 1972.
- [28] M. Sheik-Bahae, D.C. Hutchings, D.J. Hagan, and E.W. Van Stryland. Dispersion of bound electron nonlinear refraction in solids. *Quantum Electronics, IEEE Journal of*, 27(6):1296–1309, June 1991.
- [29] M. Born and R. Oppenheimer. Zur quantentheorie der molekeln. *Annalen der Physik*, 389(20):457–484, 1927.
- [30] D Kivelson and P A Madden. Light scattering studies of molecular liquids. *Annual Review of Physical Chemistry*, 31(1):523–558, 1980.
- [31] R. Cubeddu, R. Polloni, C. A. Sacchi, and O. Svelto. Self-phase modulation and "rocking" of molecules in trapped filaments of light with picosecond pulses. *Phys. Rev. A*, 2(5):1955–1963, Nov 1970.
- [32] D. McMorow, W.T. Lotshaw, and G.A. Kenney-Wallace. Femtosecond optical kerr studies on the origin of the nonlinear responses in simple liquids. *Quantum Electronics, IEEE Journal of*, 24(2):443–454, feb 1988.
- [33] Toshiaki Hattori and Takayoshi Kobayashi. Ultrafast optical kerr dynamics studied with incoherent light. *The Journal of Chemical Physics*, 94(5):3332–3346, 1991.
- [34] Kenji Kiyohara, Kenji Kamada, and Koji Ohta. Orientational and collision-induced contribution to third-order nonlinear optical response of liquid cs<sub>2</sub>. *The Journal of Chemical Physics*, 112(14):6338–6348, 2000.
- [35] B. I. Greene, P. A. Fleury, H. L. Carter, and R. C. Farrow. Microscopic dynamics in simple liquids by subpicosecond birefringences. *Phys. Rev. A*, 29(1):271–274, Jan 1984.
- [36] Constantinos Kalpouzos, Dale McMorow, William T. Lotshaw, and Geraldine A.

- Kenney-Wallace. Femtosecond laser-induced optical kerr dynamics in cs<sub>2</sub>/alkane binary solutions. *Chemical Physics Letters*, 150(1-2):138 – 146, 1988.
- [37] R.W. Hellwarth. Third-order optical susceptibilities of liquids and solids. *Progress in Quantum Electronics*, 5:1 – 68, 1979.
- [38] B. I. Greene and R. C. Farrow. Direct measurement of a subpicosecond birefringent response in cs<sub>2</sub>. *The Journal of Chemical Physics*, 77(9):4779–4780, 1982.
- [39] D. Close, C. Giuliano, R. Hellwarth, L. Hess, F. McClung, and W. Wagner. Self-focusing of light of different polarizations. *Quantum Electronics, IEEE Journal of*, 2(9):553 – 557, Sep. 1966.
- [40] Anna Samoc. Dispersion of refractive properties of solvents: Chloroform, toluene, benzene, and carbon disulfide in ultraviolet, visible, and near-infrared. 94(9):6167–6174, 2003.
- [41] D. R. Lide and W. M. Haynes. *CRC Handbook of Chemistry and Physics*. CRC Press, Boca Raton, 90<sup>th</sup> edition, 2009.
- [42] A. A. Said, M. Sheik-Bahae, D. J. Hagan, T. H. Wei, J. Wang, J. Young, and E. W. Van Stryland. Determination of bound-electronic and free-carrier nonlinearities in znse, gaas, cdte, and znte. *J. Opt. Soc. Am. B*, 9(3):405–414, Mar 1992.